ABSTRACT

Title of dissertation: DIRECT NUMERICAL SIMULATION
OF NON-PREMIXED FLAME
EXTINCTION PHENOMENA

Praveen Narayanan, Doctor of Philosophy, 2010

Dissertation directed by: Dr. Arnaud Trouvé
Department of Fire Protection Engineering

Non-premixed flame extinction phenomena are relevant in a variety of combusting environments, including but hardly limited to diesel engines, pool fires, and fire suppression scenarios. These disparate phenomena are controlled by various parameters that contain information on flame stretch, heat losses, composition of the fuel and oxidizer supply streams, etc. Direct Numerical Simulation (DNS) is used in the present study to provide fundamental insight on diffusion flame extinction under non-adiabatic combustion conditions. The list of DNS configurations include: (C1) counterflow laminar flames with soot formation and thermal radiation transport; (C2) coflow turbulent flames with soot formation and thermal radiation transport; (C3) counterflow laminar and turbulent flames interacting with a mist-like water spray. Configurations C1 and C2 use single-step chemistry while configuration C3 uses detailed chemistry (all cases correspond to ethylene-air combustion). Configuration C1 is also treated using large Activation Energy Asymptotics (AEA). The AEA analysis is based on a classical formulation that is extended to include ther-

mal radiation transport with both emission and absorption effects; the analysis also includes soot dynamics. The AEA analysis provides a flame extinction criterion in the form of a critical Damköhler number criterion.

The DNS results are used to test the validity of this flame extinction criterion. In configuration C1, the flame extinction occurs as a result of flame stretch or radiative cooling; a variation of configuration C1 is considered in which the oxidizer stream contains a variable amount of soot mass. In configuration C1, flame weakening occurs as a result of radiative cooling; this effect is magnified by artificially increasing the mean Planck soot absorption coefficient. In configuration C3, flame extinction occurs as a result of flame stretch and evaporative cooling. In all studied cases, the critical Damköhler number criterion successfully predicts transition to extinction; this result supports the unifying concept of a flame Damköhler number Da and the idea that different extinction phenomena may be described by a single critical value of Da.

DIRECT NUMERICAL SIMULATION
OF NON-PREMIXED
FLAME EXTINCTION PHENOMENA

by

Praveen Narayanan

Dissertation submitted to the Faculty of the Graduate School of the
University of Maryland, College Park in partial fulfillment
of the requirements for the degree of
Doctor of Philosophy
2010

Advisory Committee:
Associate Professor Arnaud Trouvé, Advisor/Chair
J. L. Bryan Professor James Quintiere, Dean's Representative
Professor Howard Baum
Associate Professor Andre Marshall
Assistant Professor Peter Sunderland
Professor Greg Jackson
Associate Professor Christopher Cadou

Acknowledgments

I have made a few good friends in Maryland who I wish to thank immensely. Mr. Bhargav Kanagal, Mr. Luis Bravo, Mr. Debojyoti Ghosh, Dr. Vivien Lecoustre, and Mr. Tom Dotson are notable. I wish them the best in their endeavors.

And last but hardly the least, to my family and immediate of kin, for providing long distance comfort and freedom to pursue what I think is best for me.

Table of Contents

List of Tables

List of Figures

List of Abbreviations

AEA   Activation Energy Asymptotics
DNS   Direct Numerical Simulation
RTE   Radiation Transport Equation

Nomenclature

Greek symbols

α	Strain rate
δ	Reduced Damköhler number
ϵ	Small parameter for asymptotic expansion
ζ	Non-dimensional Howarth coordinate
η	Inner mixture fraction coordinate
θ	Non-dimensional inner flame temperature
κ	Planck mean absorption coefficient
λ	Thermal conductivity
ξ	Dimensional Howarth transformed coordinate
ρ	Density
σ	Stephan-Boltzmann constant
τ	Time scale, shear stress tensor
χ	Scalar dissipation rate
$\dot{\omega}$	Reaction rate
Ω	Solid angle

Roman symbols

A	Arrhenius frequency factor in reaction rate
B	Arrhenius frequency factor in reaction rate
D_k	Mass diffusivity of species k
Da	Damköhler number
E	Total gas phase energy per unit volume
e	Gas phase internal energy per unit volume
f_v	Soot volume fraction
G	Radiation absorption term appearing in energy equation
h	Gas phase enthalpy per unit volume
ΔH_F	Heat of combustion per unit mass of fuel
I	Radiation intensity
I_b	Black body intensity
Le	Lewis number
M	Molecular weight
n	Soot number density
N_A	Avogadro number
Nu	Nusselt number
p	Pressure
Pr	Prantl number
$\vec{q_r}$	Radiation heat flux vector
R	Universal gas constant, flame weakness factor
Re	Reynolds number
s	Coordinate along path of a ray
Sc	Schmidt number
T	Temperature
T_a	Activation temperature
Y_k	Mass fraction of species k
u_k	Velocity in direction k
$V_{t,k}$	Thermophoretic velocity in direction k
x, y, z	Spatial coordinates in x, y and z directions
Z	Mixture fraction

Subscripts

st	Stoichiometric location
BS	Burke-Schumann quantity
f	Quantity at flame

Superscripts

$'$	Dimensionless quantity
$\hat{}$	Dimensionless outer quantity
$\tilde{}$	Dimensionless inner quantity

Chapter 1

Introduction

1.1 Background

The present work concerns itself non-premixed or diffusion flames, investigating conditions under which these flames (with initially unmixed streams of fuel and oxidizer) show propensity to extinguish [47]. Non-premixed flame extinction is a phenomenon that may be described canonically as a *hole* in a flame, an event where the flame is quenched, or has ceased to burn even when fuel and oxidant are favorably mixed. From a practical standpoint, non-premixed flame extinction is a highly relevant phenomenon, and is significant in a number of seemingly disparate combusting environments. In diesel engines, where the environment is highly turbulent, characterized by large Reynolds numbers and flame stretching, extinction is linked to conditions favoring pollutant formation such as NO_x, CO and soot [32, 33, 77]. In fires- which are buoyancy driven environments with comparatively lower Reynolds numbers- it is suggested (but is moot) that extinction behavior may play a role in the transitioning from sooting to smoking fires [40]. These environments (such as in pool fires) are strongly affected by radiation heat loss, unlike in engines, where radiation heat loss is not particularly important for extinction. In compartment fires [41, 80], conditions may exist where the fuel and oxidizer are vitiated, leading to quenching from insufficient reactants -or dilution [115, 79, 115]. One need also make

mention of flame extinction from the standpoint of fire-suppresion-in the designing

of sprinklers, for example-where suppression takes place from interactions between

fine water droplets atomized by the sprinkler and the fire, as a result of evaporative

cooling [31, 35]. Description is now made of the the various types of non-premixed
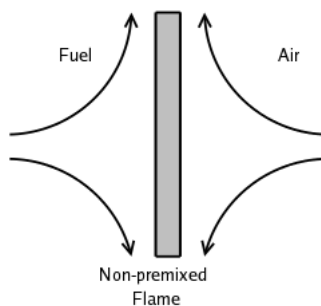
Figure 1.1: Schematic of a non-premixed flame

extinction phenomena in terms of residence time arguments [75, 113] In this con-

nection, it is necessary to introduce two key time-scales, the mixing time-scale τ_m

and the chemical time scale τ_c. The ratio of these two quantities is known as the

Damköhler number $Da = \tau_m/\tau_c$, which is central to determining the *structure* and

extinction of non-premixed flames. In well-burning flames (say, in the usual sense,

the hydrocarbon flame) the chemical processes usually occur much faster than the

rate of mixing. Thus $\tau_m >> \tau_c$ or $Da >> 1$. Extinction conditions are exhibited

when conditions occur such that the Damköhler number is no longer large. Simply

put, one expects this to happen when

$$\tau_m \sim \tau_c \tag{1.1}$$

Typically, mixing conditions are embodied in the levels of laminar or turbulent

stretching (alternatively, one may refer to it as strain), contained in the strain

2

rate α, or the flame scalar dissipation rate χ_{st} (conveniently used in CFD codes), which are both inverse time scales. Chemical time-scales, when expressed by a one-step Arrhenius kinetics model, depend on the flame temperature, predicated by an activation temperature (which is usually large for hydrocarbon flames).

$$\tau_c \sim \left[\exp\left(-\frac{T_a}{T_{st}} \right) \right]^{-1} \tag{1.2}$$

where T_a is the activation temperature corresponding to a single-step Arrhenius kinetics model and T_{st} is stoichiometric flame temperature. Thus, one may define a Damköhler number that scales as

$$Da \sim \frac{\exp(-T_a/T_{st})}{\chi_{st}} \tag{1.3}$$

Inspection of the foregoing equation suggests that Da can become small when conditions occur such that χ_{st} is large, or T_{st} is small, either or both of which may occur for the ratio to become small (Chapter 3). This mathematical model is useful in elucidating the phenomenological ideas. The classical description of flame extinction (in the absense of heat losses) may be understood in terms of the S-curve, presented in Figure 1.2, where the maximum flame temperature is sketched against the Damköhler number. The upper branch constitutes the diffusion flame (or near equilibrium) regime (near complete combustion of reactants occurs in this regime), while the lower branch is the frozen regime (extinguished) [113]. The middle branch is typically unstable. As one traverses the curve from the right, by decreasing the Damköhler number, there occurs a point where transition occurs from burning to non-burning (which in the classical picture is by increasing stretch), so that the system jumps from the upper branch to the lower branch. This corresponds to the

extinction conditions Da_E, T_E in the curve. Likewise, one may also traverse this curve from the left, so that transition occurs from the lower branch to the upper branch, occuring at the ignition Damköhler number Da_I. The ambient lower branch conditions in the figure are taken as as $T_{F,o}$, the fuel temperature, while T_{ad} is the adiabatic flame temperature.

This picture is altered when there is heat loss, in that the maximum upper branch temperature would be lower because of the heat losses. These scenarios are discussed in the subsequent chapters.
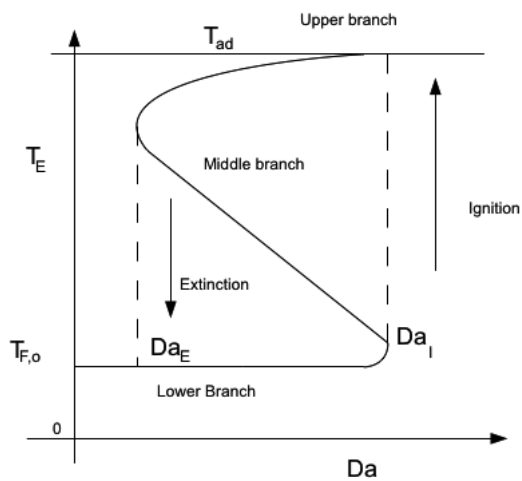
Figure 1.2: S-curve. Schematic illustration of the dependence of the maximum flame temperature on the Damköhler number.

1.2 Types of Flame Extinction Phenomena

The classical connotation for flame-extinction is with large stretch, where the mixing rate χ_{st} takes large values. This high-stretch limit is also known as *kinetic*

extinction, as seen in the seminal investigations [30, 53] . The extinction conditions may be expressed in terms of a strain-rate, or, as is convenient in combustion CFD solvers, the scalar dissipation rate χ_{st} obtained by carrying out a Crocco transformation on the governing equations, explained in Peters [73]. Examples are the blowing out of a candle, and turbulent quenching in a diesel engine.

Extinction conditions may also occur when a reduction in flame temperature results in reduced burning, and is manifest in an increased chemical time-scale. These conditions may occur in non-adiabatic environments where the flame loses heat to radiation heat losses, or evaporative cooling from water-droplets. When extinction occurs from excessive radiative heat losses, it is typically under sluggish burning conditions, also known as *radiative extinction* where mixing rates are low (i.e. low χ_{st}). These conditions are not often seen under normal earth-gravity flames because of buoyancy effects. However, the existence of the radiatively quenched flames has been confirmed from micro-gravity experiments [63, 100, 86]. Nevertheless, radiation heat loss is dominant in fires, which are characterized by large soot production. The soot is luminous at high temperatures, and black at low temperatures. While earth-gravity flames may not experience low enough stretching conditions to exhibit quenching from radiative heat losses, it is possible that the resulting low flame temperatures lead to a reduction in soot oxidation rates, the upshot of which is that the unoxidized soot escapes as smoke [40, 61]. Also, it is curious and interesting to know that large amounts of heat are trapped in the clouds of smoke surrounding pool-fires [40].

Evaporative cooling affects flame chemistry by lowering its temperature-similar

to radiative heat losses, with the exception that they may be effected even at high stretch rates by controlling the water-loading rates. Likewise, dilution affects flame chemistry by lowering the adiabatic flame temperature, thereby causing flames to extinguish at lower mixing rates.

The present work aims to understand these myriad extinction phenomena by producing mathematical models that incorporate the effects of pertinent controlling parameters, appropriately juxtaposed with numerical experiments from high fidelity Direct Numeircal Simulation runs (DNS), which are used for validation purposes and exploration where necessary.

In this connection, much of the effort here is devoted to demonstrate the validity of the Damköhler number model (the extinction criterion [53, 22, 57, 111]) in non-premixed flame extinction, particularly, in non-adiabatic environments (the classical or non-adiabatic extinction criterion is well known). This is done through a combination of means-theoretical studies to formulate simplified mathematical models using analytical tools (the Activation Energy Asymptotics technique), and numerical experiments to generate datasets (using Direct Numerical Simulations) against which to validate the theoretical models developed.

1.3 Some Flame extinction Studies: Literature Review

In this section is presented the types of flame extinction studies carried out by researchers, so as to give survery some of the pertinent literature discussing the analytical, experimental and computational approaches and configurations.

Analytical studies on flame extinction have frequently used simplified configurations using Asymptotic Analysis [12](with assumptions such as one-dimensionality, steady state, constant density, single-step chemistry). The flame structure is decomposed into the outer non-reacting regions and the inner reacting regions, which are then merged using matching techniques [12]. One often refers to the outer solutions as the Burke-Schumann solutions [16], obtained by invoking the flame-sheet model, in which reactants are completely consumed at the flame location. The small parameter for these asymoptotic expansions may be obtained using the largeness of the Damköhler number, or the largeness of the Activation Energy [113]. However, large activation energy asymptotics have the advantage of furnishing *sharp* ignition-extinction criteria, and are therefore attractive.

The early (now classical) studies focused on the kinetic or high-stretch limit. Fendell, in his seminal paper [30], used Damköhler number asymptotics to propose the S-curve for a liquid fuel pyrolysis problem. Numerical simulations were used near extinction because the Damköhler number is not large in this regime. This approach was also used in [19, 17], which did not investigate extinction as such, but obtained the flame structure of various one-dimensional configurations under steady and unsteady conditions. The treatment of large and small Damköhler number regimes were discussed in [19], and [17] respectively. Activation Energy Asymptotics was first used in providing sharp ignition-extinction criteria by Liñan [53, 54] for strained laminar counterflow flames to obtain the high-stretch limit. Theoretical work by Liñan, Williams, Peters, Law and their coworkers extends upon this work to more complex scenarios with radiation [89], [57], [111] and differential diffusion

[111, 26].

The flamelet idea was proposed in Peters [73] to express the governing equations in mixture fracrtion space by carrying out a Crocco transformation and using the thinness of the reaction zone. Extinction may be described using Liñan's approach for the steady laminar flamelet. Description of laminar flamelet structure is presented in Williams [114], Bilger [13]. Flamelet modeling has been extensively investigated since then, and forms an essential part of turbulent combustion modeling. A review is presented Peters' monograph [75].

Formulations for radiation had mostly extended upon Liñan's approach by treating radiation as a singular quantity around the flame, and arriving at an effective activation temperature (when expressed suitably) characterizing radiation heat loss [89]. The investigation [89] formed the basis of the radiation formulation in subsequent efforts [22, 111, 21, 57]. These studies demonstrate the dual extinction limits -the high stretch kinetic limit where radiation is negligible, and the low stretch radiative limit, where radiation is considerable (as a percentage of the flame heat release rate). The formulation invokes the optically thin formulation [90], using which one solves the ODEs using a multiscale asymptotic expansion procedure, where the boundary layers comprise a radiation zone, enveloping a much thinner reaction zone. It is mentioned in this context that such an assumption may be valid in a limited number of configurations where flame radiation is concentrated in a small region around the flame, and is dubious in heavily sooting configurations which can contribute to radiation being distributed non-locally (i.e. to the flame), by which it is meant that one can have a radiation field arising from processes exclusive of

the flame element under consideration, as would be the case in large smoking fires. The asymptotic analysis used in the current work attempts to remedy this partly by accounting for this non-locality, in that both radiation emission and absorption are included in the formulation by solving for the radiation transport equation [66, 94]. It might be useful to derive approximations in optically thick media as is done in investigations by Szoke et. al. [94] for astrophysical systems.

The aforementioned mathematical studies on radiating flames were used to demonstrate the radiative extinction limit in counterflow and spherical diffusion flames (in addition to the kinetic or high stretch limit). AEA counterflow flame studies include [57, 111]. Spherical flame investigations were carried out in [22] for an evaporating droplet subject to radiation heat loss. Spherical flames subject to radiative heat loss from soot was investigated in [64] (which, however, uses an approach based on the soot absorption coefficients to compute radiation, and is different from the formulation in [89]). Regardless of the formulation for radiation used, these studies capture the qualitative features of low strained flames subject to radiation heat loss and provide a criterion to describe kinetic and radiative extinction.

Some of the early experimental studies by Tsuji et. al. attempted to understand the structure and extinction of strained laminar counterflow flames [103, 104] (numerically, among the first known works was Spalding and Jain in [91] for a one-dimensional planar diffusion flame with kinetics)in the stagnation region of a porous burner. Particularly notable is the counterflow flame study by Puri and Seshadri [79] where the effect of dilution and its connection with flame structure and extinction was discussed, together with an AEA model accounting for reactant temperature

9

and concentration. Dilution reduces the adiabatic flame temperature, under which conditions the flame burns more sluggishly and can therefore extinguish more easily. This is demonstrated through an analysis of the governing equations subsequently in chapter 3.

The effects of adding diluents (halon suppressants such as CH_3Br, CF_3Br) were illustrated in papers [15, 59, 36, 37, 87]. Suppressants reduce flame intensity through a combination of chemical, thermal and dilution effects, which is discussed in these papers. Experimentally, flame extinction from dilution may also be investigated by using the cup-burner, which is a coflow burner with a wide nozzle, and with low velocity injection of reactants to mimic a fire configuration [56, 8]. However, cup burner flame extinction is qualitatively different from counterflow flame extinction in that the flames are blown off from the burner upon increasing diluent concentration (with experimental and numerical demonstrations in [42, 95, 56]) and drift downstream.

Radiative extinction was demonstrated by T'ien numerically in [99], [100], [101] in which radiative extinction was shown to occur in the context of a pyrolyzing solid with an opposed flow configuration (also in [82]). Experiments on radiative extinction have been carried out in microgravity, primarily because the effects of radiation heat loss become become more pronounced at lower strain rates. Maruta [63] demonstrated low strain-rate radiative extinction experimentally in counterflow flames in methane diluted with nitrogen. The interplay between radiative extinction and dilution was investigated in [36]) so as to get a measure of the minimum suppressant concentration necessary for extinction. A notable aspect is that there

exists a critical mass concentration limit (typically, presented as the oxidizer limit) in the presence of radiation below which there can no combustion [99, 100], which will not be the case when there is no radiation.

Another oft-used configuration of interest is the spherical burner (Figure 1.3). microgravity, discussed in [5, 76, 6, 64, 102, 96, 97, 98, 84, 85]. These flames are typically transient in nature and frequently experience radiative extinction. The canonical features at the radiative extinction limit such as low flame temperature (~ 1150 K) and large radiant heat loss fraction (as a percentage of the flame heat release rate, of about 70%) are manifest . The flames are often blue at the radiative limit owing to the inhibition of soot production [84, 85]. In [84, 85], pertinent aspects emerge in connection with flame extinction occurring from burner related heat losses (base extinction) and extinction far from the burner (hole extinction), in addition to numerical simulations demonstrating radiative extinction when the flame radius become large. These issues appear (while peripheral to the main discussion) in [49, 48], where the focus was more on determining the $C/0$ ratio and temperature effects in sooting spherical flames. In [97, 98] spherical microgravity diffusion flames were studied computationally (along with experimental validation from [25]) to investigate the effects of dilution on flame structure and extinction. Fuel and oxidizer dilution were examined and it was concluded that oxidizer side dilution has a more severe effect in affecting the flame properties (e.g. temperature). Furthermore, corroboration appears with the findings in [84, 85] in that the flame temperature at the radiative extinction limit is about 1150 K.

Numerical demonstration of radiative extinction in counterflow diffusion flames

11
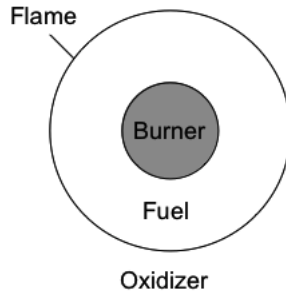
Figure 1.3: Spherical flame

(Figure 1.4) were carried out in [7, 28, 4, 115], where in addition to describing the behavior of low strained, radiatively weakened flames, some light is also shed on the flamelet structure close to extinction. Radiative extinction in the presence of soot in microgravity one-dimensional counterflow diffusion flames were investigated in an analytical-numerical study in [4]. Diluted methane flames were examined (along
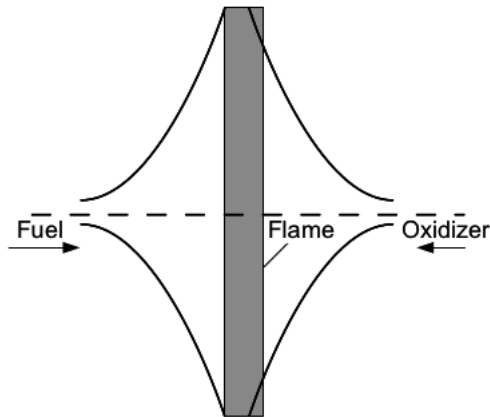
Figure 1.4: Counterflow flame

with experiments) using OPPDIFF in [115], the aim of this work being to examine flame extinction behavior under vitiated fuel/oxidizer conditions (in which radiation

plays a role at low stretch-rate). Also related to this were studies by Utiskul [105] that examined flame extinction in under-ventilated compartment fires, classified according to the level of ventilation (well ventilated or under-ventilated, steady or unsteady burning). Quintiere [81], used a critical flame temperature criterion for extinction in fires to describe extinction in underventilated fires, using similar phenomelogy based on the Damköhler number.

Lewis number effects were examined in [26, 23, 24]. Reactant leakage at near extinction conditions can lead a premixed flame type regime sensitive to cellular oscillations. The flames can be strenghthened or weakened by the increase or decrease of Lewis numbers. This effect has been attributed to the interplay between thermal and mass transfer [114, 47], so that if one increases the Lewis number of either reactant, heat loss effects increase, and leads to a drop in the flame temperature, and the flames are therefore weaker. One may argue about the strengthening of flames by decreasing the Lewis number in a similar vein.

Flame extinction from evaporative cooling was investigated in [51, 50]. Experimental and numerical studies were carried out in [51] to assess the importance of chemical, thermal, dilution effects of fine water droplets in extinguishing counterflow diffusion flames, using a Lagrangian-Eulerian droplet formulation. This was also used in [50] in describing the flow field of fine water droplets. DNS studies [109] describe evaporation in a fuel-spray environnment (which the current study extends upon to water-spray).

The current work is an extension of the DNS studies carried out by Dr. Yi Wang [107], which focused on kinetic extinction exacerbated by wall cooling [110,

107], with inclusion now being made of the effects of soot, radiation and evaporative cooling. The analysis in this work is based primarily on the Damköhler number based on single step chemistry in similar fashion to Liñan [53], and while this is inaccurate in real flames -the reader is referred to Williams' extensive review [114]- since it omits key elements allied with the chemistry, such as fuel and oxidizer consumption, and branching, the thesis is to test how well the single-step asymptotic model describes extinction.

1.4   Objectives and Author's Contributions

1.4.1   Objectives

The research conducted as part of this thesis focuses on multifarious aspects of non-premixed, non-adiabatic flame extinction pertaining to stretch, radiation heat loss, and evaporative cooling. The attempt is to bring together these various extinction phenomena in terms of a Damköhler number criterion derived (using AEA theory) for non-adiabatic configurations. To this end, DNS simulations are carried out in three configurations to highlight different aspects of flame extinction (owing to stretch, radiation heat loss and evaporative cooling), where the validity of the Damköhler number based criterion is examined.

The first configuration considered is (C1) counterflow laminar flames with soot formation and thermal radiation transport. Ethylene-air combustion with single-step chemistry is assumed, with constant transport properties. These flames are investigated in order to bring to focus the effects of radiation and flame stretch

Table 1.1: Test configurations

C1	Laminar counterflow flames with soot formation and radiation transport
C2	Turbulent coflow flames soot formation and radiation transport
C3	Laminar and turbulent counterflow flames weakened by evaporating droplet spray

on flame extinction. They are analyzed by means of DNS simulations, together with an AEA approach that is developed for radiating flames considering a formulation that includes both emission and absorption (by solving the RTE). The aim is to understand, firstly, the parameters that control the structure and extinction of these radiating flames -the effects of stretch, radiative heat loss, temperature and soot; secondly, to demonstrate the effect of external soot loading on the flame structure and extinction; and thirdly, to develop an extinction criterion for kinetic and radiative extinction that may be used in other configurations.

The second configuration considered is (C2) counterflow turbulent flames with soot formation and radiation transport, with an artificially increased radiation absorption coefficient to amplify radiation effects. The chemistry and transport properties are identical to C1. These flames are subject to soot loading caused by turbulent mixing. In this sense, it is similar to the configuration C1 because the soot does not originate locally, but is delivered to individual flame elements from elsewhere. It is of interest to know the effect that soot has in weakening these flames. The extinction criterion developed for C1 is tested in C2.

The third configuration considered (C3) is one with laminar and turbulent counterflow flames weakened by an interacting mist of water-spray. The focus is

to understand flame extinction from thermal cooling driven by droplet evaporation. Unlike configurations C1 and C2, this configuration uses detailed chemistry to simulate more realistic flames. These ethylene-air counterflow flames loaded with fine water droplets in the mist regime (10μm). The study uses a highly resolved (15μm) grid, detailed chemistry (the DRG mechanism) and turbulence injection. Laminar DNS simulations are first carried out at various droplet mass loading rates in order to better understand the effect of droplet loading on flame extinction. In addition to this, turbulent counterflow flame DNS are carried out to understand flame quenching in an environment where the flames are weakened by both stretch and spray-interactions. These are then analyzed using the extinction criterion diagnostics developed for flame C1. In addition, flame C3 opens itself to further investigation as regards the validity of classical state relationships in this case where there is addition of vapor mass from the droplet phase.

The aim of this study is thus, to firstly bring basic information on the flames that are studied -C1, C2, C3- such as the flame structure, heat release rate and temperature, and secondly, to understand flame extinction in these different scenarios by testing them with the extinction criterion developed.

1.4.2 Author's Contributions

The current work is an extension of previous efforts by Dr. Yi Wang, which examined non-adiabatic, turbulent non-premixed flame extinction at high stretch conditions with interactions with cold wall surfaces. The current work builds upon

this by examining non-adiabatic configurations where heat losses occur from radiation, and by evaporative cooling. Much of this is owing to contributions by Dr. Yi Wang, who had developed the soot and radiation (based on DTM) solvers, which are used in configurations C1 and C2.

The code used for the lagrangian spray solver was originally developed by Dr. Chris Rutland's group at the University of Wisconsin [2], for fuel sprays. The candidate has adapted this code for extinction studies with water-spray (configuration C3), with extensive collaboration with Paul Arias and Dr. Hong Im at the University of Michigan. Paul Arias and Dr. Hong Im have contributed to developing improved boundary conditions [3] for configuration C3, which is used in the current studies. Detailed chemistry is used in configuration C3, developed by Dr. Tianfeng Lu and Dr. C. K. Law in Princeton University.

At a broader level, the effort supplements large scale DNS efforts of Dr. J. H. Chen's group at Sandia National Laboratories.

The candidate has primarily been involved (in terms of code development) in the implementation into configurations C1, C2 and C3, the codes owing to the aforementioned parties. This is to be noted while perusal is made of the physical and numerical models in the S3D solver subsequently.

The candidate's role has been to devise numerical experiments, and develop the theory in these non-adiabatic configurations, specifically aimed at bringing to light aspects of flame extinction. Emphasis is made of the theoretical developments using AEA theory in deriving a Damköhler number based extinction criterion used these configurations. The mathematical treatment contains improvements in that

non-optically thin configurations are considered by solving for the Radiation Transport Equation (RTE). This is an improvement over existing theoretical work which considers optically thin media (with ramifications in sooting environments). A reappraisal of mixture fraction and state-relationships in the multi-phase environment with droplet spray (configuration C3), was deemed necessary (where the classical two phase definition of the mixture fraction was found inaccurate). The candidate was involved in developing modified mixture fraction and state-relationhips by recognizing this aspect, and in demonstrating them with DNS.

In summary, the candidate's contributions are enumerated below.

1. Devising and running numerical experiments to demonstrate diffusion flame extinction in non-adiabatic configurations C1 and C2 (sooting and radiating flames in laminar counterflow and turbulent coflow flames).

2. Devising and running numerical experiments to demonstrate diffusion flame extinction in non-adiabatic configuration C3 (flames weakened by evaporative cooling from water droplets interacting with laminar and turbulent counterflow diffusion flames)

3. Developing (through rigorous mathematical analysis) a modified extinction criterion based on the classical Damköhler number based criterion for non-adiabatic configurations using AEA theory. Improvements in the mathematical treatment are noted, addressing optically thicker media by accounting for radiation emission and absorption by solving the Radiation Transport Equation (RTE).

4. Demonstrating the validity of the modified extinction criterion in describing diffusion flame extinction in configurations C1, C2 and C3 (environments where extinction from stretch, radiative heat loss and evaporative cooling may be described by a single extinction criterion).

5. Developing modified state-relationships in configuration C3 where the classical two-stream mixture fraction was demonstrated to be inadequate.

1.5   Organization

The content is organized as follows.

In Chapter 2 the governing equations for reacting flow as solved in the DNS solver S3D are presented, with a description of the modeling capabilities of the solver (chemical kinetics, soot transport, radiation transport).

In Chapter 3, the theory of Activation Energy Asymptotics (AEA) is introduced for the configuration C1. The aim of this chapter is to lay the groundwork for subsequent analysis of flames with soot loading, and to derive an extinction criterion based on the Damköhler number. By means of a Howarth transformation [9], the two dimensional counterflow flame equations are transformed into a one-dimensional form. Soot is loaded on the oxidizer side of these flames, and the equations are solved using matched asymptotic expansions with the Activation Energy Asymptotics (AEA) technique. The analysis furnishes extinction criteria containing the effects of various controlling parameters-strain, radiation heat loss and soot. Additionally, the mathematical treatment contains the 'novelty' of a more rigorous

treatment of radiation emission and absorption by solving for the radiative transport equation. It is pointed out that the often used optically thin approximation using which one treats the radiation zone as a singular quantity in other works on radiating flames [22, 111, 57, 89], while describing the phenomenology, may be inaccurate in heavily sooting flames. The results of the asymptotic analysis are validated with DNS data to justify the modeling assumptions made.

In Chapter 5 laminar counterflow flames C1 are subjected to external soot loading to study its effect on the flammability limits-the high stretch kinetic extinction limit and the low stretch radiative extinction limit. The equations are solved using the AEA approach developed in Chapter 3.

Chapter 6 centers the discussion primarily on turbulent flames C2, so as to bring to the fore the effect of non-local soot loading in turbulent environments (in effect, an extension of Chapter 3) in relation to the flame structure, radiating properties, and questions on flame weakening and extinction arising thereof. In the turbulent flames studied, it is found that the flames are considerably weakened by soot loading, but are not radiatively quenched. However, the weakening events are closely allied with soot emission-or leakage-from these flames, raising some interesting questions regarding the cessation of soot oxidation chemistry and radiative "extinction-like" phenomena. Consistent with Chapter 3, it is also demonstrated that the extinction limits are considerably altered in the absence of external soot loading, by means of laminar counterflow DNS datasets.

Chapter 7 conducts investigations in the configuration C3, with flame-droplet interactions to understand flame extinction from evaporative cooling. Diagnostic

improvements on state-relationships (Appendix A) find usage in this study. The high quality numerical data resulting from these numerical simulations provide detailed information on flame-structure and properties. Laminar and counterflow diffusion flames are subjected to various levels of droplet loading so as to investigate the response of these flames to water-loading, from light loading which results only in flame weakening to supercritical loading that causes extinction. Noteworthy diagnostics include the application of the Damköhler number-developed in more simplified cases (Chapter 3)-the flame temperature, and heat release rates integrated across the flame sheet.

In addition, is attached in the Appendix A, a somewhat peripheral study (corresponding to configuration C3) that came about while investigating flame extinction in an evaporating spray environment. In this, one sets up a framework for analyzing data in an evaporating spray environment, inasmuch as to demonstrate that the pertinent state relationships (embodied in the mixture fraction) require modification. It is shown that in this environment the traditional spray-free definition of the mixture fraction (the correct definition of which is of utmost importance for flamelet modeling) is incorrect, and that one must modify these relationships so as to include an additional variable to describe the added mass from the evaporating water-stream. Thus, instead of a single gas-phase mixture fraction Z the modified state relationships are to now include, in addition to Z, a spray vapor fraction γ. The state relationships derived are subject to validation using DNS data from two dimensional simulations with detailed chemistry, with a lagrangian water-spray model to decribe dilute liquid sprays. It is envisaged that similar modifications are

necessitated in spray environments for an accurate description of the physics. While this study is not per se, one on extinction, it is nevertheless a useful (and necessary) by product of the study on flame-droplet interactions.

Chapter 2

Direct Numerical Simulation

Direct Numerical Simulation is a numerical approach to simulate a variety of fluid dynamic phenomena, with great fidelity. DNS is attractive because it does not require a model for the Reynolds stress turbulence terms. It is also an expensive approach because all the scales of motion should be resolved, from the smallest eddies to the largest eddies. The reader is referred to Moin and Mahesh [67] for an overview of current progress in DNS.

DNS of combustion must account for a host of complex phenomena, such as gas-phase chemical kinetics, heat release, soot (particulates), radiation losses, and multiphase phenomena (pyrolysis, droplet vaporization). Depending on the application that one is interested in, it may become necessary to model these phenomena accordingly.

It is to be mentioned that in addition to resolving the flow-scales, one must now also resolve the reaction-layer (loosely, the thin region where fuel and air mix stoichiometrically and where most of the reaction takes place). The thickness of the reaction zone is usually smaller than the Kolmogorov length scales, leading to locally laminar flame-sheets. This is the laminar flamelet assumption, with seminal contributions by Peters [73, 74] and Williams [113] and Liñan [53].

In a DNS (in this work, DNS is undertood to be in a combusting framework),

both the flow-scales and the chemical scales need to be resolved. The reader is referred to [106] for progress in DNS of nonpremixed flames.

2.1 DNS Solver

The Direct Numerical Simulations are carried out with an advanced numerical solver (S3D) that has been part of a collaborative development effort from a team consisting of Sandia National Laboratories, the universities of Michigan, Wisconsin and Maryland. The solver has a number of sophisticated numerical and physical models built into it, such as detailed transport, detailed chemistry (CHEMKIN compatible), a soot model, and a lagrangian particle solver to handle spray injection.

This work features high-fidelity simulations that leverage state of the art computing resources from the Department of Energy's NERSC computing center (part of Lawrence Berkeley National Laboratories, California). While the specific focus of this effort is to examine non-premixed flame extinction phenomena, a larger goal of the project is in using scientific computing to bring insight into combustion science with scientific-visualization and data-mining techniques.

2.2 Computational Methodology in DNS

We use an advanced numerical solver called S3D that has been developed for combustion applications. S3D is a fully compressible Navier-Stokes solver coupled with an integrator for combustion chemistry and is based on eighth-order finite differencing [45], fourth-order explicit Runge-Kutta time integration [46], characteristic-

based boundary conditions treatment [78, 10], a CHEMKIN-compatible description of chemical kinetics [44], and a conventional rectangular Cartesian mesh capability. In addition, S3D is a massively parallel solver based on message passage interface (MPI) libraries and is currently being redesigned and enhanced for increased performance and capability by a consortium of research institutions [2].

2.2.1 Governing Equations

We numerically solve for the multi-component gas-phase flow equations (for mass, momentum, energy and species mass) which are the following, for a single-phase, gaseous fluid (the multiphase case with spray is examined in Section 2.2.5:

$$\frac{\partial \rho}{\partial t} + \frac{\partial}{\partial x_j}(\rho u_j) = 0 \tag{2.1}$$

$$\frac{\partial}{\partial t}(\rho Y_k) + \frac{\partial}{\partial x_j}(\rho Y_k u_j) = -\frac{\partial}{\partial x_j}(\rho Y_k V_{k,j}) + \dot{\omega}_k; \qquad 1 \le k \le N_s \tag{2.2}$$

$$\frac{\partial}{\partial t}(\rho u_i) + \frac{\partial}{\partial x_j}(\rho u_i u_j) = -\frac{\partial p}{\partial x_i} + \frac{\partial \tau_{ij}}{\partial x_j} + \rho g_i \tag{2.3}$$

$$\frac{\partial}{\partial t}(\rho E) + \frac{\partial}{\partial x_j}(\rho E u_j) = -\frac{\partial}{\partial x_j}(p u_j) + \frac{\partial}{\partial x_j}(\tau_{ij} u_i) - \frac{\partial q_j}{\partial x_j} + \rho g_j u_j \tag{2.4}$$

where t is time, x_j the spatial coordinate in the j-direction, the mass density, u_j the j-component of flow velocity; Y_k the mass fraction of species k, $V_{k,j}$ the $j$component of molecular diffusion velocity for species k, $\dot{\omega}_k$ the mass reaction rate for species k,

p the pressure, τ_{ij} the ij-component of the viscous stress tensor, g_i the i-component of acceleration due to gravity, E the total energy per unit mass (internal energy plus kinetic energy) and q_j the heat flux vector. Equation (2.2) is written for $1 \leq k \leq N_s$, where N_s is the total number of species in the gaseous mixture; Equation (2.3) is written for all 3 components of momentum, $1 \leq i \leq 3$.

Assuming Newtonian fluid behavior, the stress tensor τ_{ij} is linearly related to the velocity gradient tensor as

$$\tau_{ij} = \mu \left(\frac{\partial u_i}{\partial x_j} + \frac{\partial u_j}{\partial x_i} - \frac{2}{3} \delta_{ij} \frac{\partial u_k}{\partial x_k} \right) \tag{2.5}$$

Furthermore, in the energy equation (2.4) E and q_j are defined as

$$E = e + \frac{u_i u_j}{2} = \sum_{k=1}^{N_s} \left(h_k Y_k - \frac{P}{\rho} \right) + \frac{u_i u_j}{2} \tag{2.6}$$

$$h_k = h_k^0 + \int_{T_0}^{T} c_{p,k} dT \tag{2.7}$$

$$q_j = -\lambda \frac{\partial T}{\partial x_j} + \rho \sum_{k=1}^{N_s} h_k Y_k V_{k,j} + q_{r,j} \tag{2.8}$$

where h_k is the total enthalpy per unit mass (chemical enthalpy plus thermal enthalpy), h_k^0 the chemical enthalpy of formation (evaluated at reference temperature T_0), and $c_{p,k}$ the specific heat at constant pressure; all 3 quantities referring to species k; and where λ is the mixture thermal conductivity, T the temperature; $q_{r,j}''$, the radiative heat flux in the j direction. Note that these terms are included in

the energy equation as divergence quantities.

$$\nabla \cdot \vec{q} = \frac{\partial q_j}{\partial x_j} \tag{2.9}$$

Finally, equations (2.1)- also require the equation of state. We assume the ideal gas law

$$p = \rho R T \sum_{k=1}^{N_s} \frac{Y_k}{M_k} = \rho \left(\frac{R}{M} \right) T \tag{2.10}$$

where R is the ideal gas constant, with M_k, the species molecular weights and M being the molecular weight of the mixture.

2.2.2   Chemical Mechanism

The studies conducted in this work feature a combination of simplified one-step ethylene-air chemistry [112], with which simplified analytical models are derived, and a more complex, reduced chemical mechanism for use in detailed calculations with water-spray, using an approach called Directed Relations Graphs (DRG) [60] for Ethylene-air combustion. With the DRG mechanism, the detailed chemical mechanism consisting of 463 species and 70 elementary reactions was reduced to 19 species, 15 semi-global reactions to render it more tractable for use in DNS. A number of techniques were used in [60] to effect this reduction -computational Singlular Perturbation (CSP), Quasi Steady State assumptions (QSS) and Sensitivity Analysis. It is noted that the detailed chemistry aspects of the code were developed by Dr. Tianfeng Lu and coworkers [60].

2.2.3 Soot Transport

Soot formation is modeled as an empirical, two-equation transport process. The model was proposed by Moss and coworkers [68, 93, 69]. Phenomenological process governing soot transport - soot nucleation, growth and oxidation-are included in the equations, which comprise an equation for soot number density n and soot mass fraction Y_s. The soot particles are assumed to be monodisperse and spherical. The soot modeling aspects of the code were developed by Dr. Yi Wang [107].

$$\frac{\partial}{\partial t}\left(\frac{n}{N_0}\right) + \frac{\partial}{\partial x_i}\left(\frac{n}{N_0}u_i\right) = \frac{\partial}{\partial x_i}\left[\frac{\nu}{Sc_{soot}}\frac{\partial}{\partial x_i}\left(\frac{n}{N_0}\right)\right] - \frac{\partial}{\partial x_i}\left(\frac{n}{N_0}V_{t,i}\right) + \dot{\omega}_{(n/N_0)}$$

(2.11)

$$\frac{\partial}{\partial t}(\rho Y_s) + \frac{\partial}{\partial x_i}(\rho Y_s u_i) = -\frac{\partial}{\partial x_i}\left(\rho\frac{\nu}{Sc_{soot}}\frac{\partial Y_s}{\partial x_i}\right) - \frac{\partial}{\partial x_i}(\rho Y_s V_{t,i}) + \dot{\omega}_{\rho Y_s}$$

(2.12)

where $N_0 = 6.023 \times 10^{26}$ molecules/kmol, the Avogadro number. The first term on the right hand side incorporates thermophoresis effects via a thermophoresis velocity $V_{t,i}$.

$$V_{t,i} = -0.54\nu\frac{\partial}{\partial x_i}lnT$$

(2.13)

We introduce artificial diffusion terms (first terms on the right hand side of the soot transport equations) to dampen the solution numerically to improve stability. The Schmidt number Sc_{soot} is prescribed as 1000, a large number. This does not have any effect in the quality of the solution other than to improve stability [107]. Soot volume fractions f_v and mass fractions Y_s are equivalently used. They are related

28

as follows

$$\rho_s f_v = \rho Y_s \tag{2.14}$$

where ρ_s is the density of soot particles, $\rho_s = 1800$ kg/m^3. The soot volume fraction is related to the soot number density by the interaction term $\dot{\omega}_{\rho Y_s}$.

The source terms for soot number and mass densities are modeled as

$$\dot{\omega}_{n/N_0} = \alpha(\xi) - \beta(\xi) \left(\frac{n}{N_0} \right)^2 \tag{2.15}$$

$$\dot{\omega}_{\rho Y_s} = \gamma(\xi)n + \delta(\xi) - S\dot{\omega}_{ox} \tag{2.16}$$

In equation (2.16) first term on the right hand side is from an increase in soot number density due to nucleation, the second term is from soot growth and the last term containing $\dot{\omega}_{ox}$ is from soot oxidation. S is the surface area of soot-particles

$$S = \pi d^2 n = (36\pi n)^{\frac{1}{3}} f_v^{\frac{2}{3}} \tag{2.17}$$

and

$$\alpha(\xi) = c_\alpha \rho^2 T \frac{1}{2} X_c \exp(-\frac{T_\alpha}{T})$$

$$\beta(\xi) = c_\beta T^{\frac{1}{2}}$$

$$\gamma(\xi) = c_\gamma \rho T^{1/2} X_c \exp(-\frac{T_\gamma}{T}) \tag{2.18}$$

$$\delta(\xi) = c_\delta \alpha(\xi)$$

The source term for soot oxidation is given in [93] as

$$\dot{\omega}_{ox} = 1.085 \times 10^5 X_{O_2} T^{-1/2} \exp(-\frac{19778}{T}) \tag{2.19}$$

c_α (m³kg⁻²K⁻¹/²s⁻¹)	c_β (m³K−1/2s⁻¹)	c_γ (m³K⁻¹/²s⁻¹)	c_δ	T_α (K)	T_γ (K)
6.0×10^6	2.25×10^{15}	6.3×10^{-14}	144	4.61×10^4	1.26×10^4

Table 2.1: Constants for use in soot transport equations [107]

2.2.4   Radiation Transport

Radiation is computed in S3D using the Discrete Transport Equation developed by the UMD group [107])or Discrete Ordinates Method (code developed by the UMICH group [116]). The radiative extinction simulations in the current work use the Discrete Transport Method (DTM) developed originally by Lockwood and Shah [58]. DTM is a ray tracing approach, with the domain divided into a number of control-volumes and the angular space is discretized.

Radiation is a complicated process involving both emission of radiant energy from a radiating element, and the absorption of radiant energy from the surroundings.

The radiation transport equation along any direction in $\hat{s}$, for an emitting-absorbing, but non-scattering medium is written as

$$\frac{dI}{ds} = \hat{s} \cdot \nabla I = \kappa I_b - \kappa I \qquad (2.20)$$

where $I_b = \sigma T^4/\pi$ is the black body intensity at temperature T, $\sigma = 5.66 \times 10^{-8}$ W/m²/K⁴ is the Stephan-Boltzmann constant, and I is the intensity of a ray oriented in the direction $\hat{s}$, and κ is the Planck mean absorption coefficient.

In the foregoing equation the term $I_b = \sigma T^4/\pi$ (emission) can be computed locally using temperature, but the other term κI can only be computed by solving

the RTE, which is expensive.

The radiation term in the energy equation $\nabla \cdot \vec{q}_R$ is obtained from the distributon of radiation intensities, for which we need to solve the radiation transport equation.

$$\vec{q_r} = \int_{4\pi} I(\hat{s})\hat{s}d\Omega \tag{2.21}$$

$$\nabla \cdot \vec{q_r} = \nabla \cdot (\int_{4\pi} I(\hat{s})\hat{s}d\Omega) = \int_{4\pi} \hat{s} \cdot \nabla I(\hat{s})d\Omega = \int_{4\pi} \frac{dI}{ds}d\Omega \tag{2.22}$$

Using the radiation transport equation (2.20), we may recast equation (2.22) as

$$\nabla \cdot \vec{q_r} = \kappa(4\pi I_b - \int_{4\pi} I d\Omega) = \kappa(4\pi I_b - G) \tag{2.23}$$

We therefore have contributions from emission (a sink term) $4\pi I_b = 4\kappa\sigma T^4$ and absorption (a source term) κG. The absorption term can only be obtained from solving the radiation transport equation.

In the present computations, the DTM approach is used to solve the radiative transport equation to resolve radiation emission and absorption. DTM is a ray-tracing approach in which: the RTE is first integrated analytically along straight rays that are representative of radiation transport in elementary angular regions; the radiation field is then calculated as a solution of an elliptic system through a succession of iterative sweeps; and a simple projection algorithm is finally applied to transform the radiation field from a ray-based solution to a Eulerian grid-based

solution compatible with the flow and combustion solver [58, 107]. The computations are expensive as they need information from the whole domain, and need resolution to a high degree of angular accuracy. In DTM, precision is controlled by changing the angular discretization, i.e the number of rays N_θ and N_ϕ used to divide the polar and azimuthal coordinates system; we use $N_\theta = 8$ and $N_\phi = 17$. A sub-cycling scheme is also adopted in which the DTM solver is called once every 50 compressible flow time steps. With this scheme, the overhead associated with the calculation of thermal radiation transport is approximately 100%.

2.2.5 Lagrangian Spray Equations

Evaporative cooling phenomena by fine water-droplets are currently being investigated using S3D. This is part of the INCITE project aimed at simulating flame-extinction by fine water-droplets [39]. Water-droplets are computed in a Lagrangian framework. Water-droplets are affected by the local flow conditions: droplet mass, momentum and energy have interaction terms with the gas-phase flow. Flame-droplet interactions take place via an interaction term in the energy equation that accounts for droplet vaporization. The reader is referred to Wang and Rutland [109] for details of the solver. Dr. Chris Rutland's group from the University of Wisconsin was responsible for the original development of the lagrangian spray code.

2.2.5.1 Droplet Phase Equations

The lagrangian droplet equations for mass, momentum and energy are presented below:

$$\frac{\mathrm{d}x_{d,i}}{\mathrm{d}t} = u_{d,i}$$

$$m_d \frac{\mathrm{d}u_{d,i}}{\mathrm{d}t} = F_{g,d,i}$$

$$\frac{\mathrm{d}m_d}{\mathrm{d}t} = 2\pi\rho Dr_d Sh_d B_M \qquad (2.24)$$

$$\frac{\mathrm{d}T_d}{\mathrm{d}t} = \frac{4\pi r_d^2}{m_d c_{liq}} \left[\rho_d \frac{\mathrm{d}r_d}{\mathrm{d}t} L_{vap} + \frac{\lambda_g (T - T_d) Nu_d}{2r_d} \right]$$

where the subscript d indicates droplet values: r_d, u_d, m_d and T_d are the droplet radius, velocity, mass and temperature respectively. The drag force F_{gd} exerted by the carrier fluid is given by

$$F_{gd,i} = \frac{1}{2}\rho C_D A_d |u_i - u_{d,i}|(u_i - u_{d,i}) \qquad (2.25)$$

where A_d is the frontal area of the droplets, and C_D is the drag coefficient, which is calculated according to the expression

$$C_D = \frac{24}{Re_d}\left(1 + \frac{1}{6}Re_d^{2/3}\right) \qquad (2.26)$$

where Re_d is the Reynolds number defined as

$$Re_d = \frac{2\rho|\vec{u} - \vec{u}_d|r_d}{\mu} \qquad (2.27)$$

In equation 2.24 the Sherwood number Sh is calculated using the expression

$$Sh_d = (2 + 0.6Re^{1/2}Sc^{1/3})\frac{\ln(1 + B_M)}{B_M} \qquad (2.28)$$

where $Sc = \mu/\rho D$ is the Schmidt number and D is the diffusivity of the gas-phase fuel in the carrier fluid. Also, B_M is the mass transfer number defined as

$$B_M = \frac{Y_{FS} - Y_{F\infty}}{1 - Y_{FS}} \qquad (2.29)$$

where $Y_{F\infty}$ is the fuel vapor mass fraction of the fluid, and Y_{FS} is the fuel vapor mass fraction at the droplet surface given by

$$Y_{FS} = \frac{W_{FV}}{W_{FV} + W_{GAS}(p/p_{st} - 1)} \qquad (2.30)$$

In the foregoing W_{FV} is the fuel vapor molecular weight; W_{GAS} is the molecular weight of the gas mixture; p_{st} is the saturation pressure for a droplet temperature T_d; c_{liq} and L_{vap} are the specific heat and specific latent heat of the droplets; and Nu_d is the Nusselt number, calculated by

$$Nu_d = (2 + 0.6 Re^{1/2} Pr^{1/3}) \frac{\ln(1 + B_M)}{B_M} \qquad (2.31)$$

A weighted temperature is employed to calculate the gas fluid properties when the surface temperature is required:

$$T_{AVG} = \frac{T_g + 2T_d}{3} \qquad (2.32)$$

2.2.5.2   Gas Phase Equations

For the gas phase, we include an additional (interaction) term in the mass, momentum, energy and species equations.

$$\frac{\partial \rho}{\partial t} + \frac{\partial}{\partial x_j}(\rho u_j) = \psi_\rho \qquad (2.33)$$

34

$$\frac{\partial}{\partial t}(\rho Y_k) + \frac{\partial}{\partial x_j}(\rho Y_k u_j) = -\frac{\partial}{\partial x_j}(\rho Y_k V_{k,j}) + \dot{\omega}_k; 1 \le k \le N_s + \psi_\rho \delta_{n,vapor} \qquad (2.34)$$

$$\frac{\partial}{\partial t}(\rho u_i) + \frac{\partial}{\partial x_j}(\rho u_i u_j) = -\frac{\partial p}{\partial x_i} + \frac{\partial \tau_{ij}}{\partial x_j} + \rho g_i + \psi_{ui} \qquad (2.35)$$

$$\frac{\partial}{\partial t}(\rho E) + \frac{\partial}{\partial x_j}(\rho E u_j) = -\frac{\partial}{\partial x_j}(p u_j) + \frac{\partial}{\partial x_j}(\tau_{ij} u_i) - \frac{\partial q_j}{\partial x_j} + \rho g_j u_j + \psi_e \qquad (2.36)$$

The interaction terms ψ_ρ, ψ_{ui} and ψ_e are given by

$$\psi_\rho = -\frac{1}{\Delta V} \sum_{k=1}^{n_d} \left(\frac{\mathrm{d}m_d}{\mathrm{d}t}\right)_k \qquad (2.37)$$

$$\psi_{u_i} = -\frac{1}{\Delta V} \sum_{k=1}^{n_d} \left(F_{gd,i} + \frac{\mathrm{d}m_d}{\mathrm{d}t} u_{d,i}\right)_k \qquad (2.38)$$

$$\psi_e = -\frac{1}{\Delta V} \sum_1^{n_d} \left[\frac{d(m_d h_d)}{dt} + F_{gd} u_{d,i} + \frac{dm_d}{dt}\left(\frac{1}{2}u_{d,i}^2\right)\right]_k \qquad (2.39)$$

The balance are done over a control volume ΔV, because the lagrangian quantities dealt with here are point sources, and will lead to discontinuities if they are not averaged out suitably [109]. The averaging is done by using local integrals.

2.3   Author's Contributions to DNS Solver Development

In the foregoing sections, the physical and numerical models present in the DNS solver used in the current work was described. It is pertinent to point out the

author's contribution to the DNS-solver development as part of this PhD, and to some extent acknowledge the efforts of the others in the development.

The author was responsible for the development of parts of the DNS code pertaining to the radiation and droplet solvers. The radiation solver -which contains an implementation of the Discrete Transfer Method (DTM)- was developed by Yi Wang (who had also developed the soot modules) during the course of his PhD (who was also advised by the author's adviser and of whom the candidate is a successor) [107]. This solver was improved upon, debugged where necessary by the candidate, and implemented to carry out simulations of nonpremixed flames (including the development of associated code such as postprocessors).

The candidate had obtained an implentation of the lagrangian droplet solver developed by the group stationed at the University of Wisconsin, Madison (spearheaded by Dr. Chris Rutland) which had lead the original development efforts for the droplet solver. The original development was for dilute fuel sprays. The candidate was responsible for the adaptation of this code to the water-spray framework, used in the current work. This was done in collaboration with Paul Arias (also, a PhD candidate) at the University of Michigan, Ann Arbor and his adviser Dr. Hong Im. Notably, Dr. Im's group was also responsible for developing the Discrete Ordinates Method (DOM) implentation for the DNS solver.

The portions of code pertaining to detailed chemistry were obtained from Tianfeng Liu and coworkers (now at the University of Connecticut).

It is also to be noted that the development effort for S3D as a whole is headed by Dr. Jacqueline Chen's group stationed at Sandia National Laboratories, and to

whom gratitude is expressed.

The simulations were carried out almost entirely in the machines at the National Energy Research Scientific Computing Center (NERSC) run by the Lawrence Berkeley National Laboratories. The candidate had used (primarily) Seaborg and Bassi until they were decommissioned, and currently uses Franklin and Hopper for his simulations.

Chapter 3

Activation Energy Asymptotics of Radiative Extinction in Laminar

Counteflow Diffusion Flames

3.1 Introduction

The objective of this chapter is to describe how Activation Energy Asymptotics (AEA) theory may be used to describe kinetic and radiative extinction for laminar counterflow diffusion flames. The AEA analysis assumes single-step global combustion chemistry, constant heat capacity and Sjunity Lewis numbers; it also includes a two-equation phenomenological model to describe soot formation, growth and oxidation processes, as well as a generalized treatment of thermal radiation that assumes spectrally-averaged gray-medium properties and applies to flames with an arbitrary optical thickness. The aim is to set up the theoretical framework for laminar counterflow diffusion flames, insofar as to derive extinction criteria in non-adiabatic, radiating configurations. One wishes to shed light on the dual extinction limits comprising kinetic extinction at high stretch, and kinetic or radiative extinction at low stretch. It is of interest to draw upon the analysis to produce an extinction criterion for use in DNS, for non-adiabatic configurations (turbulent soot loading in Chapter 6, and evaporative cooling from water-spray in Chapter 7).

In this connection, reference is made to similar asymptotic analyses discussed

in [53, 19, 17, 57, 111, 22, 73, 30, 89, 54]. Various combusting confugrations are featured in these works, such as a condensed liquid fuel [30], counterflow planar flames [53, 57, 111, 89], spherical burning droplets [22], and more general one-dimensional descriptions (such as a strip of burning fuel) [19, 17], and flamelet descriptions that are independent of coordinate frame [73, 75]. In all these works, the equations are recast into a one-dimensional form suitable for asymptotic analysis. Constant density, single-step fuel-air chemistry are common assumptions. Variable density formulations can be included by means of the Howarth transformation [9] [19, 17] by defining a modified density weighted coordinate. One may also carry out a Crocco transformation to obtain a description in mixture fraction space, or the laminar flamelet [73, 75]. Time dependent configurations are addressed in [19, 54] by use of Fourier-Laplace transforms.

Investigations on radiative extinction have hitherto been carried out from the purview of AEA, by means of singular perturbation around the flame zone [57, 111, 22, 89] in a steady framework. In these investigations, the radiation source term is treated as a singular quantity around the flame, with the thickness of the radiating zone being much larger than the reaction zone, but small compared to the convective or flow length scale. This entails the use of the optically thin radiation assumption, where absorption effects are negligible. The current work distinguishes itself from the aforementioned investigations, in its treatment of the radiation source term, in that both emission and absorption are resolved (the optically thin assumption is not made), the latter of which requires solving the radiation transport equation (RTE) [66]. Also, unlike in those investigations, where the radiation source term is treated

as a singular quantity around the flame, the resolution of the absorption term by means of the RTE takes into account the *non-locality* of radiation absorption around the flame.

The analysis is then used in subsequent chapters to interpret kinetic and radiative extinction in laminar and turbulent configurations under conditions where the flames are loaded with non-locally generated soot (as would be reminescent of a fire, where soot at the flame originates elsewhere, and is transported into the flame).

3.2 Problem Formulation

The problem uses conventional treatment using singular perturbation, the so called Activation Energy Asymptotics (AEA) approach, in which the flame is decomposed into the outer and inner regions and resolved by matched asymptotic expansions. As has been mentioned in Chapter 1 this corresponds to the configuration C1. The configuration of interest is a counterflow diffusion flame, with fuel (Ethylene) and oxidizer (air) being supplied from the left and right respectively. This non-premixed combustion system is assumed to be described by a single-step global chemical reaction [112] as follows .

$$C_2H_4 + 3O_2 \rightarrow 2CO_2 + 2H_2O$$
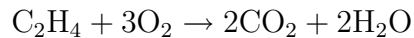
3.3 Governing Equations

The equations comprise those of mass, momentum and energy, as would be expected for a gas phase combustion problem. Transformations are made appropri-
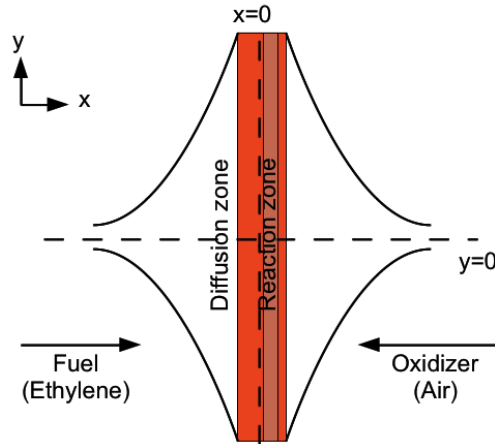
Figure 3.1: Schematic of counterflow flame. The flame (shaded brown) is located to the right of the stagnation flame (dashed lines). The reaction zone is embedded in a much thicker diffusion zone (shaded red)

ately to simplify the treatment for variable density for the outer non-reacting scales using the Howarth transformation; and a flamelet type transformation is applied to describe the the inner regions in mixture fraction space. In addition to these, the radiation transfer equation is solved in order to resolve radiation emission and absorption.

3.3.1 Howarth Transformation

Density weighted coordinates are used, in conformity with Carrier, Fendell and Marble [19] that greatly simplifies the analysis. The reason for using this transformation is that mass weighted coordinates help in treating variable density flows, and one need not resort to assuming $\rho = constant$, as is done in some works [53, 57, 111]. The transformation is described here in brief [9].

Consider a two dimensional counterflow flame configuration in which the flame normal is along the x direction; u and v being the velocities in the x and y directions and ρ being the density. The continuity equation is

$$\frac{\partial \rho}{\partial t} + \frac{\partial(\rho u)}{\partial x} + \frac{\partial(\rho v)}{\partial y} = 0 \tag{3.1}$$

A mass weighted coordinate ξ is defined as

$$\xi = \int_0^x \frac{\rho}{\rho_2} \mathrm{d}x \tag{3.2}$$

where ρ_2 is the density of the oxidizer stream, which is denoted by the subscript 2, while $x = 0$ is the location of the stagnation plane. Transform the equations into this coordinate system comprised of $X = \xi, Y = y$ and $\mathcal{T} = t$ with the following transformation rules

$$
\begin{aligned}
x = x(\xi, Y, \mathcal{T}) \Rightarrow \frac{\partial}{\partial x} &= \frac{\partial}{\partial \xi}\frac{\partial \xi}{\partial x} + \frac{\partial}{\partial Y}\frac{\partial Y}{\partial x} + \frac{\partial}{\partial \mathcal{T}}\frac{\partial T}{\partial x} \\
&= \frac{\partial}{\partial \xi}\frac{\partial \xi}{\partial x} \\
&= \frac{\rho}{\rho_2}\frac{\partial}{\partial \xi}
\end{aligned}
\tag{3.3}
$$

$$
\begin{aligned}
y = y(\xi, Y, t) \Rightarrow \frac{\partial}{\partial y} &= \frac{\partial}{\partial \xi}\frac{\partial \xi}{\partial y} + \frac{\partial}{\partial Y}\frac{\partial Y}{\partial y} + \frac{\partial}{\partial \mathcal{T}}\frac{\partial \mathcal{T}}{\partial y} \\
&= \frac{\partial}{\partial \xi}\frac{\partial \xi}{\partial y} + \frac{\partial}{\partial Y}
\end{aligned}
\tag{3.4}
$$

$$
\begin{aligned}
t = t(\xi, Y, \mathcal{T}) \Rightarrow \frac{\partial}{\partial t} &= \frac{\partial}{\partial \xi}\frac{\partial \xi}{\partial t} + \frac{\partial}{\partial Y}\frac{\partial Y}{\partial t} + \frac{\partial}{\partial \mathcal{T}}\frac{\partial \mathcal{T}}{\partial t} \\
&= \frac{\partial}{\partial \xi}\frac{\partial \xi}{\partial t} + \frac{\partial}{\partial \mathcal{T}}
\end{aligned}
\tag{3.5}
$$

The continuity equation becomes, together with equation (3.2)

$$\frac{\partial}{\partial x}\left(\rho u + \rho_2 \frac{\partial \xi}{\partial t}\right) + \frac{\partial(\rho v)}{\partial y} = 0 \tag{3.6}$$

42

Now one may define a stream function $\psi(x, y, t)$ as follows

$$\rho_2 \frac{\partial \psi}{\partial x} = \rho v; \qquad \rho_2 \frac{\partial \psi}{\partial x} = -(\rho u + \rho_2 \frac{\partial \xi}{\partial t}) \tag{3.7}$$

Together with equation (3.2) the this gives

$$\frac{\partial \psi}{\partial \xi} = v \tag{3.8}$$

One can now define a normal transformed velocity $U(\xi, Y, \mathcal{T})$ as

$$\frac{\partial \psi}{\partial Y} = -U \tag{3.9}$$

A constant density version of the continuity equation may now be written as

$$\frac{\partial v}{\partial Y} + \frac{\partial U}{\partial \xi} = 0 \tag{3.10}$$

The velocity U is obtained from the equation (3.7) as

$$U = \frac{1}{\rho_2} \frac{\partial \xi}{\partial t} + \frac{\rho}{\rho_2} u + v \frac{\partial \xi}{\partial y} \tag{3.11}$$

The continuity equation may now be cast into a form, after suitable manipulation, to preserve the convective derivative to obtain

$$\frac{\mathrm{D}}{\mathrm{D}t} = \frac{\partial}{\partial \mathcal{T}} + U \frac{\partial}{\partial \xi} + v \frac{\partial}{\partial Y} \equiv \frac{\tilde{\mathrm{D}}}{\tilde{\mathrm{D}}\mathcal{T}} \tag{3.12}$$

3.3.2 Applying Howarth transform to Governing Equations

The governing equations are manipulated by invoking one-dimensionality, so that all quantities (except the velocities) vary only in the x direction, which is normal to the flame. The velocity in the direction normal to the flame in this new coordinate system is obtained from the equation (3.10) as

$$U = -\int_0^\xi \frac{\partial v}{\partial Y} \mathrm{d}\xi \tag{3.13}$$

43

If a constant strain rate $\partial v / \partial Y = \alpha$, together with a reference velocity of zero at $\xi = 0$, is assumed, one gets at the stagnation plane location $x = 0$

$$U = \int_0^\xi \frac{\partial v}{\partial Y} d\xi = -\alpha \xi \tag{3.14}$$

In the undermentioned, $\mathcal{T}$ and Y are replaced later by t and y to retain the usual notation. The transport operator is now transformed into mass weighted coordinates. As mentioned in the foregoing, quantities of interest are only assumed to depend on x and t. Furthermore, unity Lewis numbers are assumed so that the diffusion coefficient may be denoted by a quantity D. Define a tranpsort ooperator L as follows

$$\rho L \equiv \rho \frac{\partial}{\partial t} + \rho u \frac{\partial}{\partial x} - \frac{\partial}{\partial x} \left(D\rho \frac{\partial}{\partial x} \right) - \frac{\partial}{\partial y} \left(D\rho \frac{\partial}{\partial y} \right) \tag{3.15}$$

Upon introducing the Howarth transformation (3.2), and ignoring Y dependence, one gets

$$\rho \frac{\partial}{\partial t} + \rho u \frac{\partial}{\partial x} = \rho \left(\frac{\partial}{\partial \mathcal{T}} - \alpha \xi \frac{\partial}{\partial \xi} \right) \tag{3.16}$$

The diffusion terms are manipulated, using the transformation (3.2) as follows

$$\frac{\partial}{\partial x} \left(\rho D \frac{\partial}{\partial x} \right) = \frac{\rho}{\rho_2} \frac{\partial}{\partial \xi} \left(D\rho \frac{\rho}{\rho_2} \frac{\partial}{\partial \xi} \right)$$
$$= \frac{\rho}{\rho_2^2} \frac{\partial}{\partial \xi} \left(D\rho^2 \frac{\partial}{\partial \xi} \right) \tag{3.17}$$

Now, if one makes the simplification that $D\rho^2$ is nearly constant in flows of interest, one may remove this quantity as $D\rho^2 = D_2 \rho_2^2$. One may replace $\mathcal{T}$ with t to obtain

$$L \equiv \frac{\partial}{\partial t} - \alpha \xi \frac{\partial}{\partial \xi} - D_2 \frac{\partial^2}{\partial \xi^2} \tag{3.18}$$

44

3.3.3 Non-dimensionalization

The governing equations for species mass and energy are

$$\rho L(Y_F) = -\dot\omega_F$$

$$\rho L(Y_{O_2}) = -r_s\dot\omega_F \tag{3.19}$$

$$\rho L(h) = \Delta H_F \dot\omega_F + \nabla \cdot \vec{q}_R$$

where Y_F, Y_{O_2} are the fuel and oxidizer mass fractions respectively; $h = \int_0^T c_p \mathrm{d}T = c_p T$ the enthalpy for material at temperature T, for a constant specific heat $c_p = 1008\ \mathrm{J/kg-k}$, based on some reference enthalpy at temperature $T_0 = 0$; $\Delta H_F = 32.7\ \mathrm{MJ/kg}$ is the heat of combustion per unit mass of fuel (a positive quantity); $\dot\omega_F$ is the fuel mass burning rate per unit volume; r_s is the stoichiometric fuel-oxygen coefficient in the chemical reaction. The non-dimensional quantities are superscripted by primes

$$\rho' = \frac{\rho}{\rho_2}; \qquad \xi' = \frac{\xi}{\ell}; \qquad t' = \alpha t$$

$$Y_F' = \frac{Y_F}{Y_{F,1}}; \qquad Y_{O_2}' = \frac{Y_{O_2}}{r_s Y_{F,1}}; \qquad Y_{CO_2}' = \frac{Y_{CO_2}}{r_{CO_2} Y_{F,1}} \tag{3.20}$$

$$Y_{H_2O}' = \frac{Y_{H_2O}}{r_{H_2O} Y_{F,1}}; \qquad T' = \frac{c_p T}{\Delta H_F Y_{F,1}}$$

In the foregoing equations, ℓ is a reference convective length scale (to be defined), and quantities subscripted with $1, 2$ are reference quanties at the fuel and oxidizer boundaries respectively: $Y_{F,1} = Y_F(\xi = -\infty)$, $\rho_2 = \rho(\xi = \infty)$. The convective length scale ℓ is defined based on the aforementioned quantities as

$$\ell = \sqrt{\frac{D_2}{\alpha}} \tag{3.21}$$

In the foregoing, the oxidizer stream's diffusivity is $D_2 = 2.21 \times 10^{-5}$ m^2/s. The reaction term is taken to be of the following form, proposed in [112]

$$\dot{\omega}_F = \frac{A}{(10^6)^{p+q-1}} \times M_F \left(\frac{\rho Y_F}{M_F}\right)^p \left(\frac{\rho Y_{O_2}}{M_{O_2}}\right)^q \exp\left(-\frac{T_a}{T}\right) \qquad (3.22)$$

where $A = 2.0 \times 10^{12}$ (mol/m^3)$^{1-p-q}$ s^{-1} is a model coefficient, p, q are the model fuel and oxidizer exponents, $p = 0.1$, $q = 1.65$, M_k the molecular weight of species k (kg/mol), and T_a a model activation temperature, $T_a = 15107$ K. Collecting terms in the above equation so that

$$B = \frac{A}{(10^6)^{p+q-1}} M_F \qquad (3.23)$$

the reaction source term $\dot{\omega}_F$ may be written as

$$\dot{\omega}_F = B \left(\frac{\rho Y_F}{M_F}\right)^p \left(\frac{\rho Y_{O_2}}{M_{O_2}}\right)^q \exp\left(-\frac{T_a}{T}\right) \qquad (3.24)$$

3.4   Solution Approach

The governing equations are solved using matched asymptotic expansions [12] in conventional fashion. Here, the outer regions comprise the radiatively active layer, while the inner region is the thin reacting zone, which forms a *corner* boundary layer whose location is to be determined (which, however, may be intuitively viewed as the region where fuel and oxidizer mix in stoichiometric proportions). An implicit assumption here is that the length scale for radiation is much larger than that of the reaction zone, the fallout of which assumption is that the radiation term is dwarfed by the reaction term inside the inner layer (except, perhaps in regions where the optical thickness is large, which is not considered presently). The outer and inner

problems are thus posed by appropriately expressing the governing equations. They are then matched to arrive at the complete solution.

3.5   Outer Solutions

The outer solutions are derived as follows, using the Howarth transformed equation (3.18).

$$\rho L(Y_F) = -\dot{\omega}_F$$

$$\rho L(Y_{O_2}) = -r_s \dot{\omega}_F \tag{3.25}$$

$$\rho L(h) = \Delta H_F \dot{\omega}_F + \nabla \cdot \vec{q}_R$$

where

$$L \equiv -\alpha\xi \frac{\mathrm{d}}{\mathrm{d}\xi} - D_2 \frac{\mathrm{d}^2}{\mathrm{d}\xi^2} \tag{3.26}$$

In the above, the time dependency is removed since the problem under consideration is a steady counterflow flame. However, it may be added if desired.

After non-dimensionalizing, and abstracting the reaction source term into a Dirac-delta function $\delta(\xi - \xi_f)$, which is zero everywhere, except at the flame located at ξ_f where it is infinite, one gets

$$\rho L'(Y'_F) = A_r \delta(\xi - \xi_f)$$

$$\rho L'(Y'_{O_2}) = A_r \delta(\xi - \xi_f) \tag{3.27}$$

$$\rho L'(T') = -A_r \delta(\xi - \xi_f) + \frac{1}{\Delta H_F \alpha Y_{F,1}} \nabla \cdot \vec{q}_R$$

where

$$L' \equiv -\xi' \frac{\mathrm{d}}{\mathrm{d}\xi'} - \frac{\mathrm{d}^2}{\mathrm{d}\xi'^2} \tag{3.28}$$

and A_r is a quantity that denotes the strength of the chemical reaction (added for consistency reasons).

In the forthcoming developments, a non-dimensional notation for the outer variables of interest is defined as follows

$$\xi' \to \zeta; \qquad L' \to \hat{L}; \qquad Y_F' \to \hat{Y}_F$$

$$Y_{O_2}' \to \hat{Y}_{O_2}; \qquad Y_{CO_2}' \to \hat{Y}_{CO_2}; \qquad Y_{H_2O}' \to \hat{Y}_{H_2O}; \qquad (3.29)$$

$$T' \to \hat{T}; \qquad \rho' \to \hat{\rho}$$

With these definitions, the outer equations are rewritten as

$$\hat{L}(\hat{Y}_F) = 0$$

$$\hat{L}(\hat{Y}_{O_2}) = 0 \qquad (3.30)$$

$$\hat{L}(\hat{T}) = \frac{1}{\alpha\hat{\rho}}\nabla \cdot \vec{q}_R$$

subject to the boundary conditions

$$\hat{Y}_F(-\infty) = Y_F'(-\infty) = Y_{F,-\infty}'; \qquad \hat{Y}_F(\infty) = Y_F'(\infty) = Y_{F,\infty}' = 0$$

$$\hat{Y}_{O_2}(-\infty) = Y_{O_2}'(-\infty) = Y_{O_2,-\infty}' = 0; \qquad \hat{Y}_{O_2}(\infty) = Y_{O_2}'(\infty) = Y_{O_2,\infty}' \qquad (3.31)$$

$$\hat{T}(-\infty) = T'(-\infty) = T_{-\infty}'; \qquad \hat{T}(\infty) = T'(\infty) = T_\infty'$$

It is noted that the reaction source term, contained in the Dirac-delta function is non-existent in the outer equations. However, since these equations are solved on either side of the flame, one needs to know the values taken by the variables at the flame, which is done in the forthcoming.

3.5.1 Flame Location

The flame location is determined using the Shvab-Zeldovich coupling relationships contained in equations (3.27).

$$L'(Y_F' - Y_{O_2}') = 0 \tag{3.32}$$

The quantity in the paranthesis $Y_F' - Y_{O_2}'$ is well behaved thoughout the domain and varies in the outer scale. Using appropriate boundary conditions for fuel and oxidizer (which are entirely known), one may solve the above equation to get

$$Y_F' - Y_{O_2}' = \frac{Y_{F,-\infty}' - Y_{O_2,\infty}'}{2} - \frac{Y_{F,-\infty}' + Y_{O_2,\infty}'}{2} \, \mathrm{erf}\left(\frac{\xi'}{\sqrt{2}}\right) \tag{3.33}$$

The flame location is taken to be that where fuel and oxidizer both simultaneously vanish to leading order. If this is used in the foregoing equation, one gets

$$\mathrm{erf}\left(\frac{\xi_f'}{\sqrt{2}}\right) = \frac{Y_{F,-\infty}' - Y_{O_2,\infty}'}{Y_{F,-\infty}' + Y_{O_2,\infty}'} \tag{3.34}$$

which gives the flame location. It is noted that this occurs at the stoichiometric location, as it would even without radiation heat losses. The flame location is henceforth denoted by the subscript st. Also, the quantity on the LHS of equation (3.33) is essentially a restatement of the mixture fraction, defined below so that the mixture fraction Z is zero in the air stream, and unity in the fuel stream.

$$Z = \frac{Y_F' - Y_{O_2}' + Y_{O_2,\infty}'}{Y_{F,-\infty}' + Y_{O_2,\infty}'} \tag{3.35}$$

The mixture fraction profile may then be expressed by the relationship

$$Z = \frac{1}{2}\left[1 - \mathrm{erf}\left(\frac{\xi'}{\sqrt{2}}\right)\right] \tag{3.36}$$

3.5.2 Quantities at the Flame Location

This is done analogously to the above.

$$L'(Y_F' + T'^0) = 0 \tag{3.37}$$

where T'^0 is the non-dimensional flame temperature (the outer solutions of which are which are expressed in the same notation as defined in the foregoing, i.e. by inserting a caret symbol âbove the variable) in the absence of radiation. This is the so called Burke-Schumann flame temperature for the adiabatic flame. One gets the adiabatic flame temperature upon solving this equation and substituting for values at the stoichiometric location.

The boundary conditions for the foregoing equation are

$$
\begin{aligned}
Y_{F,-\infty}' = Y_F'(-\infty); \qquad & Y_{F,\infty}' = Y_F'(\infty) \\
T^{0'}(-\infty) = T'(-\infty); \qquad & T^{0'}(\infty) = T'(\infty)
\end{aligned}
\tag{3.38}
$$

The solution can be written as

$$T^{0'} + Y_F' = \frac{T_\infty' - T_{-\infty}' - Y_{F,-\infty}'}{2} \operatorname{erf}\left(\frac{\xi'}{\sqrt{2}}\right) + \frac{T_{-\infty}' + T_\infty' + Y_{F,-\infty}'}{2} \tag{3.39}$$

The flame location can be inserted from equation (3.34), after recognizing that $\hat{Y}_{F,st} = 0$, to get the non-dimensional adiabatic flame temperature $\hat{T}_{st}^0$ as

$$\hat{T}_{st}^0 = \frac{T_\infty' - T_{-\infty}' - Y_{F,-\infty}'}{2} \left(\frac{Y_{F,-\infty}' - Y_{O_2,\infty}'}{Y_{F,-\infty}' + Y_{O_2,\infty}'}\right) + \frac{T_{-\infty}' + T_\infty' + Y_{F,-\infty}'}{2} \tag{3.40}$$

In similar fashion, one may also obtain the values at the flame location for other quantities, such as $\hat{Y}_{CO_2,st}$ and $\hat{Y}_{H_2O,st}$.

3.5.3 Non-radiating Solutions

The solutions to the non-radiating problem are to be obtained for use in the radiating problem. These are the so called Burke-Schumann solutions for the unstrained problem far from the reaction zone.

The equations to be solved are

$$\hat{L}(\hat{Y}_F) = 0$$

$$\hat{L}(\hat{Y}_{O_2}) = 0$$

$$\hat{L}(\hat{Y}_{CO_2}) = 0 \tag{3.41}$$

$$\hat{L}(\hat{Y}_{H_2O}) = 0$$

$$\hat{L}(\hat{T}^0) = 0$$

$\hat{T}^0$ is the *outer* 'adiabatic' or radiation free solution to the outer energy equation. This must be distinguished from $\hat{T}$, which also contains within it the effects of radiation. The species mass fractions remain the same in both the radiating and non-radiating solutions because their outer equations are unchanged in the presence of radiation. However, the energy equation will have to be revisited because alterations are effected by the radiation source term.

The outer solutions are characterized by a slope discontinuity on either side of the flame, which will have to be corrected by patching with the inner solution. The non-radiating solutions may be written as follows

$$\hat{Y}_F = Y'_{F,-\infty} \frac{\text{erf}\left(\frac{\zeta_{st}}{\sqrt{2}}\right) - \text{erf}\left(\frac{\zeta}{\sqrt{2}}\right)}{1 + \text{erf}\left(\frac{\zeta_{st}}{\sqrt{2}}\right)}; \qquad\qquad \zeta < \zeta_{st}$$

$$= 0; \qquad\qquad\qquad\qquad\qquad\qquad\qquad \zeta \geq \zeta_{st} \tag{3.42}$$

$$\hat{Y}_{O_2} = 0; \qquad\qquad\qquad\qquad\qquad\qquad\qquad\qquad \zeta < \zeta_{st}$$

$$= Y'_{O_2,\infty} \frac{\mathrm{erf}\left(\frac{\zeta}{\sqrt{2}}\right) - \mathrm{erf}\left(\frac{\zeta_{st}}{\sqrt{2}}\right)}{1 - \mathrm{erf}\left(\frac{\zeta_{st}}{\sqrt{2}}\right)}; \qquad\qquad\qquad \zeta \geq \zeta_{st} \tag{3.43}$$

$$\hat{Y}_{CO_2} = \hat{Y}_{CO_2,st} \frac{1 + \mathrm{erf}\left(\frac{\zeta}{\sqrt{2}}\right)}{1 + \mathrm{erf}\left(\frac{\zeta_{st}}{\sqrt{2}}\right)}; \qquad\qquad\qquad \zeta < \zeta_{st}$$

$$= \hat{Y}_{CO_2,st} \frac{\mathrm{erf}\left(\frac{\zeta}{\sqrt{2}}\right) - \mathrm{erf}\left(\frac{\zeta_{st}}{\sqrt{2}}\right)}{1 - \mathrm{erf}\left(\frac{\zeta_{st}}{\sqrt{2}}\right)}; \qquad\qquad\qquad \zeta \geq \zeta_{st} \tag{3.44}$$

$$\hat{Y}_{H_2O} = \hat{Y}_{H_2O,st} \frac{1 + \mathrm{erf}\left(\frac{\zeta}{\sqrt{2}}\right)}{1 + \mathrm{erf}\left(\frac{\zeta_{st}}{\sqrt{2}}\right)}; \qquad\qquad\qquad \zeta < \zeta_{st}$$

$$= \hat{Y}_{H_2O,st} \frac{\mathrm{erf}\left(\frac{\zeta}{\sqrt{2}}\right) - \mathrm{erf}\left(\frac{\zeta_{st}}{\sqrt{2}}\right)}{1 - \mathrm{erf}\left(\frac{\zeta_{st}}{\sqrt{2}}\right)}; \qquad\qquad\qquad \zeta \geq \zeta_{st} \tag{3.45}$$

$$\hat{T}^0 = \hat{T}^0_{st} \frac{1 + \mathrm{erf}\left(\frac{\zeta}{\sqrt{2}}\right)}{1 + \mathrm{erf}\left(\frac{\zeta_*}{\sqrt{2}}\right)} + T'_{-\infty} \frac{\mathrm{erf}\left(\frac{\zeta_{st}}{\sqrt{2}}\right) - \mathrm{erf}\left(\frac{\zeta}{\sqrt{2}}\right)}{1 + \mathrm{erf}\left(\frac{\zeta_{st}}{\sqrt{2}}\right)}; \quad \zeta < \zeta_{st}$$

$$= \hat{T}^0_{st} \frac{1 - \mathrm{erf}\left(\frac{\zeta}{\sqrt{2}}\right)}{1 - \mathrm{erf}\left(\frac{\zeta_{st}}{\sqrt{2}}\right)} + T'_{\infty} \frac{\mathrm{erf}\left(\frac{\zeta}{\sqrt{2}}\right) - \mathrm{erf}\left(\frac{\zeta_{st}}{\sqrt{2}}\right)}{1 - \mathrm{erf}\left(\frac{\zeta_{st}}{\sqrt{2}}\right)}; \quad \zeta \geq \zeta_{st} \tag{3.46}$$

3.5.4 Radiation Source Term

The radiation source term is given by the expression

$$\nabla \cdot \vec{q}_R = -\kappa(4\sigma T^4 - G) \tag{3.47}$$

where κ is the Planck mean absorption coefficient (described below) and G is the integrated incident radiation. κ comprises contributions from gas radiation (in this

case, CO_2 and H_2O), and a contribution from soot luminosity (which is typically the dominant part).

$$\kappa = p(x_{CO_2}a_{CO_2} + x_{H_2O}a_{H_2O}) + C_{soot}f_vT \qquad (3.48)$$

where p is pressure (atm), x_k the mole fraction of species k, a_k is described by curve-fit expression given in [1]. C_{soot} is a quantity that may be tuned in order to make the medium more, or less radiating during numerical experiments, f_v is the soot volume fraction. Unless otherwise mentioned, a value of $C_{soot} = 1817 \text{ m}^{-1}\text{K}^{-1}$ (based on recent measurements [88]) is used in the current work.

The two terms on the right hand side of Equation (3.47) are the contributions from emission and absorption. The emission term contains the T^4 dependence on flame temperature and is computable once we know that quantity. However, the radiation absorption term G is in general, non-local, although under special conditions (optically thin flames) it may be approximated. But in a general case, one obtains it by solving the radiative transport equation (RTE), detailed in the following.

3.5.4.1 Obtaining Radiation Heat Fluxes by Solving RTE

An expression for radiant energy absorption is developed below for the laminar counterflow flame configuration. This expression may be used in the outer energy equation in order to compute the temperature field predicated by radiation losses.

The radiation transport equation in the absence of scattering is

$$\frac{\mathrm{d}I(s)}{\mathrm{d}s} = \kappa(s)(I_b(s) - I(s)) \qquad (3.49)$$

where I is the intensity of a ray traveling in the direction $\hat{s}$, s being a coordinate defined in the direction of the ray's path, κ is the Planck mean absorption coefficient, $I_b = \sigma T^4/\pi$ being the black-body intensity at temperature T, with σ being the Stephen-Boltzmann constant. Since this is an entirely symmetric problem, one may alternatively recast the above in terms of x and the polar angle θ. The azimuthal angle ϕ will not appear in the expression because of symmetry, and will be integrated out. Note that the analysis now uses dimensional coordinates.

Considering an angle $0 < \theta < \pi/2$, one may write

$$dx = -\frac{ds}{\cos\theta} \tag{3.50}$$

and

$$-\cos\theta\frac{dI}{dx} = \kappa(I_b - I) \tag{3.51}$$

Define the optical thickness $\tau(x)$ as

$$\tau(x) = \int_0^x \kappa(x')dx' \tag{3.52}$$

so that

$$d\tau(x') = \kappa(x')dx' \tag{3.53}$$

Also, define a shorthand notation for τ as follows

$$\tau = \tau(x), \qquad \tau' = \tau(x') \tag{3.54}$$

Multiplying both sides of equation (3.51) by $\exp(-\tau/\cos\theta)$ and grouping terms, one gets

$$\frac{d}{d\tau}\left[I\exp\left(-\frac{\tau}{\cos\theta}\right)\right] = \left(-\frac{I_b}{\cos\theta}\right)\exp\left(-\frac{\tau}{\cos\theta}\right) \tag{3.55}$$

which can be integrated as

$$\int_{\infty}^{\tau} \frac{\mathrm{d}}{\mathrm{d}\tau'} \left(I e^{-\frac{\tau'}{\cos\theta}} \right) \mathrm{d}\tau' = -\int_{\infty}^{\tau} \frac{I_b}{\cos\theta} e^{-\frac{\tau'}{\cos\theta}} \mathrm{d}\tau' \tag{3.56}$$

giving

$$I[\tau(x)] = \int_{\tau(x)}^{\infty} \frac{I_b(\tau')}{\cos\theta} \exp\left(-\frac{\tau(x') - \tau(x)}{\cos\theta} \right) \mathrm{d}\tau' \tag{3.57}$$

This is only the contribution from the *right* of the point x. One may likewise derive an expression for the contribution from the left of x. The subscript $+$ and $-$ shall henceforth be used to mark this distinction.

3.5.4.2 Absorption Source Term

The absorption source term is derived by taking the integral of the intensity in solid angle space as follows (similar expressions are available in [66])

$$S_{R,A} = \kappa G = \kappa \int_{\Omega} I \mathrm{d}\Omega \tag{3.58}$$

If one calls the contributions to the radiation source term from the left and right as q_- and q_+ respectively, one has

$$S_{R,A} = q_- + q_+ \tag{3.59}$$

The derivation for q_+ is shown in the following. q_- may be obtained similarly.

$$\begin{aligned}
q_+ &= \int_0^{\frac{\pi}{2}} I_+(x) \sin\theta \mathrm{d}\theta \int_0^{2\pi} \mathrm{d}\phi \\
&= 2\pi\kappa \int_{\tau}^{\infty} \int_0^{\frac{\pi}{2}} \frac{I_b}{\cos\theta} \exp\left(-\frac{\tau' - \tau}{\cos\theta} \right) \sin\theta \mathrm{d}\tau' \mathrm{d}\theta
\end{aligned} \tag{3.60}$$

One now makes the transformation

$$t = \frac{\tau' - \tau}{\cos\theta} \tag{3.61}$$

55
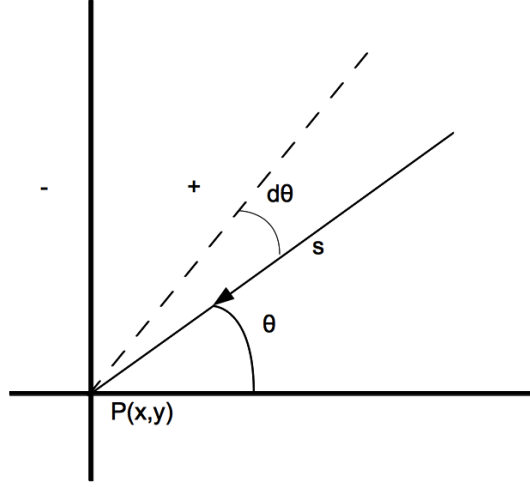
Figure 3.2: Schematic of domain and setup to calculate radiation absorption by integrating RTE. The left and right of the point under consideration $P(x, y)$ are denoted by '-' and '+' respectively.

to get

$$q_+ = 2\pi\kappa \int_\tau^\infty I_b(\tau') \mathrm{E}_1(\tau' - \tau) \mathrm{d}\tau' \tag{3.62}$$

where E_1 is the exponential integral function defined as follows

$$\mathrm{E}_1(t) = \int_1^\infty \frac{\exp(-tz)}{z} \mathrm{d}z \tag{3.63}$$

One may similarly obtain the expression for q_- as

$$q_- = 2\pi\kappa \int_{-\infty}^\tau I_b(\tau') \mathrm{E}_1(\tau - \tau') \mathrm{d}\tau' \tag{3.64}$$

The radiation absorption source term $S_{R,A}$ then becomes

$$
\begin{aligned}
S_{R,A} &= q_+ + q_- \\
&= 2\pi\kappa \left(\int_{-\infty}^\tau I_b(\tau') \mathrm{E}_1(\tau - \tau') \mathrm{d}\tau' + \int_\tau^\infty I_b(\tau') \mathrm{E}_1(\tau' - \tau) \mathrm{d}\tau' \right)
\end{aligned}
\tag{3.65}
$$

In an optically thin medium with a quasi constant temperature T_∞, and $\tau \to 0$ one may recover the well known expression

$$S_{R,A} = 4\pi\kappa I_b(T = T_\infty) \tag{3.66}$$

since $\int_0^\infty E_1(x)dx = 1$.

3.5.4.3   Transformation into the Howarth Framework

Since the governing equations are expressed in terms of the density weighted coordinate ξ, one needs to transform the foregoing absorption heat source term into that framework. Recognizing that

$$\xi = \int_{-\infty}^x \frac{\rho(x')}{\rho_2} dx' \tag{3.67}$$

and

$$d\tau' = \kappa(x')dx' \tag{3.68}$$

one can write the absorption heat source term (3.65) as

$$\begin{aligned}
S_{R,A} = &\ 2\pi\kappa(\xi) \int_{-\infty}^\xi I_b(\xi')E_1[\tau(\xi) - \tau(\xi')]\kappa(\xi')\frac{\rho_2}{\rho(\xi')}d\xi' \\
&+ 2\kappa(\xi)\pi \int_\xi^\infty I_b(\xi')E_1[\tau(\xi') - \tau(\xi)]\kappa(\xi')\frac{\rho_2}{\rho(\xi')}d\xi'
\end{aligned} \tag{3.69}$$

3.5.5   Radiating Solutions -Solving for the Outer Temperature Field

If the radiation source term is available, one may proceed with solving the outer equations to obtain the outer temperature field. It is clear that the mass fraction profiles are unaltered in the presence of radiation (since the outer equations

are not any different from the case without radiation). The equations to be solved are as follows

$$\hat{L}(\hat{T}) = f(\zeta) \tag{3.70}$$

where f is the radiating term from equation 3.30)

$$f = \frac{\nabla \cdot \vec{q}_R}{\alpha \rho \Delta H_F Y_{F,1}} \tag{3.71}$$

The density is related to the temperature by means of the ideal gas law, at a constant atmospheric pressure P_∞.

$$P_\infty = \rho \frac{R}{M_{mix}} T \tag{3.72}$$

where R is the ideal gas constant, and M_{mix} is the molecular weight of the mixture at any given location.

$$M_{mix} = \frac{1}{\sum_k \frac{Y_k}{M_k}} \tag{3.73}$$

where M_k is the molecular weight of species k. The absorption coefficient κ_{outer} may be obtained by summing up contributions from each radiating species.

$$\hat{\kappa} = \hat{\kappa}_{CO_2} + \hat{\kappa}_{H_2O} + \hat{\kappa}_{soot} \tag{3.74}$$

where,

$$\kappa_{CO_2} + \kappa_{H_2O} = p\left(x_{CO_2} a_{CO_2} + x_{H_2O} a_{H_2O}\right)$$

and

$$\kappa_{soot} = C_{soot} f_v T$$

Again, the outer temperatures are used to compute these quantities, except for soot which is sensitive to the inner structure, for which one uses the solutions ob-

tained after solving for the quantities over the whole domain (details explained in Section 3.7).

3.5.6 Solving for the Outer Temperature Using Green's Functions

For the sake of convenience, the outer temperature is expressed in terms of the temperature drop from adiabatic or non-radiating conditions.

$$\hat{T}(\zeta) = \hat{T}^0(\zeta) - \Delta\hat{T}(\zeta) \tag{3.75}$$

where $\Delta\hat{T}$ is the correction to the outer temperature due to radiation. This is a quantity that we assume to be continuous and *smooth* upto its second derivative. This would be the case if we have *complete* consumption of fuel and oxidizer (it becomes apparent on manipulating the governing equations, as is explained in the appendices). As shall be seen, the burning rate scales as the inverse square root of the mixing rate, demonstrating that the assumption is correct. The outer energy equation now becomes

$$-\hat{L}(\Delta\hat{T}) = f(\zeta) \tag{3.76}$$

This is a non-linear equation in that the right-hand side depends on both the flame temperature. The treatment adopted is to linearize the right-hand side and solve the linearized equations with sequence of iterative sweeps. If $f(\zeta)$ *were* linear, we may solve this inhomogeneous equation using Green's functions as follows (the reader is referred to texts on ODEs for the pedagogical details [18]).

$$\Delta\hat{T}(\zeta) = \int_{-\infty}^{\infty} G(\zeta;t)f(t)\exp\left(\frac{t^2}{2}\right)\mathrm{d}t \tag{3.77}$$

where G is the Green's function for the ODE under consideration (Equation 3.76), which satisfies the boundary conditions of the original problem so that $\Delta\hat{T}^0(\zeta = \pm\infty) = 0$

$$
\begin{aligned}
G(\zeta, t) &= \frac{1}{2}\sqrt{\frac{\pi}{2}}\psi_1(t)\psi_2(\zeta); && t < \zeta \\
&= \frac{1}{2}\sqrt{\frac{\pi}{2}}\psi_2(t)\psi_1(\zeta); && t > \zeta
\end{aligned}
\tag{3.78}
$$

where

$$
\psi_1(\zeta) = \left[1 + \text{ erf}\left(\frac{\zeta}{\sqrt{2}}\right)\right]
\tag{3.79}
$$

and

$$
\psi_2(\zeta) = \left[\text{ erf}\left(\frac{\zeta}{\sqrt{2}}\right) - 1\right]
\tag{3.80}
$$

3.5.7 Correction for Nonlinearity Using Successive Approximations

Having obtained the solutions to the linearized energy equation, one may proceed to correct for non-linearlity using successive approximations, so that the solution obtained during a given iteration may be used in the source term to get the next iterate of the solution, the procedure being repeated until there is no variation in the solution obtained. This is done as follows. Let $\hat{T}^N$ be the Nth iterate of the solution to the outer energy equation, written in terms of iterates as

$$
-\hat{L}[\hat{T}^{N+1}(\zeta)] = f[\hat{T}^N(\zeta)]
\tag{3.81}
$$

where $\hat{T}$ is taken as the leading order solution for temperature, as implied in the foregoing sections. Given a known function $\hat{T}^N(\zeta)$, one can obtain $\hat{T}^{N+1}$ by using the Green's function approach indicated. One may continue this procedure until the

difference between two successive iterates is smaller than a desired tolerance.

$$\frac{|\hat{T}^N - \hat{T}^{N+1}|}{|\hat{T}^N|} < tolerance \tag{3.82}$$

3.5.8 Relating 'Howarth' Strain Rate With the Scalar Dissipation Rate

In the current work, the inner equations are solved in mixture fraction space. It is therefore of interest to relate the Howarth strain rate α with the scalar dissipation rate that appears in the inner equations. This is done as follows.

From the definition of the scalar dissipation rate at the flame in one dimensional coordinates χ_{st}, one has (with $x' = x/\ell$, the spatial coordinate, being non-dimensional)

$$\chi_{st} = \frac{2D_{st}}{\ell^2} \left(\frac{dZ}{dx'}\right)^2_{st} \tag{3.83}$$

Introducing the Howarth transformation implied in equation (3.2) one gets

$$\chi_{st} = \frac{2D_{st}}{\ell^2} \frac{\rho_{st}}{\rho_2} \left(\frac{dZ}{d\zeta}\right)^2_{st} \tag{3.84}$$

This may now be related to the Howarth strain rate α, recognizing that

$$\alpha = \frac{D_{st}}{\ell^2} \tag{3.85}$$

so that the scalar dissipation rate at the flame may be written as

$$\chi_{st} = 2\alpha \left(\frac{\rho_{st}}{\rho_2}\right)^2 \left(\frac{dZ}{d\zeta}\right)^2_{st} \tag{3.86}$$

The mixture fraction gradient is implied from the solution of the mixture fraction field Z, given by equation (3.36), reproduced below

$$Z = \frac{1}{2}\left[1 - \text{erf}\left(\frac{\zeta}{\sqrt{2}}\right)\right] \tag{3.87}$$

Upon using this in the equation for the scalar dissipation rate (3.86), together with $\rho_{st}^2 D_{st} = \rho_2^2 D_2$ one gets the relationship between the strain rate and scalar dissipation rate as

$$\alpha = \pi \chi_{st} \exp(\zeta_{st}^2) \tag{3.88}$$

3.6   Inner Equations

The inner equations at the reaction zone are solved in mixture fraction space. The notation for non-dimensional variables is such that one inserts a 'tilde' above each variable to represent its corresponding non-dimensional inner analogue.

$$T \to \tilde{T}; \qquad Y_F \to \tilde{Y}_F; \qquad Y_{O_2} \to \tilde{Y}_{O_2} \tag{3.89}$$

The governing equations for a one-dimensional, steady flamelet [73](under which assumptions the procedure is carried out) are as follows

$$\frac{\chi_{st}}{2} \frac{\mathrm{d}^2 Y_F}{\mathrm{d}Z^2} = \frac{\dot{\omega}_F}{\rho_{st}} \tag{3.90}$$

$$\frac{\chi_{st}}{2} \frac{\mathrm{d}^2 Y_{O_2}}{\mathrm{d}Z^2} = r_s \frac{\dot{\omega}_F}{\rho_{st}} \tag{3.91}$$

and

$$\frac{\chi_{st}}{2} \frac{\mathrm{d}^2 T}{\mathrm{d}Z^2} = -\frac{(\Delta H_F)}{c_p} \frac{\dot{\omega}_F}{\rho_{st}} + \frac{1}{\rho_{st} c_p} \nabla \cdot \vec{q}_R \tag{3.92}$$

The energy equation, after suitable non-dimensionalization, and neglecting the small radiation term (compared to reaction) may be written as

$$\frac{\mathrm{d}^2 \tilde{T}}{\mathrm{d}Z^2} = -Da_C \tilde{Y}_F^p \tilde{Y}_{O_2}^q \exp\left(-\frac{\tilde{T}_a}{\tilde{T}}\right) \tag{3.93}$$

where Da_C is a Damköhler number

$$Da_C = \frac{2r_s^q B \hat{\rho}_{st}^{p+q-1} Y_{F,1}^{p+q-1}}{\chi_{st} M_F^p M_{O_2}^q} \tag{3.94}$$

For future reference, the diffusion transport operator on the left hand side of these equations is denoted by $\tilde{L}$

$$\tilde{L} \equiv \frac{\mathrm{d}^2}{\mathrm{d}Z^2} \tag{3.95}$$

3.6.1 Inner Expansions

As is customary in Large Activation Energy Asymptotics (AEA) [53], [73], a small parameter for the reaction zone is defined as

$$\epsilon = \frac{\tilde{T}_{st}^2}{\tilde{T}_a} \tag{3.96}$$

A stretching transformation is introduced for the mixture fraction around $Z = Z_{st}$

$$Z = Z_{st} + \epsilon \tilde{Z} \tag{3.97}$$

and inner expansions are postulated for the flame temperature and mass concentrations

$$\tilde{Y}_F = \epsilon \mathscr{Y}_F + O(\epsilon^2)$$

$$\tilde{Y}_{O_2} = \epsilon \mathscr{Y}_{O_2} + O(\epsilon^2) \tag{3.98}$$

$$\tilde{T} = \hat{T}_{st} - \epsilon \mathscr{T} + O(\epsilon^2)$$

In the foregoing equations, fuel and oxidizer are assumed to vanish at the flame zone to leading order, and the leading order flame temperature is dictated by that given by the outer solutions, with which they are matched (containing radiation

63

effects). However, the reaction rate varies rapidly in the inner region, its variations are governed by the first order term owing to the large Damköhler number. From a dominant balance of the terms involved, one may write the inner energy equation as

$$\frac{\mathrm{d}^2 \mathscr{T}}{\mathrm{d}\tilde{Z}^2} = Da_C \epsilon^{p+q+1} \mathscr{Y}_F^p \mathscr{Y}_{O_2}^q \exp\left(-\frac{\tilde{T}_a}{\tilde{T}}\right) \tag{3.99}$$

In the foregoing equation, radiation is neglected in comparison with the reaction term. Length scale arguments may be invoked to compare the two terms; the length scale over which radiation effects become important are much larger than that of the reaction zone.

After expanding the temperature in the exponential term using equation (3.98), and grouping constants together one gets

$$\frac{\mathrm{d}^2 \mathscr{T}}{\mathrm{d}\tilde{Z}^2} = \delta \mathscr{Y}_F^p \mathscr{Y}_{O_2}^q \exp(-\mathscr{T}) \tag{3.100}$$

where δ is a reduced Damköhler number defined as

$$\delta = Da_C \epsilon^{p+q+1} \exp\left(-\frac{\tilde{T}_a}{\hat{T}_{st}}\right) \tag{3.101}$$

which works out as

$$\delta = \frac{2\hat{\rho}_{st}^{p+q-1} Y_{F,1}^{p+q-1} r_s^q A \exp(-T_a/\hat{T}_{st}) \epsilon^{p+q+1}}{(10^6)^{p+q-1} M_F^{p-1} M_{O_2}^q \chi_{st}} \tag{3.102}$$

Extinction conditions are interpreted from the foregoing equation as occuring when the ODE for the flame temperature implied ceases to have a solution. This shall be elaborated upon later. One wishes (in equation (3.100)) to express the mass fraction terms $\mathscr{Y}_F$ and $\mathscr{Y}_{O_2}$ in terms of the inner temperature quantity $\mathscr{T}$. This is

done by using Shvab-Zeldovich relationships and matching with the outer solutions.

Consider the coupling relationship around $Z = Z_{st}$

$$\tilde{L}(\tilde{T} + \tilde{Y}_F) = \frac{2}{\rho Y_{F,1} \chi \Delta H_F} \nabla \cdot \vec{q}_R \tag{3.103}$$

Upon decomposing into inner scales one gets

$$\frac{\mathrm{d}^2(\mathscr{Y}_F - \mathscr{T})}{\mathrm{d}\tilde{Z}^2} = \epsilon \frac{2}{\rho_{st} Y_{F,1} \chi_{st} \Delta H_F} \nabla \cdot \vec{q}_R \tag{3.104}$$

By dominant balance, the RHS may be neglected in comparison with LHS, so that one has to leading order

$$\frac{\mathrm{d}^2(\mathscr{Y}_F - \mathscr{T})}{\mathrm{d}\tilde{Z}^2} = 0 \tag{3.105}$$

which has the solution

$$\mathscr{Y}_{\mathscr{F}} - \mathscr{T} = C_1 \tilde{Z} + C_2 \tag{3.106}$$

Or in other words, around $Z = Z_{st}$ one has

$$\tilde{T} + \tilde{Y}_F = C_1 Z + C_3 \tag{3.107}$$

where

$$C_3 = \tilde{T}_{st} - C_1 Z_{st} + \epsilon C_2 \tag{3.108}$$

Differentiating on the air side, putting $Y_F(Z \to Z_{st,-}) = 0$, and matching with outer solutions

$$C_1 = \left(\frac{\mathrm{d}\tilde{T}}{\mathrm{d}Z}\right)_{Z=Z_{st,-}} = \left(\frac{\mathrm{d}\hat{T}}{\mathrm{d}Z}\right)_{Z=Z_{st,-}} \tag{3.109}$$

In order to obtain C_2 comparison is made with the Shvab-Zeldovich relationship that constitutes $\tilde{T} + \tilde{Y}_F$.

$$L'(T' + Y_F') = \frac{1}{\alpha \rho \Delta H_F} \nabla \cdot \vec{q}_R \tag{3.110}$$

The right hand side is a function of the temperature, and one would expect the solution at the flame to be embedded in an integral kernel with the corresponding Green's function. Note is made of the fact that the integral kernel will be a function (in order of magnitude terms) of an average absorption coefficient.

$$\frac{1}{\alpha\rho}\nabla\cdot\vec{q}_R \sim \frac{\sigma T_f^4}{\alpha\rho_f\Delta H_F}\bar{\kappa}[1+O(\epsilon)] \tag{3.111}$$

where $\bar{\kappa}$ is some average absorption coefficient for the system. In the absence of radiation, this quantity is zero (putting $\bar{\kappa}=0$), which gives $C_2 = 0$ when a term by term comparison in equation (3.108) is carried out, yielding the so-called Burke-Schumann solution. However, when κ is non-zero, the $O(1)$ term gives a measure of the temperature drop arising from radiation (which is what is computed in the outer solutions). In this case, one expects a contribution from the $O(\epsilon)$ term when there is radiation, which would increase in significance as $\bar{\kappa}\ell$ (in rough terms, ℓ contains the effect of strain) increases. In the current analysis, it is neglected for simplicity (as would indeed be the case, when $\bar{\kappa}\ell$ is small). Hence, the analysis is to some extent valid mostly for *small* $\bar{\kappa}\ell$. We carry out the analysis with this assumption, and compare them with the DNS solutions obtained for validation. A successful validation would imply that it is reasonable to neglect the higher order terms.

This also brings to focus an interesting question regarding the formulation of the inner approximations in optically thicker media, where the laminar flamelet equations would have to be revisited in strongly radiating flames, since the inner equations will take a different form from what is usually presented [89, 111, 57] (note is made of the fact that these references consider only optically thin conditions, and

that this issue has not hitherto been raised, to the best of the author's recollection, anywhere else). By logical extension of the above arguments, it becomes apparent that extinction conditions will hardly have the same morphological features as the 'classical' extinction conditions, because these arise from an entirely different type of inner equation, and therefore, one which will have a different solution for the Damköhler number. However, whether or not such conditions arise in practice is moot, aside from providing a rather interesting theoretical minutia to cogitate over.

To return to the main point of the discussion, putting $C_2 = 0$ one gets

$$\mathscr{Y}_F = \mathscr{T} - \left(\frac{\mathrm{d}\hat{T}}{\mathrm{d}Z}\right)_{Z=Z_{st,-}} \tilde{Z} \tag{3.112}$$

Similarly, for the oxygen mass fraction one obtains

$$\mathscr{Y}_{O_2} = \mathscr{T} - \left(\frac{\mathrm{d}\hat{T}}{\mathrm{d}Z}\right)_{Z=Z_{st,+}} \tilde{Z} \tag{3.113}$$

Thus, the inner energy equation may be written as

$$\frac{\mathrm{d}^2\mathscr{T}}{\mathrm{d}\tilde{Z}^2} = \delta \left[\mathscr{T} - \left(\frac{\mathrm{d}\mathscr{T}}{\mathrm{d}\tilde{Z}}\right)_{Z_{st,-}} \tilde{Z}\right]^p \left[\mathscr{T} - \left(\frac{\mathrm{d}\mathscr{T}}{\mathrm{d}\tilde{Z}}\right)_{Z_{st,+}} \tilde{Z}\right]^q \exp(-\mathscr{T}) \tag{3.114}$$

3.6.1.1   Transformation into Liñan's Form

It is convenient to transform the inner equations into the form given in Liñan [53], which may be achieved as follows.

Define

$$\theta = \mathscr{T} - \left[\left(\frac{\mathrm{d}\hat{T}}{\mathrm{d}Z}\right)_{Z_{st,+}} + \left(\frac{\mathrm{d}\hat{T}}{\mathrm{d}Z}\right)_{Z_{st,-}}\right] \frac{\tilde{Z}}{2}$$

$$\eta = \left[\left(\frac{\mathrm{d}\hat{T}}{\mathrm{d}Z}\right)_{Z_{st,+}} - \left(\frac{\mathrm{d}\hat{T}}{\mathrm{d}Z}\right)_{Z_{st,-}}\right] \frac{\tilde{Z}}{2} \tag{3.115}$$

and

$$\gamma = \frac{\left(\frac{\mathrm{d}\hat{T}}{\mathrm{d}Z}\right)_{Z_{st,+}} + \left(\frac{\mathrm{d}\hat{T}}{\mathrm{d}Z}\right)_{Z_{st,-}}}{\left(\frac{\mathrm{d}\hat{T}}{\mathrm{d}Z}\right)_{Z_{st,+}} - \left(\frac{\mathrm{d}\hat{T}}{\mathrm{d}Z}\right)_{Z_{st,-}}} \tag{3.116}$$

to get

$$\frac{\mathrm{d}^2\theta}{\mathrm{d}\eta^2} = \delta_*(\theta + \eta)^p(\theta - \eta)^q \exp[-(\theta + \gamma\eta)] \tag{3.117}$$

where δ_* is a reduced Damköhler number defined as

$$\delta_* = \frac{4\delta}{\left[\left(\frac{\mathrm{d}\hat{T}}{\mathrm{d}Z}\right)_{Z_{st,+}} - \left(\frac{\mathrm{d}\hat{T}}{\mathrm{d}Z}\right)_{Z_{st,-}}\right]^2} \tag{3.118}$$

The boundary conditions for this problem are

$$\left(\frac{\mathrm{d}\theta}{\mathrm{d}\eta}\right)_{\eta\to-\infty} = -1; \qquad \left(\frac{\mathrm{d}\theta}{\mathrm{d}\eta}\right)_{\eta\to\infty} = 1 \tag{3.119}$$

3.6.2 Extinction Conditions

Extinction is interpreted as occurring when equation (3.117) ceases to have a solution for a given value of δ_*. This happens when δ_* becomes small. From the test cases carried out here, it is seen that this happens when $\delta_* \approx 1$. To understand this better, inspection is made of the reduced Damköhler number δ_*

$$\delta_* = \frac{4\delta}{\left[\left(\frac{\mathrm{d}\mathscr{T}}{\mathrm{d}\bar{Z}}\right)_{Z_{st,+}} - \left(\frac{\mathrm{d}\mathscr{T}}{\mathrm{d}\bar{Z}}\right)_{Z_{st,-}}\right]^2}$$

In the foregoing, the denominator is the jump condition in the outer temperature gradient, which is a constant. This is because the temperature drop from radiation is assumed to be a smooth function in temperature, and gets canceled out, yielding the same jump condition as in the adiabatic case. It is esentially a measure of the strength of the chemical reaction, as shall be shown subsequently. One can therefore

say that $\delta_* \sim \delta$. Investigation of the functional form of δ provides some insight into the phenomenology of extinction.

$$\delta \sim Da_C \epsilon^{p+q+1} \exp\left(-\frac{\tilde{T}_a}{\hat{T}_{st}}\right) \sim \frac{1}{\chi_{st}} \epsilon^{p+q+1} \exp\left(-\frac{\tilde{T}_a}{\hat{T}_{st}}\right) \tag{3.120}$$

Extinction conditions occur when $\delta_* < \delta_{*,C}$ where $\delta_{*,C} \approx 1$. This would happen when

- the scalar dissipation rate (that appears in the denominator in Equation (3.120)) becomes large-as would be expected when the flame is strongly stretched.

- the flame temperature (that appears in the exponential term of Equation (3.120)) becomes small-as would happen in strongly radiating flames.

It is noted that radiating conditions only affect the value of γ, which depends on the temperature jump conditions at the flame. That $\delta_* \approx 1$ for extinction supports the idea that one could write an extinction model to back-calculate the extinction flame temperature for a given stretch rate.

3.6.3 Strength of the Reaction Source term

The reaction source term at the flame may be obtained from the outer solutions, which are sufficient to determine the burning rate as follows. Consider the inner equation in mixture fraction coordinates.

$$\frac{d^2 Y_F}{dZ^2} = \frac{2}{\rho_{st}\chi_{st}}\dot{\omega}_F \tag{3.121}$$

This equation may be integrated to give the burning rate.

$$\left[\left(\frac{dY_F}{dZ}\right)_{Z_{st,+}} - \left(\frac{dY_F}{dZ}\right)_{Z_{st,-}}\right] = \frac{2}{\rho_{st}\chi_{st}} \int_{Z_{st,-}}^{Z_{st,+}} \dot{\omega}_F dZ \tag{3.122}$$

which yields

$$\left[\left(\frac{\mathrm{d}Y_F}{\mathrm{d}Z}\right)_{Z_{st,+}} - \left(\frac{\mathrm{d}Y_F}{\mathrm{d}Z}\right)_{Z_{st,-}}\right] = \frac{2}{\rho_{st}\chi_{st}}\left(\frac{\mathrm{d}Z}{\mathrm{d}x}\right)_{st}\int_{x_{st,-}}^{x_{st,+}}\dot{\omega}_F\mathrm{d}x \qquad (3.123)$$

Rewriting, and recognizing that

$$\chi_{st} = 2D_{st}\left(\frac{\mathrm{d}Z}{\mathrm{d}x}\right)_{st}^2 \qquad (3.124)$$

together with $\rho_{st}^2 D_{st} = \rho_2^2 D_2$ one gets

$$\int_{x_{st,-}}^{x_{st,+}}\dot{\omega}_F\mathrm{d}x = \left[\frac{\mathrm{d}Y_F}{\mathrm{d}Z}\right]_{st}\rho_2\sqrt{\frac{D_2}{2}}\sqrt{\chi_{st}} \qquad (3.125)$$

where

$$\left[\frac{\mathrm{d}Y_F}{\mathrm{d}Z}\right]_{Z_{st,-}}^{Z_{st,+}} = \left[\left(\frac{\mathrm{d}Y_F}{\mathrm{d}Z}\right)_{Z_{st,+}} - \left(\frac{\mathrm{d}Y_F}{\mathrm{d}Z}\right)_{Z_{st,-}}\right] \qquad (3.126)$$

is the fuel mass jump condition. This may be used to shed insight into fuel and oxidizer vitiation by noting its dependence on the boundary conditions $Y_{F,1}$ and $Y_{O_2,2}$.

Invoking the solution for the Burke-Schumann flame, we get

$$\begin{aligned} Y_F &= 0; & Z < Z_{st} \\ &= Y_{F,1}\frac{Z - Z_{st}}{1 - Z_{st}}; & Z \geq Z_{st} \end{aligned} \qquad (3.127)$$

or

$$\left[\frac{\mathrm{d}Y_F}{\mathrm{d}Z}\right]_{st} = \frac{Y_{F,1}}{1 - Z_{st}} = Y_{F,1} + Y_{O_2,2}/r_s \qquad (3.128)$$

which gives

$$\int_{x_{st,-}}^{x_{st,+}}\dot{\omega}_F\mathrm{d}x = \sqrt{\frac{D_2}{2}}\rho_2\left(Y_{F,1} + Y_{O_2,2}/r_s\right)\sqrt{\chi_{st}} \qquad (3.129)$$

The above expression should hold (in the fast chemistry regime) for a general turbulent flame, requiring information on the local flow conditions, embedded in the

70

scalar dissipation rate χ_{st}; and the ambient mixing conditions, which we would expect to be affected by vitiation of fuel and oxidizer, and which are embodied in the quantity containing the fuel and oxidizer ambient mass fractions. This expression will be subjected to a verification test using data obtained from DNS.

3.7   Flame Structure Using Soot

In this section, the soot modeling approach used in the AEA analysis is described. Soot formation is described using a phenomenological modeling strategy previously developed by Moss *et al.* [69, 14] and Lindstedt *et al.* [52, 29]. The strategy consists in solving two transport equations for soot mass fraction Y_{soot} and soot number density N_{soot}:

$$(\bar{u} + \bar{V}_t)\frac{\mathrm{d}Q}{\mathrm{d}\xi} + \frac{\mathrm{d}\bar{V}_t}{\mathrm{d}\xi} = \frac{\dot{\omega}_Q}{\rho} \tag{3.130}$$

where Q is Y_{soot} or $n_{soot}/(\rho/N_A)$ with N_A the Avogadro number, $N_A = 6.022 \times 10^{26}$ particles/mol, and where $\bar{V}_t$ is the density weighted thermophoretic velocity in the flame normal direction

$$V_t = -0.54\nu_2\frac{\partial}{\partial\xi}(\ln T) \tag{3.131}$$

with ν_2 the kinematic viscosity in the oxidizer stream. The source term on the RHS of equation (3.130) incorporates semi-empirical descriptions of important physical and chemical soot processes, e.g. particle inception, surface growth, oxidation, and coagulation [14, 52, 29]. These expressions are also based on a number of simplifying assumptions, for instance the model ignores the role of soot precursors and assumes

a mono-dispersed soot particle size distribution. In addition, because it is combined with single-step combustion chemistry, the model adopts ethylene as the controlling species for soot inception and O_2 as that for soot oxidation. Model coefficients are taken from [14]. The values of the fuel and oxygen mole fractions and of temperature required in equation (3.130) are obtained from a reconstructed flame solution that combines the inner and outer solutions discussed in 3.6: the inner solution is used for $Z_{st} - 0.01 \leq Z \leq Z_{st} + 0.02$; the outer solution is used outside that range. Equation (3.130) is solved using a second order finite difference method and is coupled to the outer and inner equations via an interative algorithm.

Soot mass is added to the flow on the air side of the flame. While adding soot on the fuel side may appear as a better representation of the multi-dimensional sooting flame configurations that motivate the present study, it is important to realize that since the counterflow flame is located on the air side of the stagnation plane,soot particles added to the fuel will essentially follow flow streamlines and will never reach the flame because of the adverse effects of convection and thermophoresis; thus, to evaluate their impact on flame structure, soot particles must be added at locations where they can be convected into the reaction zone. This observation illustrates some of the challenges found in using counterflow flame configurations as a representative model for sooting flames.

3.8 Summary

The focus of the current chapter has been to unravel the mathematical structure of kinetic and radiative extinction by an analysis of the governing equations. Using matched asymptotic expansions comprising the AEA approach, extinction criteria have been derived to dercribe the two limits, and the controlling parameters endemic to radiating flames, inasmuch as to illuminate how the effects of strain and radiative heat loss may be juxtaposed to cause weakening, and extinction as seen from the context of laminar counterflow diffusion flames. While peripheral to the above-mentioned cause, it is nonetheless highly interesting to note that the solution of the RTE to derive the absorption source term could be use in describing optically thick conditions characterized by non-locally originating soot. In subsequent chapters are described the application of the extinction criteria derived, in more complex configurations consisting of external soot addition and turbulent coflow flames.

Chapter 4

Laminar Counterflow Flame Extinction Predictions

In this chapter, results are presented from a laminar counterflow flame study to understand how diffusion flames interact with soot and radiation computed with S3D. The case presented does not have any external soot loading (no soot injection). The soot produced originates locally from the flame. In subsequent chapters, laminar and turbulent flames are presented where external soot is loaded. The purpose of the present chapter is to demonstrate the existence of the two quenching limits (the strain affected high stretch limit and the radiation affected low stretch limit), computed using DNS. A comparison with the AEA results is also made for the equivalent counterflow configuration using the approach detailed in Chapter 3. It needs to be mentioned that soot equations are also to be solved, the details of which are given in Section 3.7 in the chapter following the present. Also, the AEA case involves the assumption of $\rho^2 D = constant$, which is not done in the DNS (which uses $\rho^{1.7} D = constant$.

This study considers the generic case of steady, plane, counterflow, ethylene-air flames (without gravity) (with single-step chemistry, radiation and soot models as introduced in Chapter 2); several flame structures are calculated ranging from high to low stretch conditions. The computational domain is two-dimensional (Figure 4.1); its size varies from $(L_x, L_y) = (1, 1.2)$ under high stretch conditions up to

$(L_x, L_y) = (160, 380)$ under low stretch conditions, where L_x and L_y are the x and y-sizes of the domain (in units of cm) and x is the flame normal direction. The grid spacing is stretched in the x-direction with $\Delta x \approx 60$ mm in the reaction zone; it is uniform in the y-direction and varies from $\Delta y \approx 120$ mm (high stretch limit) to 1.9 cm (low stretch limit). For each simulated flame, calculations are performed using a time marching approach until steady state is achieved.

Figure 4.2 summarizes important results from the laminar flamelet database and presents in particular the variations of the centerline combustion and radiation intensities with fuel-air mixing rate; the combustion (radiation) intensity is measured as the heat release rate (net radiative power) per unit flame surface area, $\dot{q}_c'' = \int \dot{q}_c''' dx$ ($\dot{q}_r'' = \int \dot{q}_r''' dx$); the fuel-air mixing rate is measured as the stoichiometric value χ_{st} of the scalar dissipation rate. The inverse of χ_{st} provides an estimate of the mixing time in the vicinity of the reaction zone. Figure 4.2 shows that the flammable domain of strained diffusion flames is limited by upper and lower limits at large and low values of χ_{st} . The upper limit corresponds to the classical flame response to increasing mixing rates, i.e. to an intensification of combustion at moderate to high values of χ_{st}, followed by kinetic extinction once $\chi_{st} \geq \chi_{st}^{UL}$ with $\chi_{st}^{UL} \approx 50$ s^{-1}. This upper limit is the only extinction limit observed under adiabatic combustion conditions. The lower limit corresponds to the flame response to decreasing mixing rates, i.e. to a progressive weakening of combustion at moderate to low values of χ_{st}, followed by radiative extinction once $\chi_{st} \leq \chi_{st}^{LL}$ with $\chi_{st}^{LL} \approx 0.025$ s^{-1}.

Figure 4.3 plots the flame temperature (at the stoichiometric location) over the flammable range from the high stretch limit to the low stretch limit. The equivalent

case obtained from AEA is also plotted (for details, chapter 5 may be referred to) with $\rho^2 D = constant$. The comparison between the two methods is excellent, providing good cross-validation between the two cases. The flame temperature varies from ≈ 1935 K to ≈ 1250 K at the low stretch limit. The radiative extinction limit temperature may be compared with [84] where the temperature obtained was about 1100 K. Further validation studies between AEA and DNS are included in the appendices. Figure 4.4 presents the variations of the flame radiant fraction (in which the radiation cooling rate and combustion intensity are both integrated across the flame sheet) with the mixing rate. It is seen thhat the effect of radiation increases fairly monotonically as one decreases the stretch rate, varying from nearly zero at the high stretch limit to nearly 60 % at the low stretch limit Figure 4.5 presents the variation of the peak soot mass fraction in the computational domain (which occurs somewhere in the vicinity of the flame) with the mixing rate. It is seen that there is hardly any soot at the quenching limits (at the high stretch limit, the residence time is too low for soot to form, while at the low stretch limit, the temperature is too low). The maximum soot (of about 2.5 % in mass fraction) occurs at intermediate stretch rates.

4.1 Conclusions

In the current chapter, DNS results were used to illustrate the behavior of laminar counterflow diffusion flames over a range of stretch rates, from stretch dominated high stretch limit (where radiation effects are negligible) to the radiation
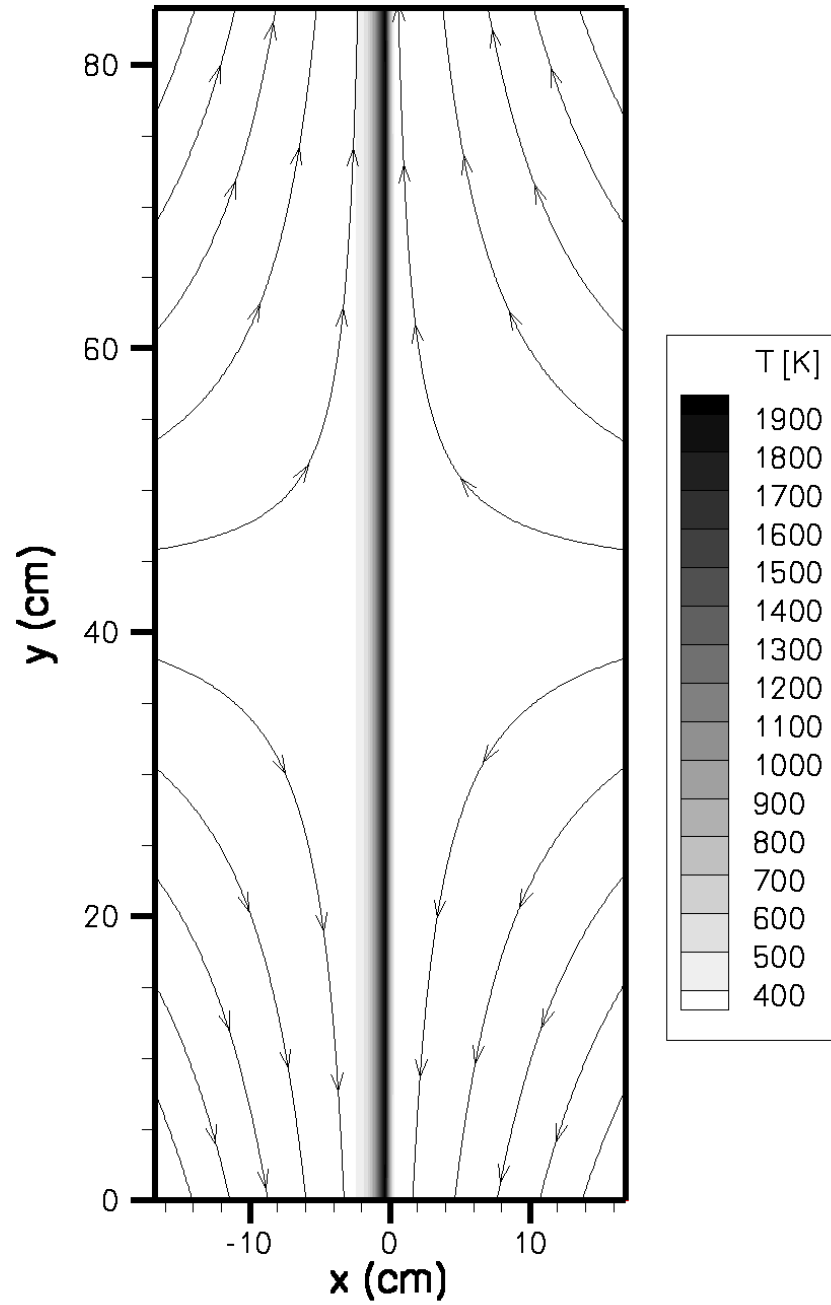
Figure 4.1: Laminar flamelet database. Fuel (ethylene) and oxidizer (atmospheric-air) are injected from the left and right respectively. The plot shows selected flow streamlines and temperature isocontours. In this case, $\chi_{st} = 0.2$ s^{-1} and $(L_x, L_y) = (33.6$ cm$, 84$ cm$)$.
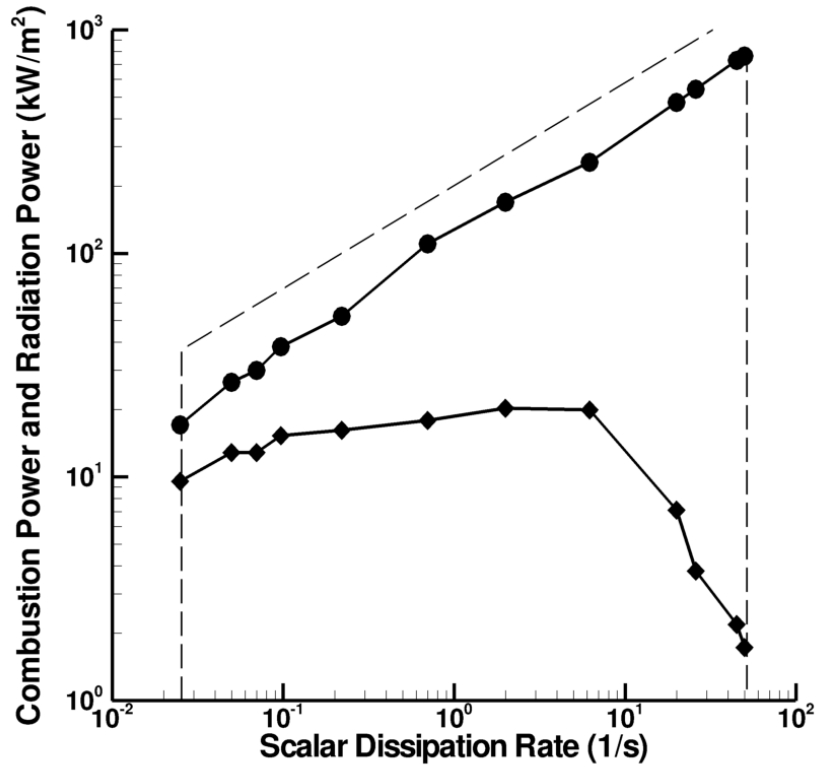
Figure 4.2: Laminar flamelet database (4). Combustion heat release rate $\dot{q}_c''$ (circles) and flame radiative power $\dot{q}_r''$ (diamonds) versus fuelair mixing rate χ_{st}. The top dashed line shows a reference square root variation; vertical dashed lines mark the lower and upper limits of the flammable domain, χ_{st}^{LL} and χ_{st}^{UL}.
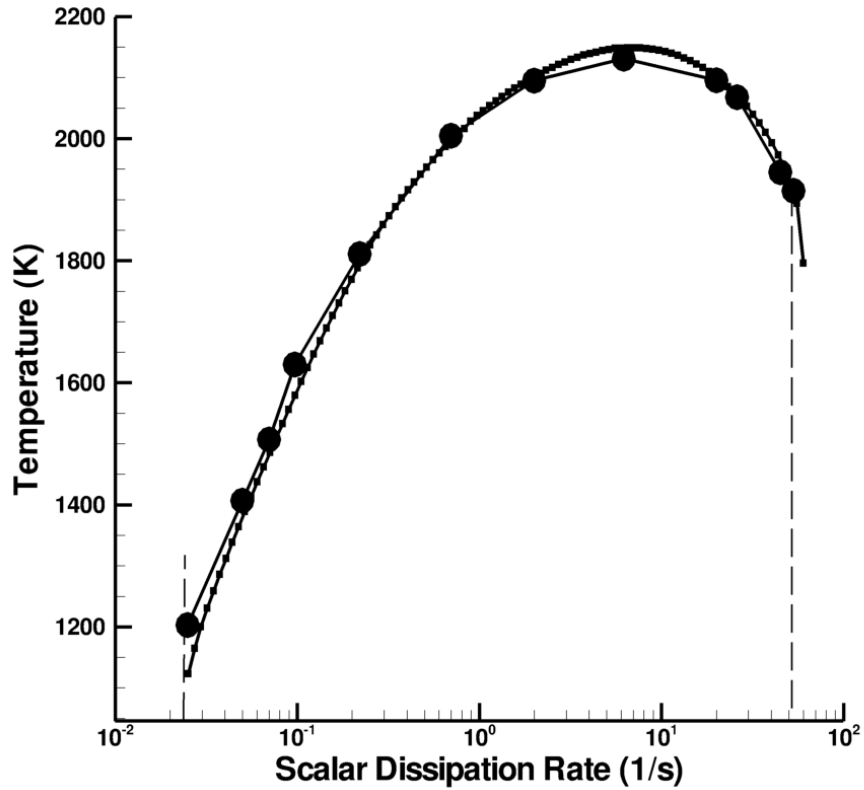
Figure 4.3: Laminar flamelet database (4, and equivalent AEA flame 3). Flame temperature [K] versus fuel-air mixing rate χ_{st}. Circular symbols represent DNS data, while diamond shaped symbols represent the AEA data. Vertical dashed lines mark the lower and upper limits of the flammable domain, χ_{st}^{LL} and χ_{st}^{UL}.
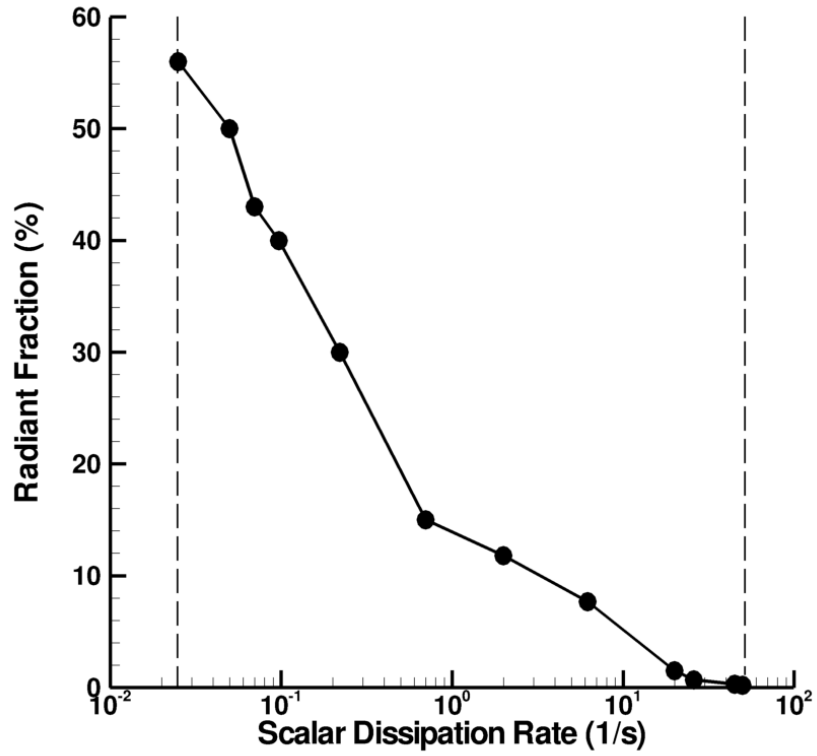
Figure 4.4: Laminar flamelet database (4). Radiant fraction (ratio of radiation cooling rate to flame heat release rate, with both quantities integrated across flame zone) versus fuel-air mixing rate. Vertical dashed lines mark the lower and upper limits of the flammable domain, χ_{st}^{LL} and χ_{st}^{UL}.
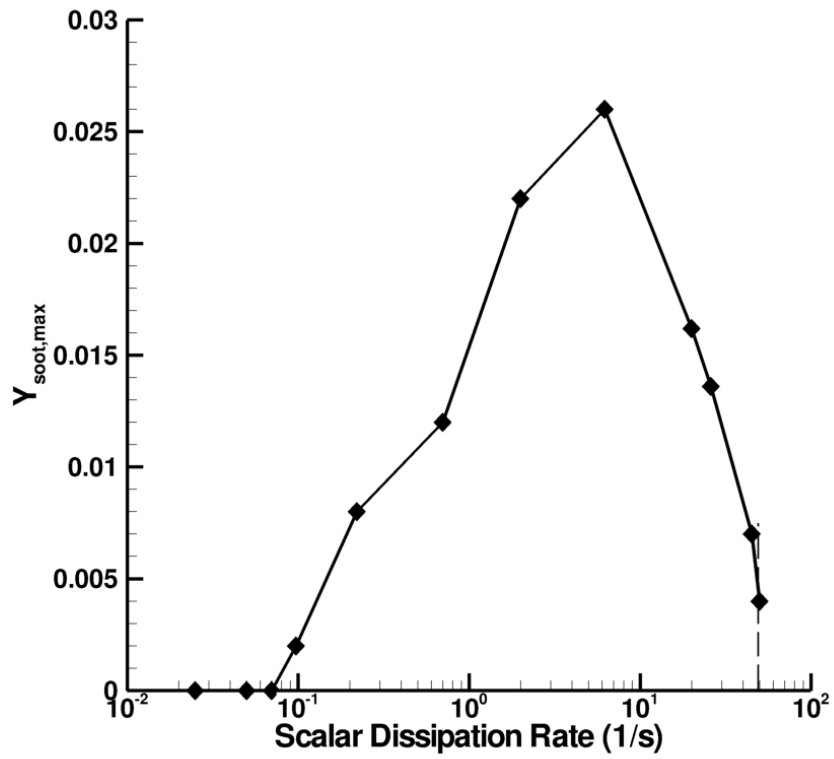
Figure 4.5: Laminar flamelet database (4). Peak soot mass fractions versus fuel-air mixing rate, corresponding to the maximum soot mass fraction in the domain. Vertical dashed lines mark the lower and upper limits of the flammable domain, χ_{st}^{LL} and χ_{st}^{UL}.

dominated low stretch limit. It is seen that the heat release rate varies as the square root of the stretch. Peak soot production takes place at moderate stretch rates, being negligible at the high and low stretch limits because of small residence time and low temperature respectively.

Chapter 5

Asymptotic Analysis of Radiative Extinction: Effect of Soot

Addition on Extinction Limits of Luminous Laminar Counterflow

Diffusion Flames

5.1   Introduction

The objective of the present chapter is to use large activation energy asymptotic (AEA) theory (developed in Chapter 3) to bring basic information on the extinction limits of non-premixed flames under sooting and radiating conditions, identical to the numerical configuration presented in previous chapters (Configuration C1). The AEA analysis assumes single-step global combustion chemistry, constant heat capacity and unity Lewis numbers; it also includes a two-equation phenomenological model to describe soot formation, growth and oxidation processes, as well as a generalized treatment of thermal radiation that assumes spectrally-averaged gray-medium properties and applies to flames with an arbitrary optical thickness. The focus of the present study is on the effect of external soot loading on flame extinction, and in particular on the slow-mixing/radiative-extinction limit that is believed to be the dominant mechanism that determines flame extinction in fires. External soot loading simulates non-local effects observed in multi-dimensional sooting flames in which soot mass may be produced at some flame locations and transported to

others where it will increase the flame luminosity and drive combustion conditions towards extinction. The AEA analysis shows that external soot loading results in a significant decrease of the size of the flammable domain and that the minimum value of flame stretch at the radiative extinction limit is increased by more than one order of magnitude compared to a non-soot-loaded-flame case. Multi-dimensional sooting flames are therefore expected to be significantly more susceptible to radiative extinction than the one-dimensional configurations that have been previously studied in microgravity combustion research.

Laminar diffusion flames may be extinguished by a number of different mechanisms. For instance, diffusion flames may be extinguished by aerodynamic quenching, a mechanism in which the flame is weakened by fast flow-induced perturbations and a critical decrease in the flame residence time. Diffusion flames may also be extinguished by thermal quenching, a mechanism in which the flame is weakened by heat losses (e.g., convective cooling to cold wall surfaces, radiative cooling, or water evaporative cooling in fire suppression applications, etc) or by dilution quenching, a mechanism in which the flame is weakened due to changes in the fuel or oxidizer stream composition (e.g., air vitiation in under-ventilated fires); in both thermal and dilution quenching, extinction occurs because of a critical increase in the flame chemical time. Laminar flame theory suggests that all these different phenomena may be explained by a single flame extinction criterion known as a Damköhler number criterion [53, 113, 75]: the Damköhler number Da is defined as the ratio of a characteristic fuel-air mixing time divided by a characteristic chemical time and extinction is predicted to occur for values of Da that are critically low. The exis-

tence of several flame extinction mechanisms explains the different extinction limits that are often observed in non-premixed combustion systems. For instance, in the classical gaseous-fuel laminar counterflow diffusion flame configuration, the domain of flammability is limited by two fundamental limits: a fast mixing limit and a slow mixing limit [28, 20, 63, 7, 57, 111, 71]. In the fast mixing limit, Da is small because the mixing time is short. The fast-mixing/aerodynamic-quenching limit is the classical limit observed in the high Reynolds number turbulent flames that are typical of many combustion engine applications. In contrast, in the slow mixing limit, Da is small because the heat release rate is moderate and thermal radiation effects are significant, the flame temperature is consequently low and the chemical time is long. The slow-mixing/radiative-extinction limit is believed to be the dominant mechanism for extinction in the low-to-moderate Reynolds number turbulent flames that are typical of fire applications.

Radiative extinction has been studied in great detail over the past two decades in several laminar diffusion flame configurations, including solid fuel stagnation-point flames [82], spherical flames around liquid fuel droplets , and spherical or planar gaseous fuel flames [28, 20, 63, 7, 57, 111, 71] (see [13] for a review). Note that these previous studies correspond to microgravity conditions and to one-dimensional flame configurations; they are also characterized by extremely low values of the fuel-air mixing rates (i.e. low values of flame stretch). In microgravity configurations, radiative extinction is achieved by gradually decreasing the flame stretch and thereby promoting sluggish combustion conditions that are vulnerable to radiative cooling. The values of flame stretch at the radiative extinction limit are significantly lower

than those found in earth-gravity laminar flames in which buoyancy-driven mixing will maintain a minimum value of the fuel-air mixing intensity; therefore, the implications of the results obtained in microgravity configurations to earth-gravity-flames in general, and to turbulent combustion applications in particular remain entirely open questions.

Note also, that in one-dimensional flame configurations, due to the very low flame temperatures observed at the radiative extinction limit (as low as 1100-1300 K), laminar flames become blue-colored and soot-free prior to extinction and that extinction is controlled by radiant emissions from gaseous species (primarily CO_2 and H_2O. The implications of these results to fire applications that emphasize the dominant role of soot and luminous radiation remain also unclear. The generic configuration used in the fire science literature to understand flame extinction is a laminar co-flow jet diffusion flame configuration at smoke point conditions [61, 62, 72]. In a laminar jet diffusion flame configuration (and assuming a sooty fuel), flame extinction is observed by gradually increasing the fuel flow rate and thereby lengthening the flame and promoting formation and growth of soot particles upstream of the flame surface. The smoke point corresponds to the transition from sooting flame conditions in which soot particles are completely oxidized in the vicinity of the flame surface to smoking flame conditions in which a fraction of the soot mass leaks across the reaction zone and is emitted downstream of the flame without oxidation. This transition may be interpreted as a radiative extinction event [40] (although this is moot, and warrants investigation) but note that unlike the extinction results obtained in microgravity configurations, soot is the dominant factor that controls the

smoke point. One important feature of smoke point configurations is that the flame is two-dimensional; multi-dimensional effects are likely to play a major role in the flame dynamics: for instance, the soot produced at low-elevation high-temperature flame locations is transported into the higher-elevation lower-temperature flame tip region where it contributes to weaken the combustion. This non-local soot loading effect is not present in classical one-dimensional configurations, which suggests that these configurations are not representative of multi-dimensional (laminar or turbulent) sooting flame conditions.The objective of the present study is to evaluate the effect of non-local soot loading on the extinction limits of diffusion flames. The configuration corresponds to steady, one-dimensional, planar, laminar, counterflow, diffusion flames; the fuel is ethylene and the oxidizer is air; soot loading is simulated by adding a controlled amount of soot mass to the flow upstream of the flame. We use an extended large Activation Energy Asymptotic (AEA) analysis to calculate the extinction limits; the AEA analysis is extended to include finite rate soot chemistry and a generalized treatment of thermal radiation that applies to participating media ranging from optically-thin too optically-thick, discussed in Chapter 3.

5.2   Results

The flame structure was calculated using the AEA formulation presented in 3.4 and for different strain rate conditions (the counterflow flame is depicted in Figure 4.1, loaded with soot on the air side) while systematically changing these conditions until the extinction limits were reached (the limits are simply identified

by the absence of numerical convergence). The calculations were also performed for different soot mass loading levels; the soot loading level is characterized by the value of the soot mass fraction upstream of the flame, noted $Y_{soot,R}$; the corresponding soot number density is not important and is arbitrarily chosen as a very small number. The selected values for $Y_{soot,R}$ are up to 5%, ; these values are believed to be on the high end of non-local soot loading effects in multi-dimensional flames: for instance, the case leads to values of the soot mass fraction in the flame region that are comparable to values previously observed in direct numerical simulations of turbulent flames [71].

Figure (5.1) presents the variations of peak flame temperature with strain rate α for three different soot loading levels. Similar variations for the corresponding adiabatic flame case are also included for comparison. The figure shows that the flammable domain of laminar counterflow diffusion flames is limited by upper and lower limits at large and low values of α. As discussed in Chapter 1, the upper limit corresponds to the classical flame response to increasing mixing rates, i.e., to an intensification of combustion at moderate-to-high values of α (or equivalently χ_{st}), followed by aerodynamic quenching once $\alpha \geq \alpha^{UL}$ (or $\chi_{st} \geq \chi_{st}^{UL}$). This upper limit is the only extinction limit observed under adiabatic combustion conditions. The lower limit corresponds to the flame response to decreasing mixing rates, i.e. to a progressive weakening of combustion at moderate-to-low values of α, followed by radiative extinction once $\alpha \leq \alpha^{LL}$ ($\chi_{st} \leq \chi_{st}^{LL}$). In the absence of soot loading ($Y_{soot,R} = 0$), we find: $\alpha^{LL} \approx 0.8$ s^{-1} ($\chi_{st}^{UL} \approx 0.25$ s^{-1}) and $\alpha^{UL} \approx 1955$ s^{-1} ($\chi_{st}^{UL} \approx 61$ s^{-1}). In the case with $Y_{soot,R} = 0.05$, we find: $\alpha^{LL} \approx 13$ s^{-1} ($\chi_{st}^{LL} \approx 0.4$ s^{-1}) and
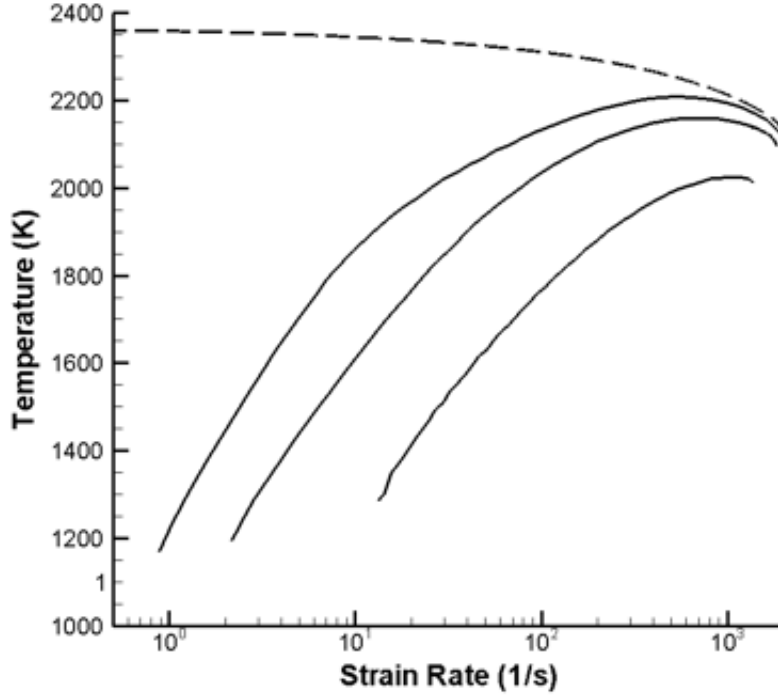
Figure 5.1: Peak flame temperature versus strain rate α (log-linear plot). Top dashed line: adiabatic flame. Three lower solid lines: sooting and radiating flames with $Y_{soot,R} = 0$ (top), 1% (middle), 5% (bottom). The end points of each solid line mark the lower and upper limits of the flammable domain.

$\alpha^{UL} \approx 1360 \text{ s}^{-1}$ ($\chi_{st}^{UL} \approx 42 \text{ s}^{-1}$). Thus, it is found that soot mass loading results in a significant decrease of the size of the flammable domain, and that for the range of conditions considered in the present study, the maximum value of flame stretch at the kinetic extinction may be decreased by as much as 30% while the minimum value of flame stretch at the radiative extinction limit may be increased by more than an order of magnitude.

These modifications of the flammable domain in the presence of soot load-

ing are further illustrated in Figure 5.2. Figure 5.2 presents the variations of the Damköhler number shows that consistent with classical laminar flame theory, flame extinction occurs when δ_* takes critically low values. An important result in Figure 5.2 is that the critical values of δ_* at the lower limit are approximately equal to those at the upper limit: in the case with $Y_{soot,R} = 0$, $\delta_*^{LL} \approx 1.1$ and $\delta_*^{UL} \approx 1.2$, whereas in the case with $Y_{soot,R} = 0.05$, $\delta_*^{LL} \approx 0.9$ and $\delta_*^{UL} \approx 1.2$, with δ_*^{LL} (δ_*^{UL}) the value of δ_* at the lower (upper) extinction limit. This result lends support to the unifying concept of a flame Damköhler number as the basis to predict all flame extinction limits: an approximate but reasonably accurate expression of the extinction criterion is $\delta_* \leq 1$.

Figure 5.3 presents the variations of soot volume fraction $f_{v,st}$ with strain rate α; $f_{v,st}$ is the soot volume fraction measured at the stoichiometric location where $Z = Z_{st}$. In the absence of soot loading, significant amounts of soot may be produced on the fuel side of the flame but this soot mass does not accumulate in the high temperature region of the flame because of adverse effects of both oxidation chemistry and convective and thermophoretic transport: $f_{v,st}$ remains below 0.01 ppm. In contrast, in the presence of soot loading, there are significant amounts of soot mass present in the high temperature region of the flame: $f_{v,st}$ is on the order of 1 ppm in the case with $Y_{soot,R} = 0.01$, and on the order of 5 ppm in the case with $Y_{soot,R} = 0.05$. This high-temperature soot is responsible for the increase in the flame luminosity and for the associated changes in the flame dynamics described in Figures 5.1, 5.2.

Figures 5.4, 5.5, 5.6 present two representative flame structures, as obtained
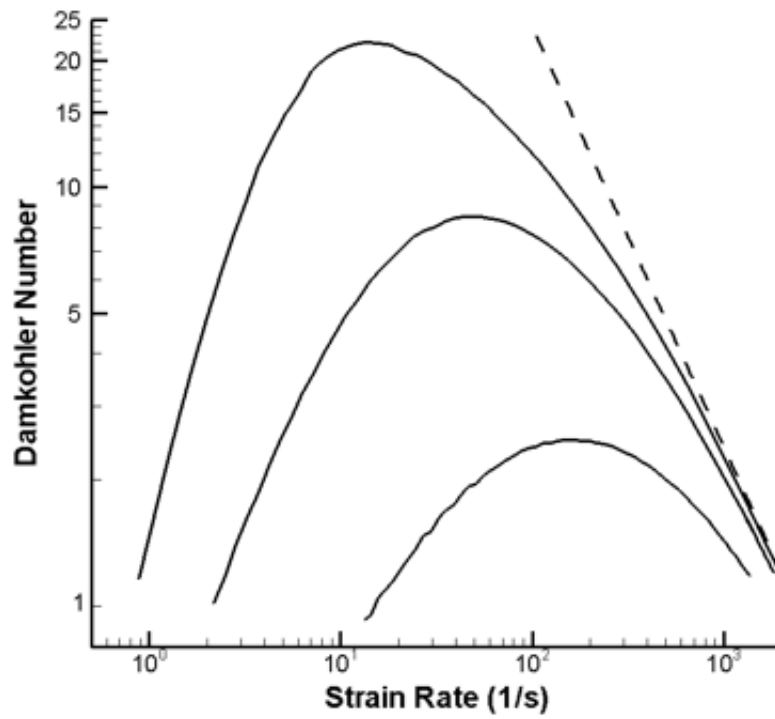
Figure 5.2: Damköhler number versus strain rate α (log-log plot). Top dashed line: adiabatic flame. Three lower solid lines: sooting and radiating flames with $Y_{soot,R} = 0$ (top), 1% (middle), 5% (bottom). The critical values of at the extinction limits are close to 1.
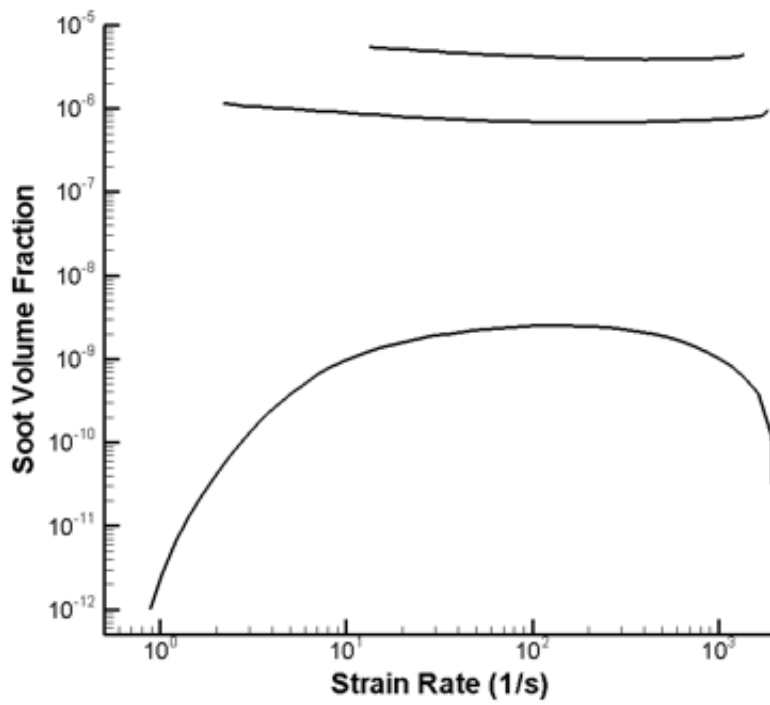
Figure 5.3: Stoichiometric value of the soot volume fraction $f_{v,st}$ versus strain rate α (log-log plot). Three solid lines: sooting and radiating flames with $Y_{soot,R} = 0$ (bottom), 1% (middle), 5% (top).

for $\alpha = 20$ s^{-1}, with and without external soot loading. Under these low strain rate conditions, the effects of radiation cooling are pronounced and are responsible for a dramatic decrease in peak flame temperature equal to approximately 330 K when and 500 K when $Y_{soot,R} = 0.02$ (Figure 5.4).

Figure 5.5 presents the corresponding spatial variations of soot volume fraction across the flame. In the case with $Y_{soot,R} = 0.02$, the soot mass is released upstream of the flame at $x \approx 17$ mm. As they approach the flame zone (i.e., moving from right to left in Figure 5.5), a significant fraction of the soot particles is first consumed by oxidation (a consequence of adding soot on the air side of the flame); the rest is transported across the reaction zone where as mentioned above, the particles contribute to increasing the flame luminosity and to weakening the flame.

Figure 5.6 presents the corresponding spatial variations of the mean absorption coefficient κ. In the absence of soot loading, the flame optical depth τ_R takes low values $\tau_R \approx 0.035$, and the flame remains in the optically-thin regime, i.e., a radiation regime dominated by emission; in contrast, in the case $Y_{soot,R} = 0.02$, $\tau_R \approx 0.12$, and the flame belongs to a mixed radiation regime in which absorption becomes important. Also, while in the case with $Y_{soot,R} = 0$, the contributions of soot and gas radiation to the mean absorption coefficient κ have comparable weights, in the case with $Y_{soot,R} = 0.02$, the soot contribution is clearly dominant.
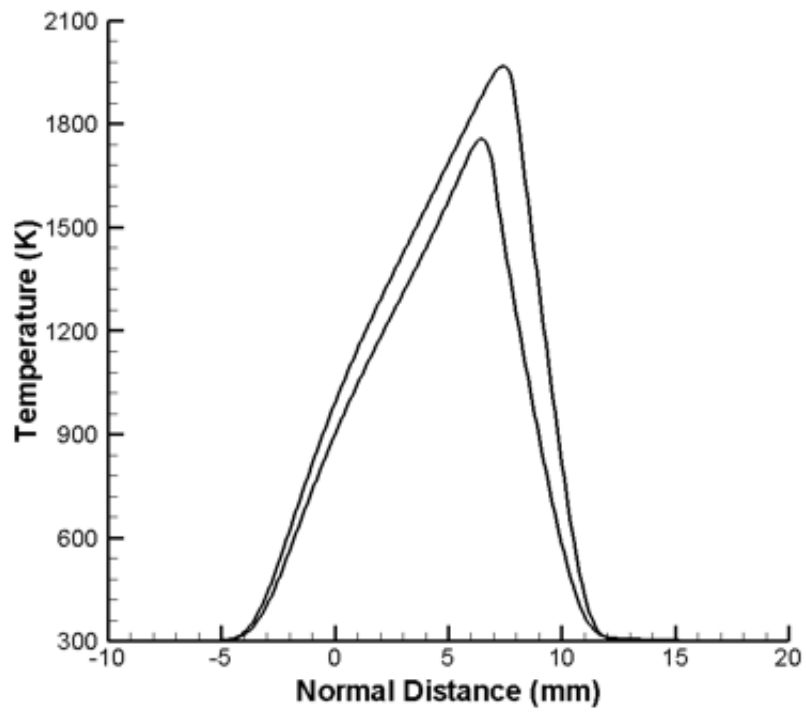
Figure 5.4: Temperature versus normal distance to the flame, $\alpha = 20s^{-1}$. Top line: flame with $Y_{soot,R} = 0$; bottom line: soot-loaded flame with $Y_{soot,R} = 2\%$. $x \leq 5$ mm corresponds to the fuel (air) side of the flame.
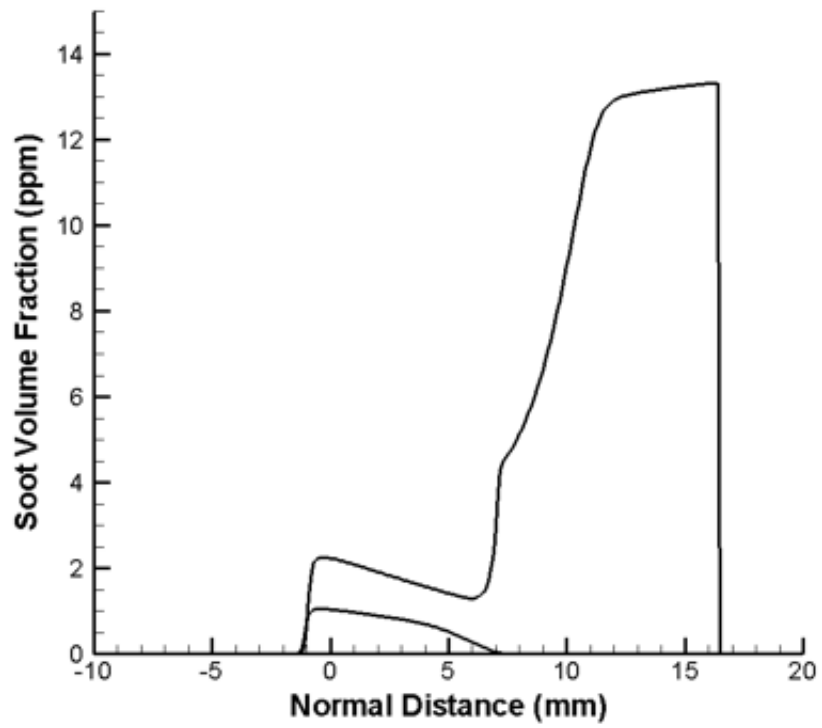
Figure 5.5: Soot volume fraction versus normal distance to the flame, $\alpha = 20s^{-1}$. Bottom line: flame with $Y_{soot,R} = 0$; top line: soot-loaded flame with $Y_{soot,R} = 2\%$. Soot addition occurs at $x \approx 17$ mm .
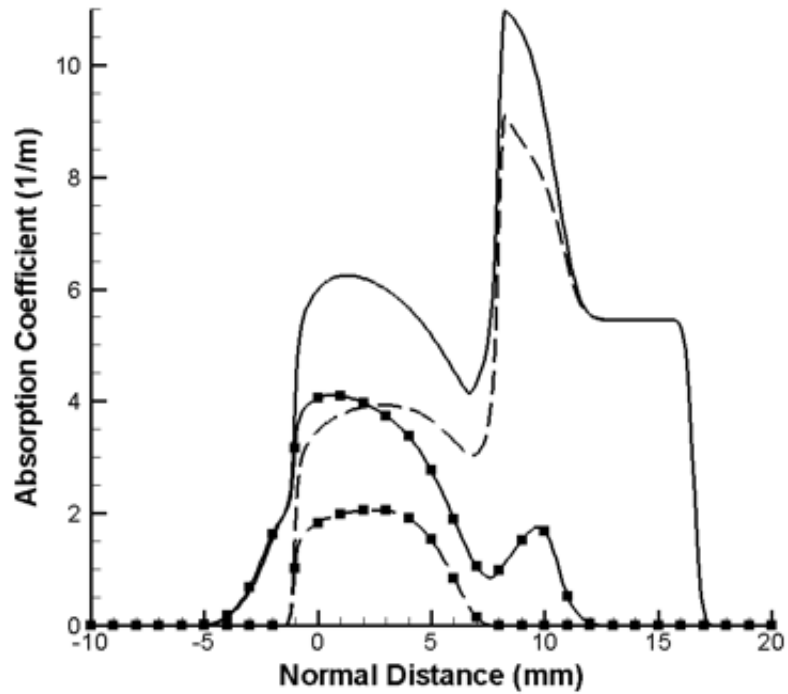
Figure 5.6: Mean radiation absorption coefficient versus normal distance to the flame, $\alpha = 20$ s^{-1}. Bottom lines with square symbols: flame with $Y_{soot,R} = 0$; top lines without symbol: soot-loaded flame with $Y_{soot,R} = 2\%$. For each flame case, the plot shows the total absorption coefficient κ (upper solid curve) and its soot contribution, (lower dashed curve); the difference between the two curves is the contribution of CO_2 and H_2O (see Equation (3.48)).

5.3 Summary

The effect of external soot loading on the extinction limits of laminar counterflow ethylene-air diffusion flames is studied using large activation energy asymptotic theory (Configuration C1). The AEA analysis is extended to include a phenomenological soot model that accounts for particles inception, growth and oxidation, and a generalized treatment of thermal radiation that accounts for both emission and absorption phenomena and applies to participating media ranging from optically-thin to optically-thick. Soot loading is simulated by adding a controlled amount of soot mass to the flow upstream of the flame.

The AEA analysis shows that soot loading results in a significant decrease of the size of the 'flammable' domain: the minimum value of flame stretch at the radiative extinction limit is increased by more than an order of magnitude. These results support the idea that in multi-dimensional sooting flames, soot first produced at locations characterized by fast fuel-air mixing and vigorous combustion conditions and then transported into locations characterized by slow mixing and sluggish combustion conditions will play a dominant role by increasing the local flame luminosity and driving the flame towards radiative extinction. This non-local multi-dimensional effect is believed to be a dominant mechanism to explain flame extinction in fires; this effect is not present in classical (i.e., non-soot-loaded) one-dimensional flame configurations, which suggests that these configurations are not representative of multi-dimensional sooting flame conditions.The present AEA results indicate that in multi-dimensional laminar or turbulent sooting flames, stretched flame elements

with values of the strain rate above approximately 13 s^{-1} (or stoichiometric values of the scalar dissipation rate above 0.4 s^{-1}) will be susceptible to radiative extinction. The AEA results also support the concept of a single critical value of the Damköhler number to predict all flame extinction limits. Future work will consider an application of the present AEA analysis to the construction of flammability maps relevant to fire problems.

Chapter 6

Radiation-driven Flame Weakening Effects in Sooting Turbulent Diffusion Flames

6.1 Turbulent Radiative Extinction

In this chapter, the effect of non-local soot loading is demonstrated in a turbulent framework, to extend upon the theoretical ideas discussed in Chapter 3 (Configuration C2). The interactions between flame, soot, and radiation processes are analyzed in a S3D-based study of two-dimensional, momentum-driven, ethylene-air diffusion flame stabilized near a solid wall surface. The numerical configuration is presented in Figure 6.1. The wall boundary conditions at $y = 0$ correspond to zero velocity, prescribed temperature, $T_w = 300$ K and blackbody radiation $\epsilon_w = 1$. The inflow boundary conditions at $x = 0$ correspond to prescribed velocity, mixture composition and temperature. The free stream corresponds to a uniform flow of air ($u_\infty = 2.5$ m/s) seeded with turbulent-like perturbations (characterized by a high forcing intensity, $u' = 1$ m/s and a small integral length scale $\ell_t = 0.17$ cm). The near-wall infflow profile has a boundary layer thickness $\delta = 0.15$ cm. This is essentially an extension of the earlier work featuring kinetic extinction in conjunction with interaction with cold walls [110], compared to which, the flame-to-wall distance has been increased by 0.5 cm (and is significantly larger than δ and ℓ_t) so that the

simulated flames are only weakly affected by the presence of the wall. Temperature and species mass fractions are specified at $x = 0$ using a laminar flamelet solution in Section 4. For radiation, the inflow/outflow x-boundaries are treated as symmetric and mimic radiation from an infinite flame.

The computational grid size is 1216×376. The grid spacing is uniform in the $x$direction, $\Delta x \approx 66\mu$m, while variable in the $y$direction: the ygrid is uniform in the nearwall and flame regions, $\Delta y \approx 50$ μm for $0 \leq y \leq 1.5$ cm, and is stretched in the freestream region.

Soot is modeled using the two equation transport model described in Section 2.2.3. The absorption coefficients for radiating species is described in Section 3.48 with the notable difference from that study being that the soot absorption coefficient is increased by modifying C_{soot} to 7000 m^{-1}K^{-1} from the recommended value of 1817 m^{-1}K^{-1} in order to accentuate the role of luminous radiation.

Figures 6.1, 6.2 present a typical instantaneous snapshot of the DNS solution. Figure 6.1(a) indicates that the flame features several weak spots, for instance at $(x, y) = (3, 1)$, $(4.5, 0.5)$, $(6.5, 1.5)$ and $(8, 2)$ (in units of cm). These weak spots correspond to low values of the flame temperature (Figure 6.1(b)) and large values of the radiative cooling rate (Figure 6.2(a)). They also correspond to local accumulation events of soot particles (Figure 6.2(b)) and appear to be well-correlated with soot mass leakage from the fuel to the air side of the flame.
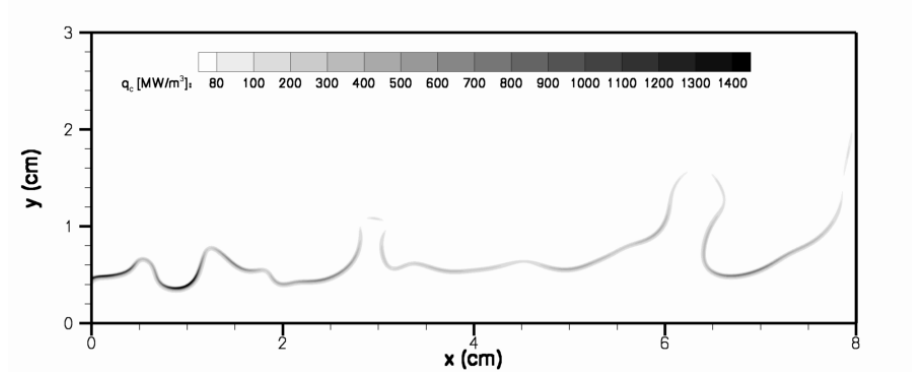
(a) Flame heat release rate $[MW/m^3]$
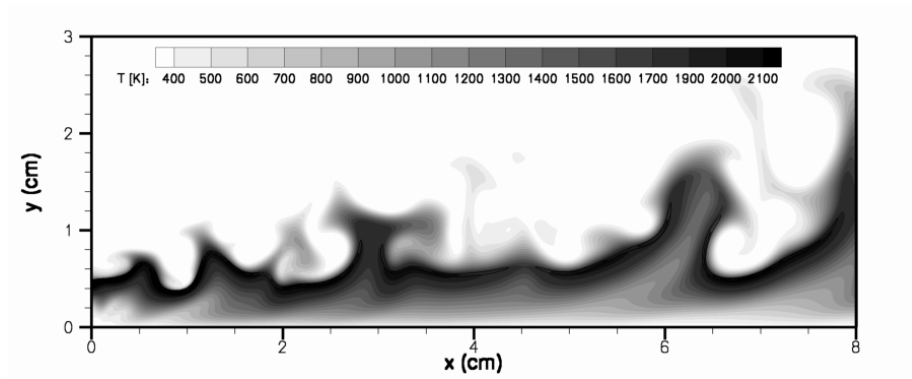
(b) Flame temperature $[K]$

Figure 6.1: Turbulent diffusion flame (6.1). Spatial variation of heat release rate (6.1(a)) and temperature (6.1(b)), superimposed with the stoichiometric mixture-fraction contour (thick black curve). Solution corresponds to strongly radiating flame with increased soot absorption coefficients ($C_{soot} = 7000$ m^{-1}K^{-1}), high turbulence intensity with $u' = 1$ m/s and mean velocity $U = 2.5$ m/s (40%).
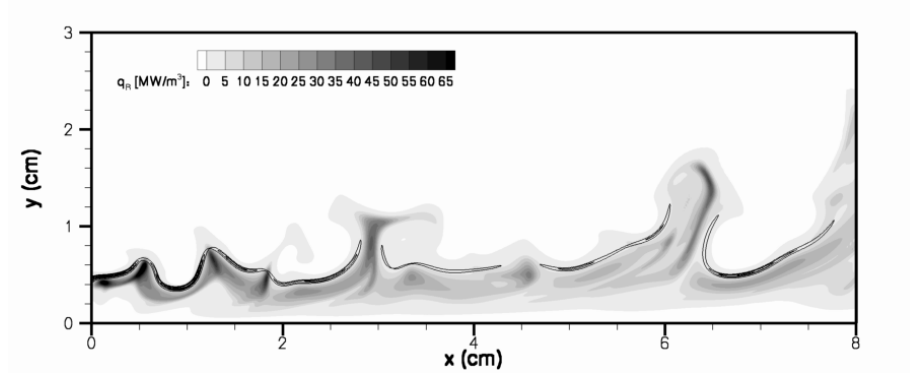
(a) Radiation power density $[MW/m^3]$
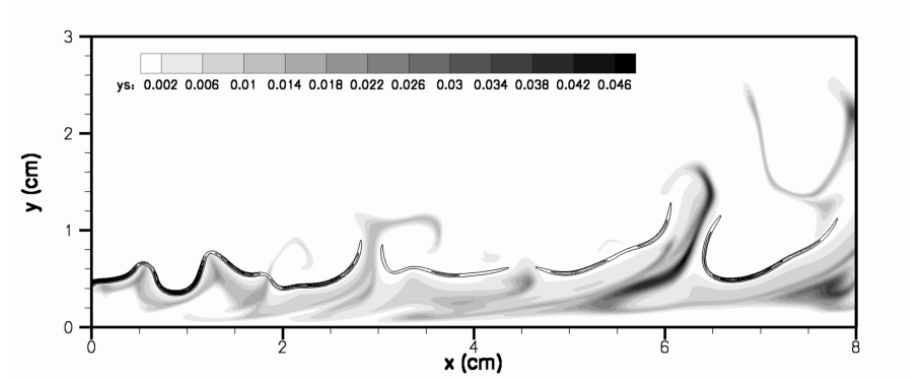
(b) Soot mass fraction

Figure 6.2: Turbulent diffusion flame (6.1). Spatial variation of radiation power density (6.2(a)) and soot mass fraction (6.2(b)), with superimposed stoichiometric mixture-fraction contour(thick black curve). Solution corresponds to strongly radiating flame with increased soot absorption coefficients ($C_{soot} = 7000$ m^{-1}K^{-1}), high turbulence intensity with $u' = 1$ m/s and mean velocity $U = 2.5$ m/s (40%).

6.1.1 Extinction Criterion

The extinction criterion has been rigorously derived for the AEA flames in Chapter 3. This requires the knowlege of the outer or Burke-Schumann temperatures, which, however, is not available in the DNS data. Therefore, for purposes of analysis, one defines a scaled version of the reduced Damköhler number (also done in previous studies [110, 107]) called the flame-weakness factor R in which is used the actual flame temperatures to detect extinction propensity.

$$R = \frac{\delta_*^{UL}}{\delta_*} \tag{6.1}$$

where the superscript UL denotes the upper or high stretch extinction limit. In the foregoing, δ_* and δ_*^{UL} are defined using the actual flame temperatures. In other words the weakness-factor may now be written as

$$R = \frac{T_{st}^{-p-q-3}\chi_{st}\exp(T_a/T_{st})}{T_{st}^{UL^{-p-q-3}}\chi_{st}^{UL}\exp(T_a/T_{st}^{UL})} \tag{6.2}$$

Figure 6.3 presents a slightly different perspective by focusing on flame-based quantities, i.e. quantities that are measured on the stoichiometric isocontour of mixture fraction. Figure 6.3(a) shows that the flame temperature is low at the locations identified in Figures 6.1 and 6.2 as the flame weakest spots. Also, the temperature takes decreasing values as one moves to larger downstream locations, which suggests that the present simulation does not capture the entire history of these weak spots and that further weakening of the flame intensity may be expected beyond $x = L_x$ ($s \approx 12$ cm). The weak spot at $s \approx 12$ cm has a very low temperature, and is likely to have quenched.
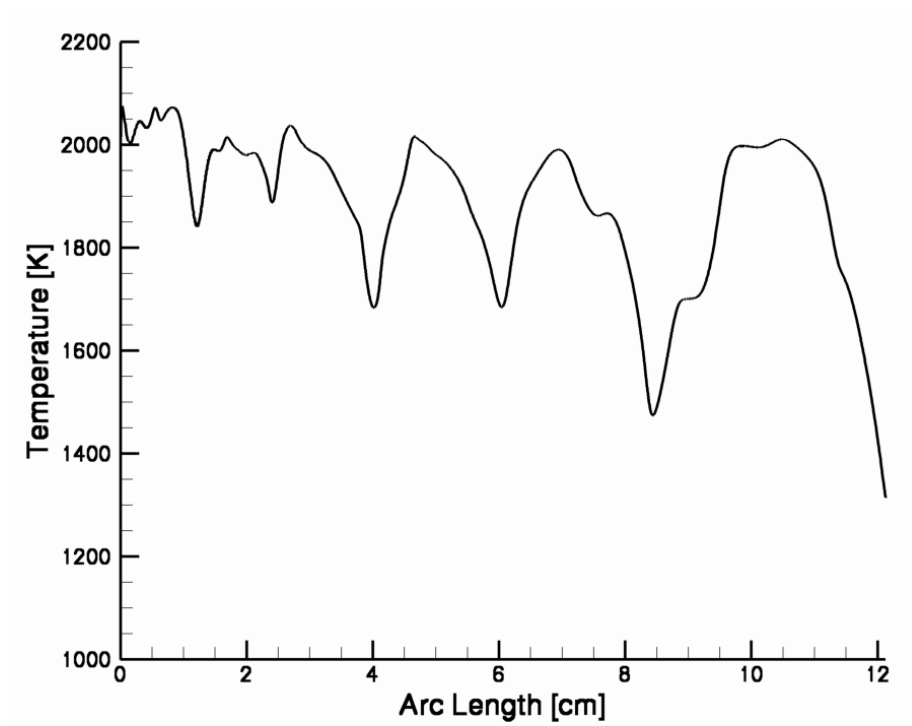
(a) Flame temperature [K]
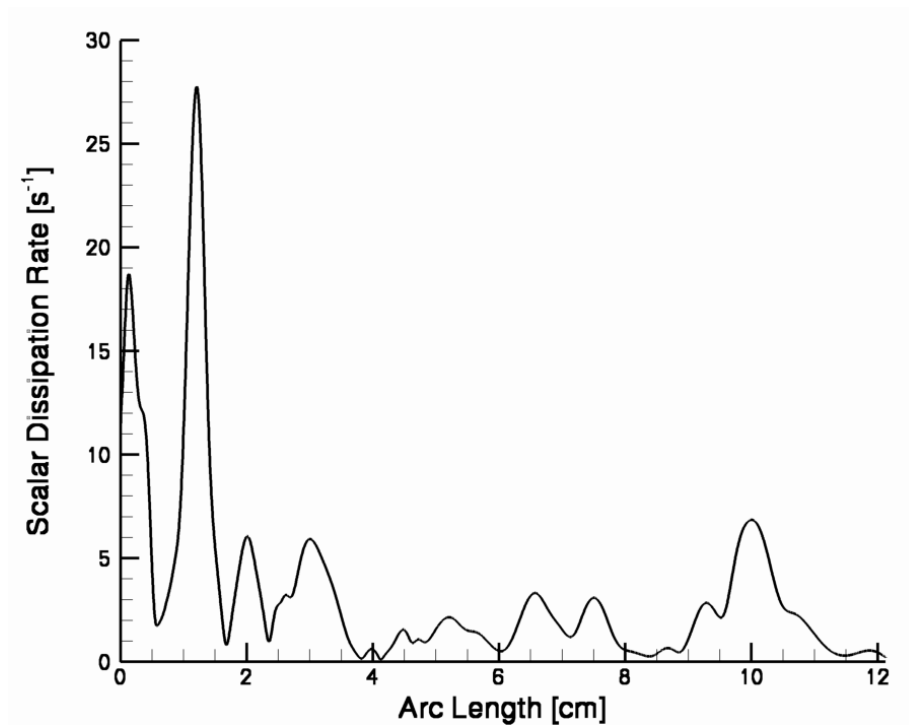
(b) Scalar dissipation rate [s^{-1}]

104
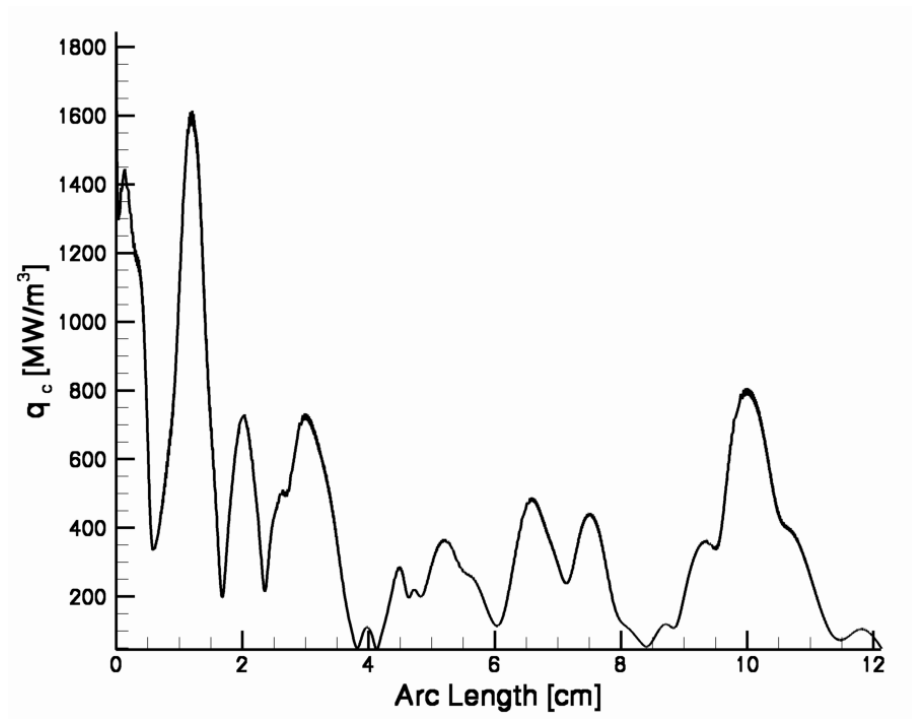
(c) Heat release rate [MW/m^3]
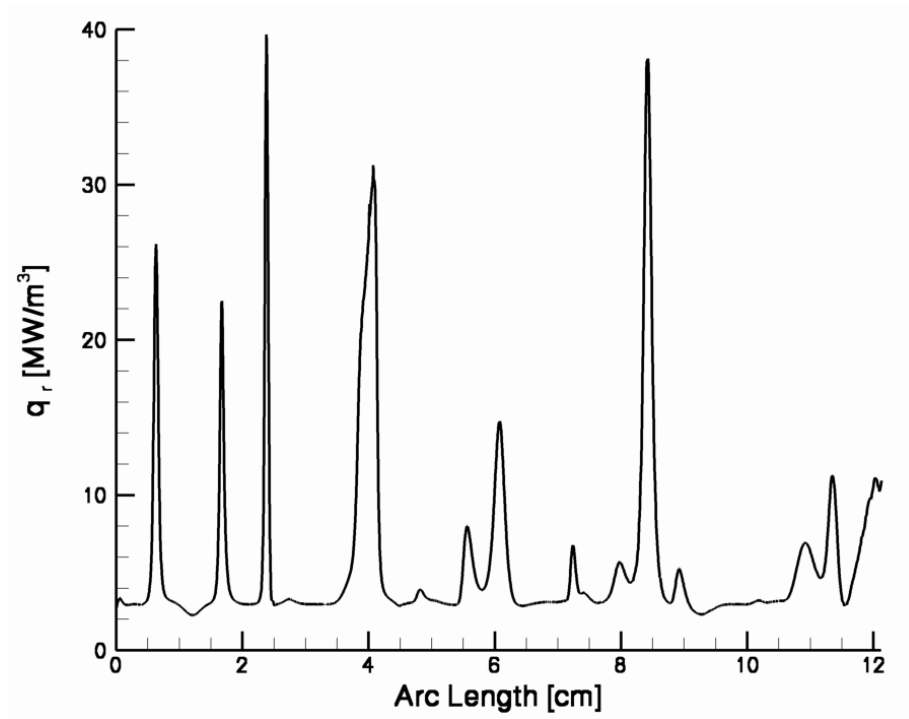
(d) Radiation power density [MW/m^3]
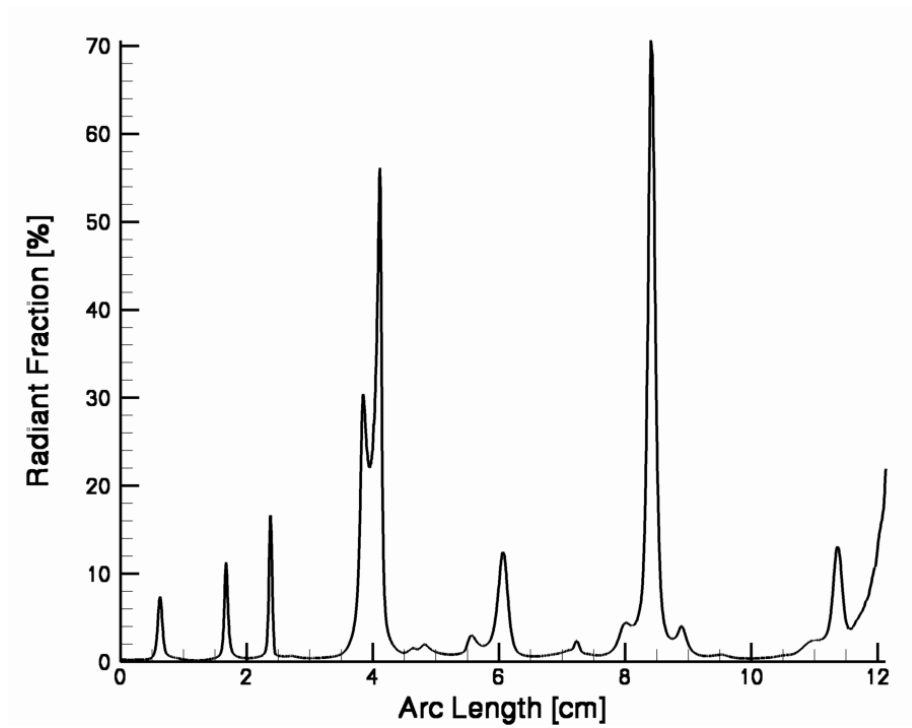
(e) Radiant fraction
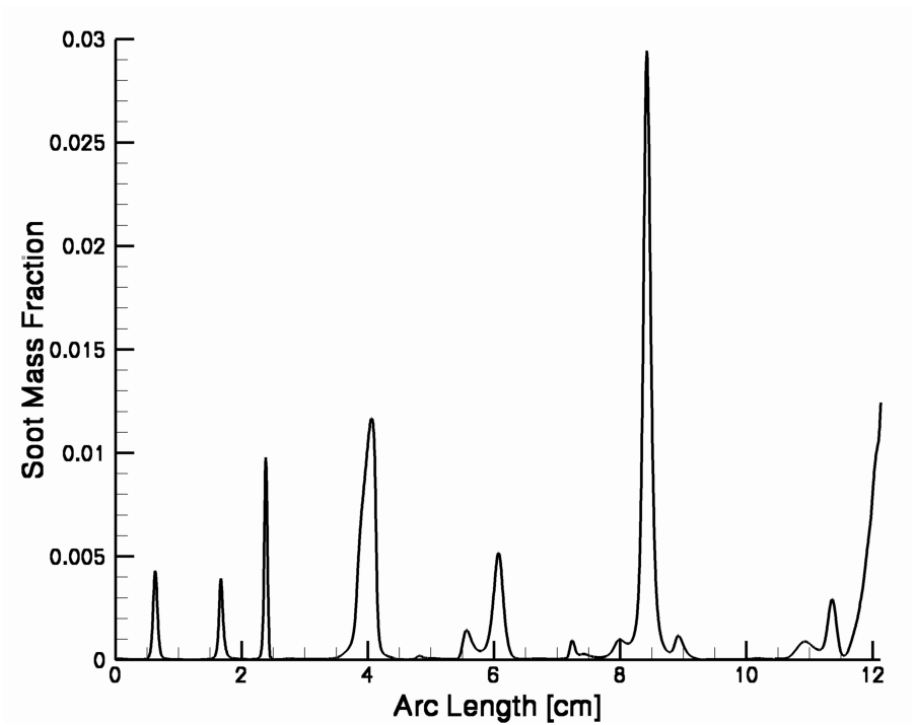
(f) Soot mass fraction
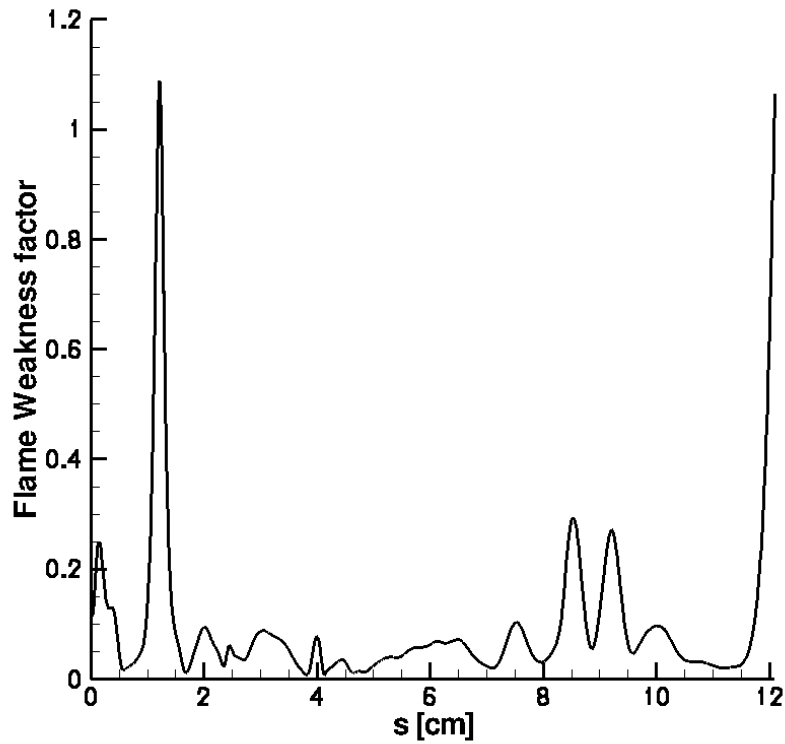
(g) Flame weakness factor

Figure 6.3: Quantities along stoichiometric contour for turbulent diffusion flame 6.1. Flame based quantities T, χ, $\dot{q}_c'''$, $\dot{q}_r'''$, radiant Fraction, soot mass fraction, R are presented as a function of the arc-length s along the stoichiometric flame contour. Flame weak-spots are located at $s \approx$ 4 cm, 6 cm, 8.5 cm, 12cm.

Furthermore, it is found that the flame weakest spots (i.e., those most suscep-tible to extinction) correspond to minimum values of the fuel-air mixing rate χ_{st} (Figure 6.3(b)-except at $s \approx$ 1cm which appears to be weakened by high stretch. This demonstrates that the present flame dynamics are generally different from previous flame extinction events studied in Ref. [110]. In Ref. [110], the simulated flames were closer to the cold wall, exposed to extensive wall-induced convective heat losses, and free of thermal radiation effects; flame extinction events corresponded to peak values of χ_{st} and were representative of the upper limit discussed in Chapter 4. In contrast, in the present study, the flame's weak spots correspond to minimum values of the mixing rate and to maximum values of the local radiant fraction 6.3(e), and may therefore be considered as representative of radiationdriven (lower limit) quasi-extinction phenomena. An interesting facet of the analysis is that like in the soot-loaded asymptotic flames discussed in Chapter 3, the build-up of soot causes radiative flame weakening at much larger stretch rates than the case with no-soot loading (as seen from the laminar flamelet database 4).

Figures 6.3(c) and 6.3(d) present the heat release rate and radiative power along the stoichiometric contour. These plots show that while the heat release rate is generally much larger than the radiation cooling rate, locations corresponding to low stretch rates have low heat release rates, causing them to lose an excessive portion of heat to radiation. This is further exemplified in Figure 6.3(e) which shows that, this profile is *spiky* (i.e., is strongly peaked), and can take values of upto 70%. The spikiness in the radiation cooling rate profile correspond to locations where there is a build up of soot, as seen in Figure 6.3(f). The radiation and soot profiles

seem very well correlated.

The flame weakness factor (the inverse of the reduced Damköhler number is presented in Figure 6.3(g)). There are only two locations where the weakness factor exceeds unity (at $s \approx 1$ cm and $s \approx 12$ cm. The first of these is kinetically weakened, while latter has fallen to a very low temperature of 1200 K. It is stated that this location, while seemingly extinguished, is an outlier- an anomalous point- in that they were formed during the initial violent perturbation in the absorption coefficient, and are most likely not representative of the dynamics. These radiative extinction data are to be analyzed by disregarding these points. Also, the event with large weakness factor corresponds to an increased scalar dissipation rate-this could be a candidate for kinetic extinction, but the event dissipates during the course of time, with nothing remarkable occuring to it. However, the other locations where the flame is radiatively weakened show comparatively low values of the weakness factor. It is also observed that these spots, while being weak, are not quenched (which might occur if the domain is long enough).

6.1.1.1 S-curve

A scatter plot of T_{st} and χ_{st} (Figure 6.4) reveals that the flame dynamics are driven by radiation, when plotted along with data from the laminar flamelet database 4. The anomalous points (which correspond to those subject to the initial large radiation perturbation) were removed from the scatter plot. That the scatter data is enveloped by the points from the laminar steady database is indicative of

the fact that these turbulent flames may be reasonably described by the laminar AEA theory developed in Chapter 3

6.1.2   Extinction Map

Extinction maps are constructed by taking the locus of points where δ_*, the reduced Damköhler number takes values of unity, since it is assumed that $\delta_*^{UL} \approx 1$ at extinction (since the outer temperatures are not available, the actual flame temperatures are used). For extinction, the analysis indicates that $\delta \leq \delta_*^{UL}$ or $R \geq 1$ in Equation (6.1). Figure 6.5 shows contains an extinction map constructed using the above-mentioned approach, which is used to give the critical flame temperature for a given mixing rate χ_{st}, by solving the equation $\delta_* = 1$. Thus, one transitions from burning to non-burning when one moves to the right of the curve at a given temperature, or when one moves down, at a given scalar dissipation rate. Data is plotted from various flame weakening events tracked in time. Inspection of the map reveals that while some of these events show low temperatures ($\simeq 1600$ K), all the points lie above the critical temperature curve, and are not extinguished. This is consistent with observations (such as the heat release rate being non-zero) showing that the weak spots are not quenched. It is concluded that the length of the domain is not large enough to provide residence times long enough to allow radiative extinction to take place.
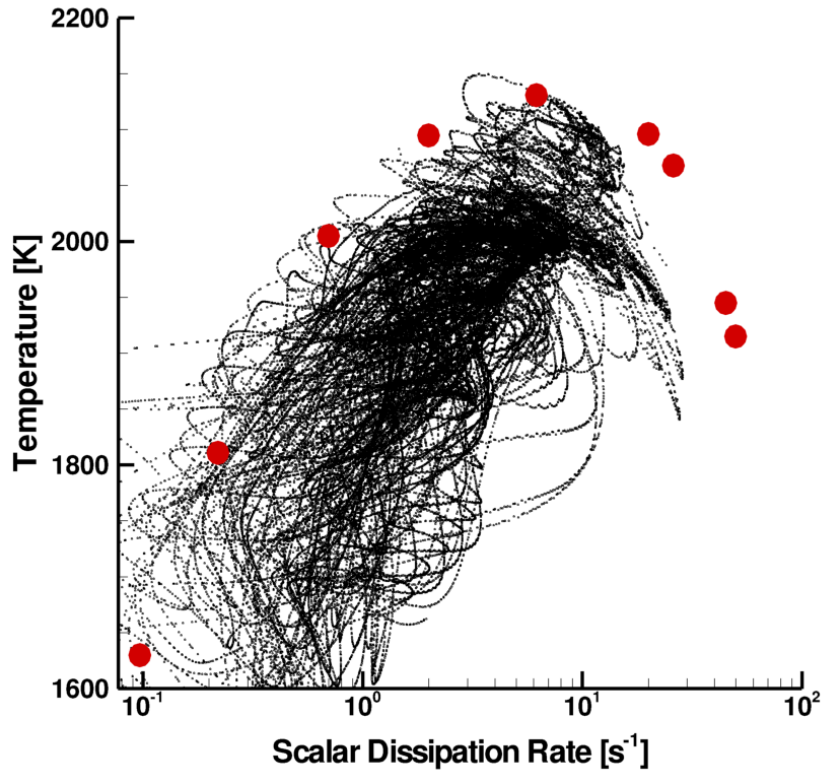
Turbulent diffusion flame (6.1)

Figure 6.4: S-curve: Stoichiometric flame temperature versus fuel-air mixing rate. The small circles (black) are points from turbulent flame undergoing radiative extinction. Large Circles (red) are from the laminar flamelet database.
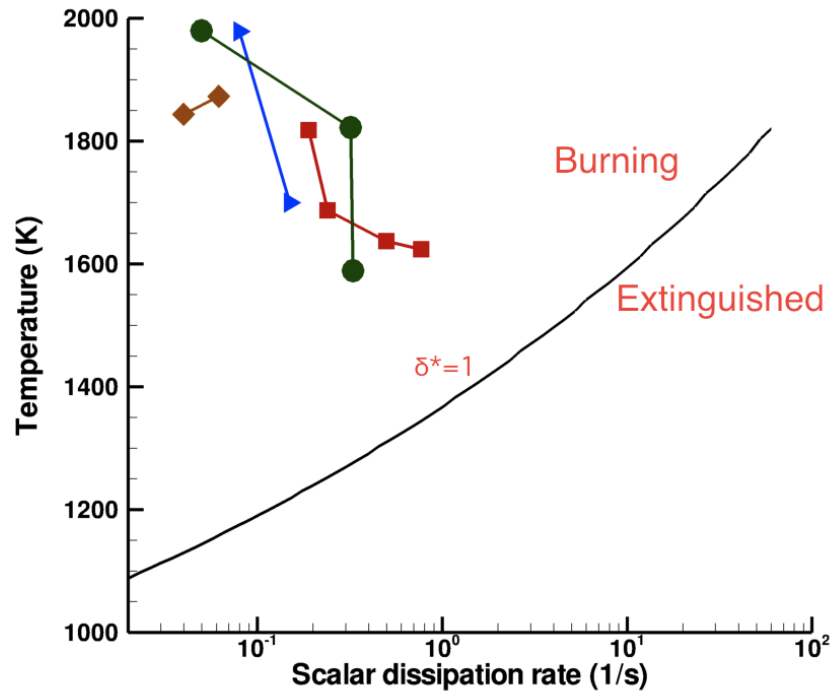
Turbulent diffusion flame (6.1)

Figure 6.5: An extinction map: Stoichiometric flame temperature versus fuel-air mixing rate, from data collected from the flame weak-spots (regions where the flame is weakened by radiation heat loss) at various times. Each colored line with symbols corresponds to the time evolution of a particular flame weakening event. The curve comprising the critical flame temperature, calculated as the locus of points where Equation (6.1) holds is the solid black line.

6.2   Summary

DNS is used in this study to bring basic information on the behavior of diffusion flames that are weakened (but not extinguished) by the effect of radiation heat loss in a turbulent wall-bounded flame configuration (C2), where the soot absorption coefficient has been artificially increased by a factor of 10 to accentuate the role of luminous thermal radiation. The study extends upon the presented in Chapter 3 to a turbulent framework, and complements the assertion made previously that non-local soot loading at the flame (i.e. soot arriving at the flame from elsewhere, as in a large fire) tends to make these flames more susceptible to radiative extinction phenomena.

Analysis of the flame structure of these turbulent flames compare favorably with the laminar AEA flame analysis in terms of the qualitative features-radiative weakening and extinction-like events occur at low stretch rates, and are characterized by large radiant fractions and soot loading. However, while weak spots are seen, complete extinction of these flames does not occur (which is mirrored in the extinction criterion diagnostic) Soot breakthrough phenomena are observed, but these soot leakage events do not seem to arise as a consequence of radiative extinction, but because of a plausible suppression of soot oxidation chemistry.

Chapter 7

Dynamics of Flame Extinction in Non-Premixed Flames Interacting
with Fine Water Spray

In this chapter, interaction of turbulent nonpremixed flames with fine water
spray is studied using Direct Numerical Simulations (DNS) with detailed chemistry
(Configuration C3). The study is of practical importance in fire safety devices that
operate in the mist regime, as well as in their use as an inexpensive temperature
control mechanism for gas turbines. Dynamics of water spray is represented by the
Lagrangian particle-in-cell method, coupled with an Eulerian gas-phase reacting
flow solver. The model configuration is a two dimensional ethylene-air counterflow
diffusion flame at moderate strain rates. Laminar and turbulent flame simulations
are performed at various water loading conditions. Comparison of various simula-
tion cases highlights the flame weakening characteristics due to aerodynamic stretch
and heat loss due to water spray evaporation. Local flame extinction is identified
by a Damköhler number criterion, derived in Chapter Asymptotic-analysis based
on an asymptotic model (the inverse of that quantity is used in this chapter, a
quantity known as the flame-weakness-factor) under non-adiabatic environments.
A statistical analysis of the cumulative turbulent flame data shows that a large heat
release enhancement is observed during the flame quenching due to the occurrence
of edge flames, while such effects are substantially reduced in the presence of wa-

ter spray. Findings from this study provide a better understanding of interaction between thermal and aerodynamic quenching in turbulent flame dynamics.

Advances in high performance computing have allowed for first-principle direct numerical simulation of turbulent combustion with detailed chemistry and transport properties. Recent DNS studies [65, 11, 83, 117] have demonstrated that laboratory-scale turbulent flames can be computationally reproduced to yield detailed information of flow and reactive scalar variables with full temporal and spatial resolution, thereby providing valuable insights into the advanced models that can better describe fundamental combustion processes in practical devices. Recent developments in combustion DNS have enhanced the fidelity of underlying physical submodels to describe soot formation, radiative heat transfer, and spray evaporation [39, 3, 109].

The primary scientific goal of this study is to unravel, by means of detailed numerical simulations, the physical processes responsible for flame extinction due to evaporating water spray. The problem is of practical interest in fire safety application, in which utilization of fine water droplets is considered a more effective means for flame suppression. In particular, we attempt to develop a unified criterion for flame extinction that extends the classical extinction strain condition to include non-adiabatic configurations in which additional flame weakening arises from heat losses due to evaporative cooling or thermal radiation. It is recognized that flame extinction occurs from combined effects of strain, preferential diffusion, and heat losses, such that the corresponding extinction condition for nonpremixed laminar flames, usually given by the critical scalar dissipation rate, needs to be appropriately modified to account for other external flame weakening effects. Recent studies

115

[110, 71, 70], addressed this issue for turbulent flames subjected to strong radiative cooling wall heat loss or soot radiation. The present study extends and complements this work by considering water spray evaporation, as an attempt to unify various flame weakening effects into a single parameter. The present study also showcases recent developments in combustion DNS coupled with Lagrangian spray dynamics [109], on which the current study builds upon (the current study consists of the same numerical code-base as in [109]).

The adopted model problem configuration consists of two-dimensional laminar and turbulent counterflow nonpremixed flames of ethylene and air, interacting with monodisperse dilute water spray injected from the air stream. Details in the computational development of the problems are described in Chapter 1, which includes a conservative treatment of coupling between Lagrangian spray droplets and the Eulerian gas-phase fluid dynamics, and modified characteristic boundary conditions to account for spray evaporation effects. Recognizing the limitations of the two-dimensional configuration in representing realistic turbulence, the model problem under study allows multiple simulations for parametric investigation at a reasonable computational cost. The counterflow configuration has recently been adopted in turbulent flame studies in favor of its compact dimension and well-defined boundary conditions [27]. In this study, test cases at various droplet loading conditions and strain rates are analyzed in terms of a theoretically developed extinction criterion in order to quantify the level of flame weakening and the onset of extinction.

7.1 Unified Extinction Criterion

According to laminar flame theory, first derived by Liñan [53], flame extinction occurs when the flow residence time becomes shorter than a critical limit below which intense chemical reactions are not sustainable. For nonpremixed flames, such a condition is identified by the extinction strain rate, or more formally by the scalar dissipation rate based on the mixture fraction variable. Although the extinction scalar dissipation rate is considered a unique property of a fuel-air mixture under a given initial enthalpy condition, studies of flames with radiative heat losses [22, 111, 70] reported dual extinction limits, the lower of which is induced by the flame weakening due to the heat loss. This has been the subject of chapter 3 where theoretical developments to extend upon the earlier works were focussed on. Following the asymptotic analyses that these efforts concerned themselves with, this leads a scaling relationship for the reduced Damköhler number, δ_* (sketched out in full in equations (3.102), (3.118))

$$\delta \sim \frac{1}{\chi_{st}} \exp\left(-\frac{T_a}{T_{st}}\right) \tag{7.1}$$

In the foregoing, the algebraic factor T_{st}^{p+q+1} that appears in the more exact expressions (3.102), (3.118))is disregarded because the aim is to obtain an expression that may be used with *detailed* chemistry, under which conditions the fuel and oxidizer coefficients p, q used in chapter 3 are unknown.

In the above expression, extinction is envisaged to occur if δ falls below a critical extinction limit. This may happen when the mixing time scales become small, $\chi_{st} < \chi_{st,critical}$, or when the chemical time-scales become large $T_{st} < T_{st,critical}$. Re-

calling the dual extinction limits [22, 111, 70], and in chapter 3, the high-stretch limit corresponds to strain induced extinction, while the low-stretch limit is primarily due to the suppressed chemical reactivity due to the excessive radiative heat loss. The weakening of chemical reactivity may also be caused by other physical processes, such as evaporative cooling of water spray (the subject of the present study); all of these flame weakening effects are manifested by a reduced flame temperature, in conjunction with a high rate of stretch (indeed, this may be viewed as a high-stretch extinction limit exacerbated by lowered flame temperature, somewhat akin to the effect caused by soot loading at high stretch in chapter 3).

The above discussion suggests that various extinction mechanisms may be described by a unified extinction criterion, implied by a reduced Damköhler number δ_* as discussed in detail in Chapter 3, which is redefined below for the present study with evaporating spray as follows

$$\delta_* = const \frac{\exp\left(-\frac{T_a}{T_{st}}\right)}{\chi_{st}} < 1 \tag{7.2}$$

in which the notation is consistent with Chapter 3. The foregoing equation contains a constant multiplicative factor $const$, which will be removed by rescaling with the extinction conditions as follows.

If, at the extinction conditions (the classical, or kinetic extinction limit under adiabatic conditions), one denotes the stoichiometric flame temperature and scalar dissipation rate by $T_{st,ext}$ and $\chi_{st,ext}$, one may define a scaled version of the reduced Damköhler number criterion as follows

$$\delta_* = \frac{1}{R} < 1 \tag{7.3}$$

where the quantity R is given the name "the flame weakness factor", consistent with previous studies by the group [110], [71]. It is fleshed out below:

$$R = \frac{\chi_{st} \exp(T_a/T_{st})}{\chi_{st,ext} \exp(T_a/T_{st,ext})} \tag{7.4}$$

where subscript ext denotes the extinction conditions for the adiabatic flame. Extinction is identified by $R > 1$. Note that such a simple description is based on a number of assumptions, such as a one-step global reaction with Arrhenius kinetics and unity Lewis numbers. A similar form of Equation (7.4) has been adopted in the study of turbulent flame-wall interaction [110], and in [71], developed and refined for the more controlled laminar asymptotic study [70]. The present study investigates the validity of the approach in identifying laminar and turbulent ethylene-air flame extinction by water spray evaporation by testing the approximate expression (7.4) with DNS data.

7.2   Problem Configuration

Figure 7.1 shows the flame configuration under study. The flow configuration corresponds to two dimensional, laminar and turbulent counterflow flames with ethylene-air chemistry, with detailed transport properties (non-unity Lewis numbers) and a reduced chemical mechanism. The reduced chemical mechanism based on the directed-relation graph technique [60] was adopted. The mechanism was validated against the original detailed mechanism by comparing the results of ignition delay, residence time, and laminar flame speeds at various pressure and equivalence ratio conditions [60]. The mechanism consists of 19 major species, 10 quasi-steady

species, and 167 reaction steps. The domain size was $1 \text{ cm} \times 2 \text{ cm}$ with 600×800 grid points in the x and y directions. The inlet temperature and pressure were at 300 K and 1 atm. The steady counterflow diffusion flame was initialized first by overlaying the 1-D solution from OPPDIF [43] onto the 2-D domain, and temporally evolving the solution until it reached a steady state. Subsequently, water spray droplets of 10 μm size diameters were injected at 1 mm distance from the flame on the oxidizer side, matching the local gas x-directional gas speed at injection location. Laminar flame tests were conducted with two different strain rates. For the turbulent cases, homogeneous isotropic turbulence was injected at both inlets by first generating an auxiliary 2-D field using a prescribed energy spectrum, which was then translated from the spatial domain into the time domain by using the Taylor hypothesis.

The DNS solver (S3D), used in several other studies [110, 109, 71] is described in Chapter 1. The spray droplets are treated in a Lagrangian formulation (Section 2.2.5), where the drag force is derived by the Stokes law, and the heat conductivity is assumed infinite inside the droplet. The Lagrangian particles are coupled to the Eulerian gas equations through the mass, momentum and energy source terms associated with water evaporation [109, 3]. Improved characteristic boundary conditions were also developed to account for spray evaporation effects at the outflow boundaries [3].

As for the diagnostics, the consideration of the additional water stream due to spray evaporation required a modified formulation of the mixture fraction variables and state-relationships, details of which are described in Appendix A. In applying Equation (7.4) as the extinction criterion, the global activation energy, T_a, for the
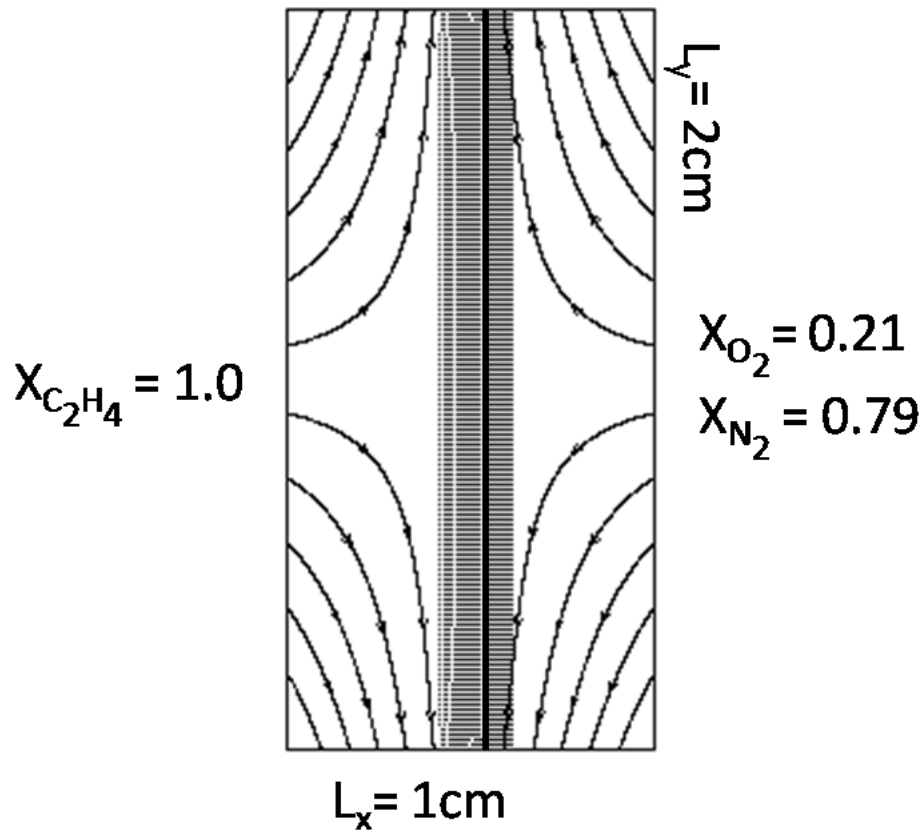
Figure 7.1: Computational configuration. Solid lines with arrows denote potential flow streamlines. Dotted lines represent temperature contours. Solid black line within the temperature contours indicates the stoichiometric mixture fraction identifying the flame location.

ethylene-air flame was determined following the method Sun *et al.* [92], and was found to be 18, 692 K. For the nonpremixed flame considered, the extinction scalar dissipation rate for the adiabatic flame without spray was at $\chi_{st,ext} = 116$ s^{-1}.

7.3   Results

7.3.1   Laminar Flames

Table 1 shows the three laminar cases under study. The scalar dissipation rate and the specific flame power (average heat release rate per unit flame area) are based on the initial steady state diffusion flame. The water loading parameter (WLP) is defined as the actual amount of water evaporated normalized by the initial flame power. In case there is a significant temporal variation in WLP, the maximum attainable value was used. Flame extinction was observed for Cases B and C only; for Case A, both fluid dynamic strain and water loading were not sufficient to quench the flame.

Table 7.1: Parameters used for three laminar test cases

Case	χ_{st}	Specific flame	WLP (%)
A	13.3 s^{-1}	400 kW/m^2	7.5 %
B	13.3 s^{-1}	400 kW/m^2	18 %
C	24.5 s^{-1}	600 kW/m^2	11.5 %

Figure 7.2 shows a temporal evolution of flame quenching by water spray, for Case B. As the injected water spray approaches the reaction zone, the heat release
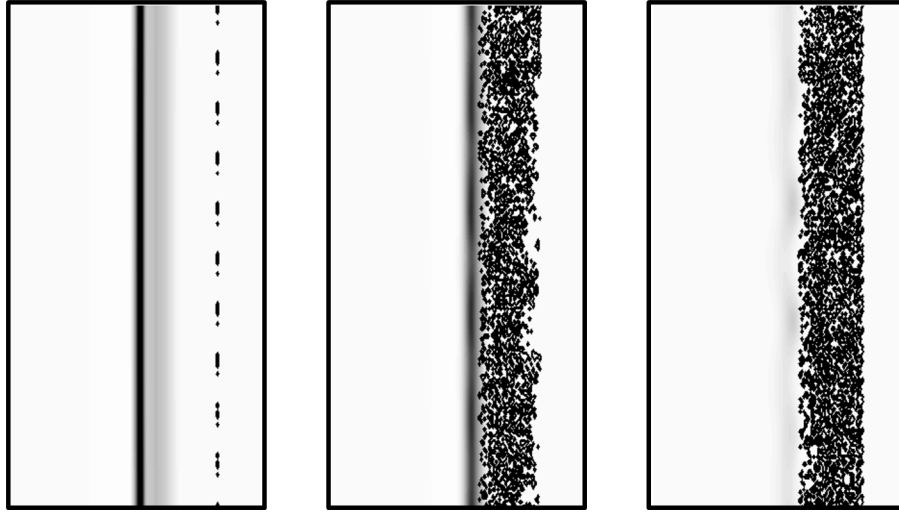
Figure 7.2: Heat release rate isocontours with spray overlay (small dots) for Case B at $t = 0.3, 5.7, 6.2$ ms (going from left to right as the simulation progresses).

rate is locally reduced. The spray is monodisperse and its density is uniformly distributed, such that the flame weakening is also uniformly spread along the flame. Therefore, the analysis of a representative flame structure was conducted along the flame norm at the midpoint of the flame. Figure 7.3 shows the temporal history of the integrated heat release rate (IHR) across the flame norm (in kW/m^2) and the flame weakness factor, R, for the three simulation cases. The flame in Case A is has a very small value of R, and no extinction occurs. For Cases B and C, an abrupt drop in IHR coincides with an increase in R value above unity. Therefore, it is qualitatively found that the $R = 1$ criterion appropriately identifies the onset of flame extinction. To further examine if the extinction criterion captures the local extinction events, Figure 7.4 shows an instantaneous image of the scalar dissipation rate, IHR, and R distribution along the flame surface (represented by the stoichio-
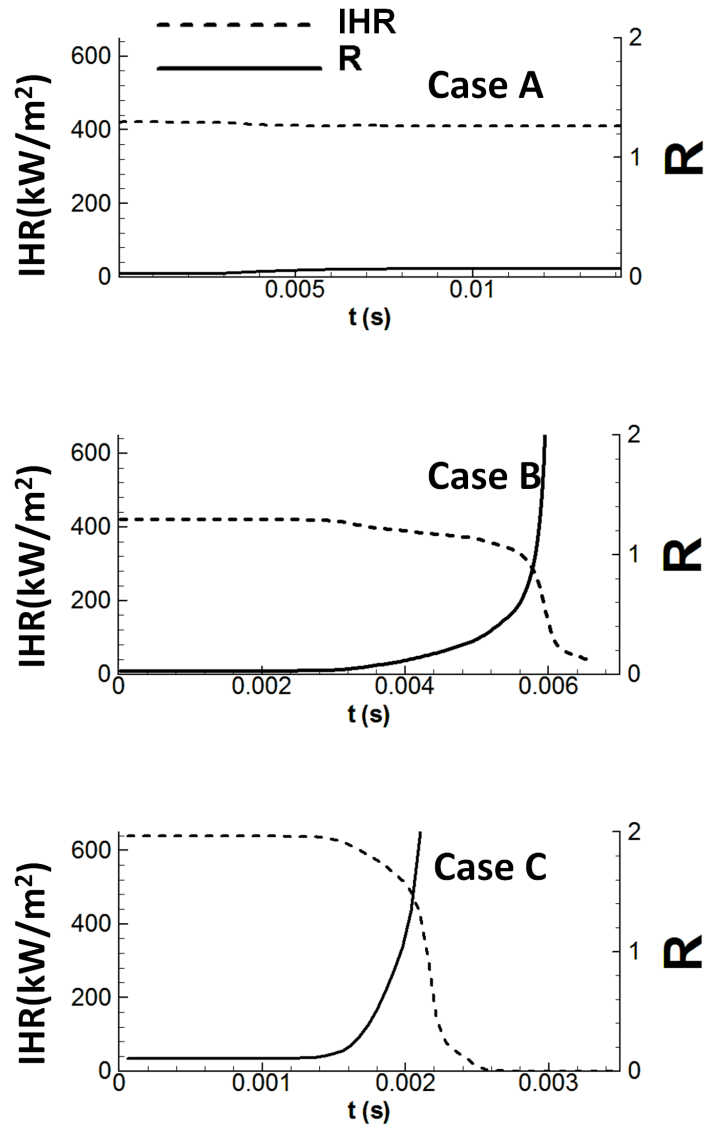
Figure 7.3: Temporal history of integrated heat release rate (IHR) and weakness factor (R) at the midpoint of the flame, for the three cases considered.
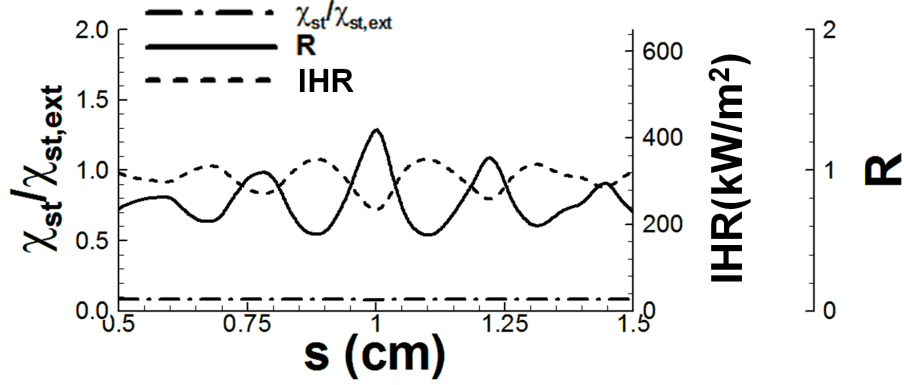
Figure 7.4: Spatial distribution of normalized scalar dissipation rate, integrated heat release rate and the weakness factor along the flame surface for Case B at $t = 5.9ms$.

metric mixture fraction line), for Case B at $t = 5.9$ ms, which is approximately at the onset of local extinction event. The results further demonstrate that the peaks in the R factor accurately identifies the local IHR minima, thus providing correct information to detect extinction points. On the other hand, the normalized scalar dissipation rate shows little variation across the entire flame surface. Therefore, Figures 7.3 and 7.4 show that the R factor serves as a valid metric to determine the level of flame weakening and subsequent extinction.

7.3.2 Turbulent Flames

Based on the reference laminar flame studies, two-dimensional turbulent flame simulations were conducted. The steady laminar flame for Case C (at $\chi_{st} = 24.5$ s^{-1}) was used as the initial condition, on which homogeneous turbulent flow was created and injected at both inlet boundaries. As for the turbulence parameters, the integral length scale ($L11$) was 0.5 cm, and the turbulence intensity was 0.85 times the mean

inlet velocity, such that the turbulent Reynolds number was 654. The turbulence parameters were selected such that turbulent eddies were strong enough to cause strain-induced extinction at some flame locations. A second simulation was run with exactly identical turbulent conditions and an additional spray injection was imposed at $WLP = 20\%$. By comparing the two simulation data sets, the additional flame weakening by spray can be clearly identified.

Figure 7.5 shows the temporal evolution of the heat release rate isocontours as the turbulent flow interacts with the planar flame. At 4.1 ms, the turbulence-induced strain enhances mixing, resulting in a temporary increase in heat release rate. Further increase in the local scalar dissipation rate creates an extinction event, with two visible edge flame structures at 4.7 ms. After the local extinction, the local strain rate decays and the two edge flames propagate onto each other along the stoichiometric line, recovering a connected flame structure at 5.1 ms.

Figure 7.6 shows the spatial distribution of the normalized scalar dissipation rate, IHR, and R along the flame surface for the four instantaneous moments shown in Figure 7.5. Figure 7.6 shows only part of the flame length of 1 cm near the location of the extinction event. At 4.1 ms, a moderate increase in IHR is shown, along with the R factor increasing above unity, indicating that a subsequent extinction event is imminent. At two subsequent times, a large peak in R appears as the local heat release rate drops to exhibit an extinction event. On the other hand, the normalized scalar dissipation rate remains lower than unity throughout the entire event. Once the local extinction occurs and the two distinct edge flames form (noticeable at 5.1 ms), IHR peaks indicate that the local heat release rate is significantly higher
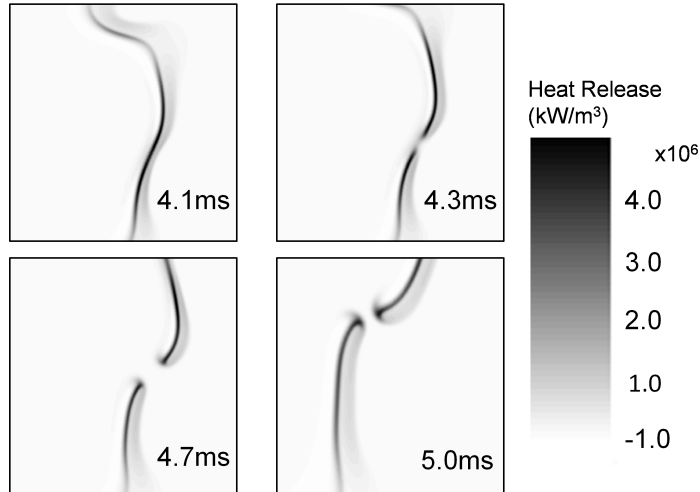
Figure 7.5: Temporal evolution of heat release rate isocontours for turbulent flame simulation without spray. These pictures are zoomed into a 0.8 cm × 0.8 cm region in which the flame undergoes a flame extinction event.

than that of the original laminar flame. This is due to the typical edge flame behavior that the burning characteristics at the edge is closer to those of a stoichiometric premixed flame, exhibiting the peak heat release rate substantially higher than that in the trailing diffusion flame branch [38].

Figures 7.7 and 7.8 show four similar instantaneous images and corresponding distribution along the flame surface for the turbulent flames with spray. The initial local extinction point is identified to be the same as in the no-spray case, but this time the two edge flames retreat from each other, leading to a total extinction of the entire flame. This is due to the additional flame weakening provided by the spray evaporation. The additional flame weakening is further evidenced in Figure 7.8 (at 4.2ms) in that the IHR peaks representing the two flame edges show heat release values much lower than those in the previous case without spray. Again, $R = 1$
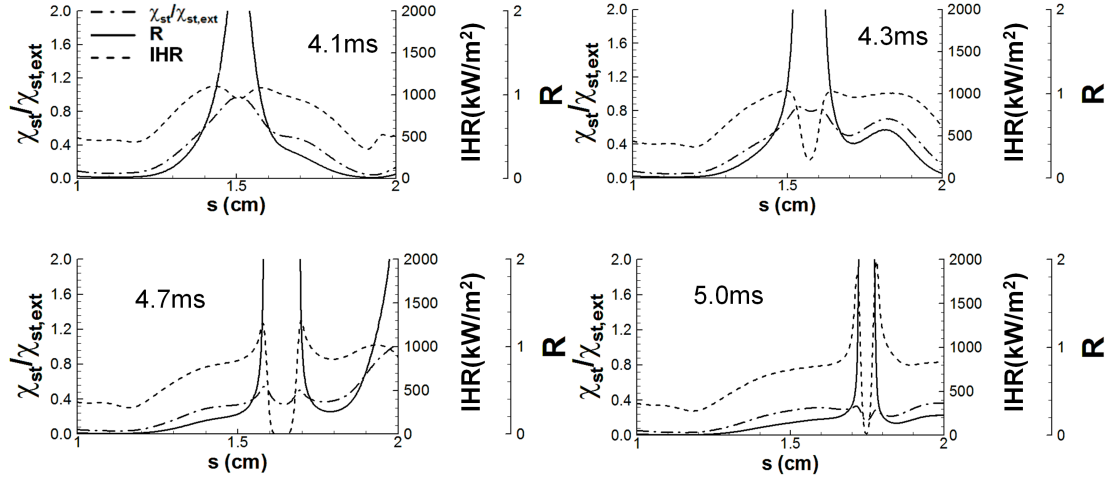
Figure 7.6: Distribution of the normalized scalar dissipation rate, integrated heat release rate (kW/m^2) and the weakness factor for the turbulent flames without spray at the four different times shown in Figure 7.5. Only part of the flame region near the location of extinction is shown here.

appears to serve as an accurate criterion to predict imminent local extinction (at 3.7 ms), while the scalar dissipation rate no longer provides any meaningful information about the state of the flame strength. In the context of turbulent combustion modeling, statistical data for the R factor distribution in turbulent flames are investigated. Figures 7.9(a) and 7.9(b) show the time-cumulative scatter plot of IHR versus R factor along the stoichiometric line for the turbulent flame case without and with spray, respectively. For $R < 1$, the flame strength increases with an increase in R. This is a weak strain (high Damköhler number) regime of the flames in which a higher strain rate provides more reactants to the flame, thereby enhancing the burning intensity. The $R = 1$ line is the suggested extinction condition, but there are surprisingly a large number of data points to indicate that the flame segments
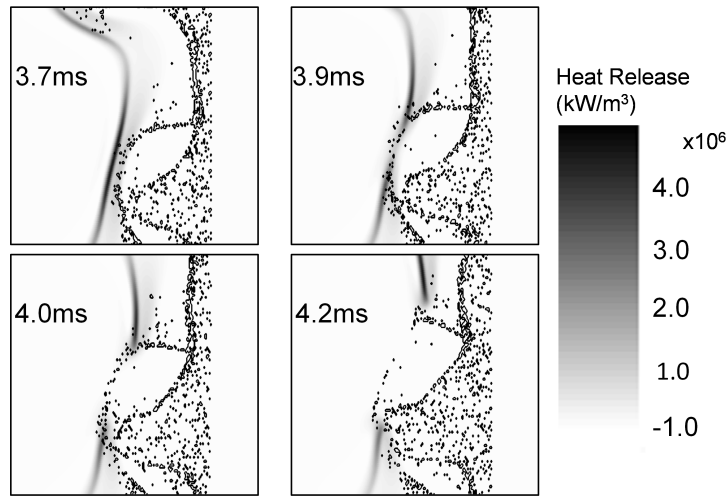
Figure 7.7: Temporal evolution of heat release rate isocontours for turbulent flame simulation with spray. The pictures correspond to the same region as those of Figure 7.5

.
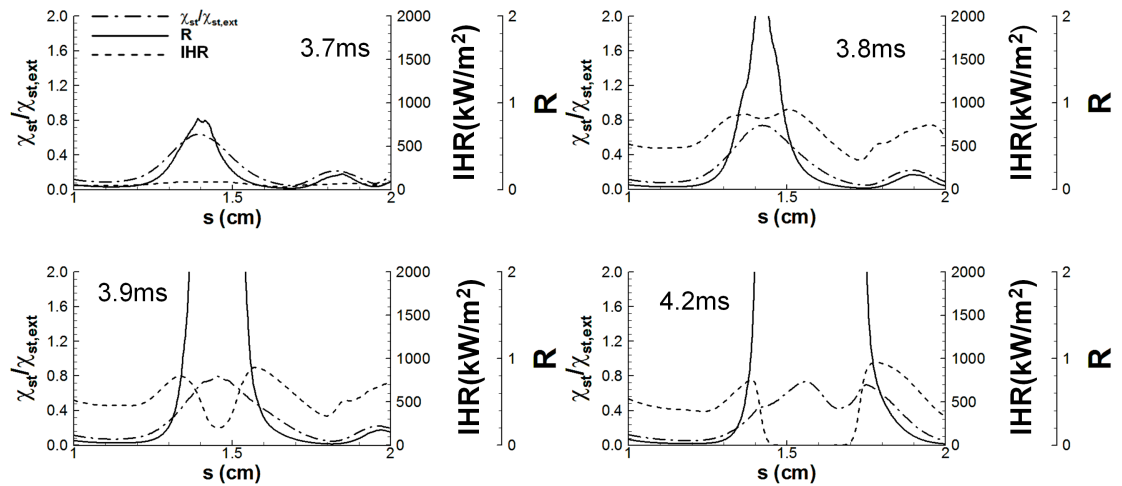
Figure 7.8: Distribution of the normalized scalar dissipation rate, integrated heat release rate (kW/m^2) and the weakness factor for the turbulent flames with spray at the four different times shown in Figure 7.7. The range of flame length shown here corresponds to that in Figure 7.6.
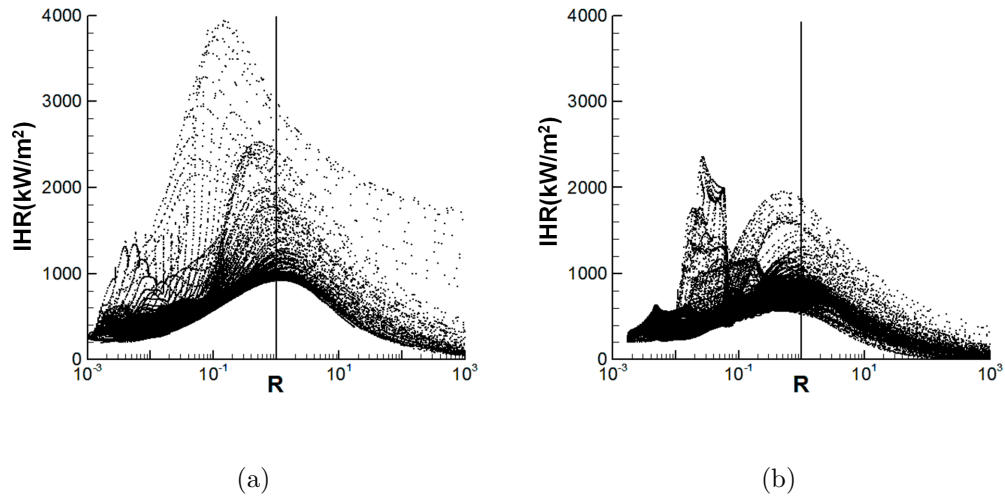
Figure 7.9: Integrated heat release rate (kW/m^2) versus weakness factor along the stoichiometric mixture fraction lines for cumulative data over the simulation time; (a) turbulent flames without spray (b) turbulent flames with spray. The vertical line denotes the $R = 1$ condition.

have finite heat release rate at R above extinction limit. This is a manifestation of transient flame dynamics; instantaneous snapshots of highly transient turbulent flames can show the weakening (and eventually extinguishing) flamelet segments as a combustion pocket at finite reaction rate. Note that the $R = 1$ criterion is still a valid metric to predict the local extinction event. However, the probability density of the local heat release rate distribution in highly turbulent flames may exhibit a more continuous spectrum in terms of the flame weakness factor.

7.4   Summary

Direct numerical simulations of 2D diffusion flames were conducted to investigate local extinction encountered in turbulent nonpremixed ethylene-air flames

interacting with fine water spray (Configuration C3). A unified extinction criterion is proposed to account for both strain-induced flame weakening and the flame cooling due to water droplet evaporation. In two dimensional laminar and turbulent flame cases under study, the proposed weakness factor R served as an excellent quantitative metric to detect local extinction events.

Two turbulent simulations, with and without spray injection, allowed direct comparison of two realistic turbulent flame quenching events by highlighting the additional flame weakening effects due to spray evaporation. Formation of edge flames was observed, and their subsequent evolution leading to the flame recovery or total extinction were found to depend strongly on the temporal history of the local strain rate as well as the presence of the spray droplets. The cumulative data for the local flame heat release rate versus the weakness factor showed two distinct regimes, the weak stretch regime in which the burning intensity increases with R and the extinction regime in which highly transient extinguishing flamelets exhibit lower yet finite heat release rate at R values significantly higher than unity. The large enhancement in the local heat release rates in some flame segments were attributed to the edge flame formation, which was significantly suppressed by the additional flame weakening in the presence of water spray.

Chapter 8

Conclusions and Future Work

8.1 Conclusions

The study has examined the extinction behavior of diffusion flames in three different non-adiabatic configurations: (C1) counterflow laminar flames with soot formation and thermal radiation transport; (C2) coflow turbulent flames with soot formation and thermal radiation transport; (C3) counterflow laminar and turbulent flames interacting with a mist-like water spray. The key findings are summarized below.

8.1.1 Key Findings

1. Configurations C1 and C2: The configuration C1 corresponds to extinction conditions that exhibit both fast and slow mixing limits in a laminar framework, while the configuration C2 exhibits extinction phenomena corresponding to the slow mixing limit in a turbulent framework. In both C1 and C2, the slow mixing limits show characteristic behavior -low temperatures and strong radiation effects. In configuration C1, it emerges that external soot loading increases the propensity of these flames to extinguish by bringing the kinetic and radiative limits closer (kinetic extinction occurs at a lower stretch rate, while the radiative extinction occurs at a higher stretch rate). In configuration

C2, the flames do not quench from radiative heat losses, but are significantly weakened. However, the stretch rates at which radiative weakening occurs is increased compared to soot free conditions.

2. Configuration C3: The configuration C3 corresponds to fast mixing conditions modulated by the level of water loading. These flames lose heat to liquid water droplets from evaporative cooling. For flames at a given stretch rate, there exists a critical water loading level above which extinction occurs. The work has also resulted in new insight being shed into the development of state relationships in a multiphase reacting framework. It was found that in the presence of an evaporating spray, the existing state relationships embodied in the classical mixing variable Z need to be modified to satisfy conservation equations.

3. On the extinction criterion: The extinction behavior of these non-adiabatic flames is investigated using an extinction criterion derived through AEA. It is seen that this criterion based on the Damköhler number describes extinction for all three configurations considered satisfactorily. However, in the turbulent flames in configuration C3, transient phenomena are seen for some of the flame elements, resulting in regimes where flames continue to burn in spite of being supercritical.

8.1.2   Key Contributions

The key contributions of this work are summarized below.

1. Validity of the Damköhler number based extinction criterion applied to non-adiabatic configurations: DNS is used to shed light into extinction phenomena in three different, and seemingly disparate extinction mechanisms, as seen in test configurations C1, C2 and C3, and presents them from a unified perspective in tying together extinction from stretch, radiative heat loss and evaporative cooling through a single Damköhler number that describes all these scenarios.

2. Development of AEA formulation for non-adiabatic configurations: Rigorous mathematical modeling techniques are used in developing a formulation to describe flame extinction in non-adiabatic configurations. The formulation includes the complete treatment of the radiation transport equation (both emission and absorption). This is an improvement over hitherto conducted investigations in that it allows the inclusion of non-local radiation absorption effects, and offers a means of including radiation absorption effects without resorting to the Optically Thin Model.

3. Modified mixture fraction and state-relationships in in flames interacting with evaporating water-spray: Based on an analysis of DNS data from Configuration C3, an improved formulation for mixture fraction and state relationships was developed and tested against data, enabling one to correctly interpret DNS data. The new state variables consist of an additional quantity called the spray-vapor fraction γ in addition to the classical mixture fraction Z. It is emphasized that not incorporating these improvements leads to an inaccurate

interpretation of the flame data.

8.2 Future Work

Several unanswered questions have arisen from the study, that need to be addressed.

8.2.1 Extinction Maps

The Damköhler number type relationships derived can be more attractively posed as extinction maps -a pictorial representation of the extinction scenario by gauging the extinction propensity of individual flame elements in two or three dimensional maps denoted by pertinent variables (for example, T_{st}, χ_{st}). It would be possible to estimate whether a point is extinguished pictorially by judging its state in relation to the extinction curve which would be the locus of all points constructed using T_{st} and χ_{st} obeying the Damköhler number based extinction criterion.

8.2.2 Demonstrating Kinetic and Radiative Extinction in Diluted Flames

It has been demonstrated in this work that external soot loading can bring about a significant reduction in the size of the flammable domain. In a similar vein, it is also of interest to know how dilution would affect the size of the flammable domain, when viewed alongside radiation heat losses. In practice, one would expect the the reactants (fuel/oxidizer) in environments such as compartment fires to be diluted,

and liable to quench from radiative extinction because of the reduction of the size off the flammable domain (i.e. low enough stretch rates may be achived even in normal gravity). DNS simulations are underway to demonstrate these ideas. Specifically, turbulent DNS simulations are now to be carried out with diluted reactants so that it may be possible to observe both kinetic and radiative extinction events to occur at stretching conditions that are moderate (i.e. one wants the radiative extinction limit to increase and the kinetic extinction limit to decrease).

Appendices

Appendix A

Mixture Fraction and State Relationships in Diffusion Flames Interacting with an Evaporating Water Spray

A.1   Introduction

Herein is considered an extension of the classical expressions for mixture fraction, coupling functions and state relationships to the case of diffusion flames interacting with an evaporating water spray (a model problem relevant to fire suppression studies). It is shown that the fuel-air-spray mixing processes may be described as a three-stream mixing problem parametrized in terms of the fractional mass that originates from the fuel stream (a mixture fraction variable) and the fractional mass that originates from the liquid water stream (a spray vapor mass fraction variable). One important outcome of the analysis is that the flame location (defined as the contour where fuel and air meet in stoichiometric proportions) is shifted due to the presence of the spray and in contrast to classical non-spray flames, does not correspond to a constant value of mixture fraction. The results of the analysis are tested against direct numerical simulation (DNS) data corresponding to two-dimensional laminar counter-flow diffusion flames interacting with a mist-like water spray. The DNS treatment includes a detailed chemical kinetic mechanism for ethylene-air combustion and unity Lewis numbers. The DNS data illustrate the change in flame structure associated with the presence of a water spray and support the validity of

the modified mixture fraction formulation.

Considered here are extensions to expressions of mixture fraction, coupling functions and state relationships to the case of diffusion flames interacting with an evaporating water spray. The study of the interactions of flames with water sprays has strong scientific and practical relevance, especially in fire suppression applications. Liquid-water-based fire suppression systems correspond to an established technology that is used today in many fire safety applications [31, 34]. It has long been known that the evaporative cooling power of liquid water is well-suited for its use as an extinguishing agent (at normal boiling conditions, the water latent heat of vaporization is equal to $\Delta H_v = 2.26$ MJ/kg, a value that is much higher than that found for any other non-flammable liquid). Current designs for water-based fire suppression protection use sprinklers or water mist systems for injection and atomization. Water mist systems use higher injection pressures (several tens of bars) and finer droplets (droplet sizes less than 100 μm) than those found in conventional sprinkler systems (a few bars of injection pressure and mean droplet diameters of order 1 mm). Sprinkler and mist systems achieve fire suppression by several mechanisms, e.g., by fuel cooling (i.e., by cooling the solid/liquid combustible material that provides fuel mass to the fire, and thereby by decreasing the fuel pyrolysis/evaporation rate), by flame spread inhibition (i.e., by pre-wetting adjacent virgin combustible surfaces), and by flame cooling (i.e., by direct interactions of the water spray with the laminar or turbulent flames).

We focus in the present chapter on the flame cooling mechanism and perform Direct Numerical Simulations of the interactions of fine mist-like evaporating water

139

droplets with an ethylene-air counter-flow diffusion flame. The scope of the present paper is limited to laminar flames (turbulent counterflow flame configurations are considered in chapter 7). Our objective is to define mixture fraction (and by the same token scalar dissipation rate), formulate coupling functions and state relationships, and identify flame location in the presence of a water spray.

A.2   Theory

The first step consists in treating the evaporating spray as a source of gaseous mass that is separate from the fuel and oxidizer supply streams. This leads to the description of the fuel-oxidizer-spray mixing process as a three-stream mixing problem, which may be viewed as a simple extension of the classical two-stream mixing problem described in textbooks. Let us consider a chemically conserved specific variable φ (i.e., a variable that is not produced or created during the combustion process, and a variable defined per unit mass of the gaseous mixture), we may write:

$$\varphi = \alpha \varphi_1 + \beta \varphi_2 + \gamma \varphi_3 \qquad (A.1)$$

where $\varphi_1, \varphi_2, \varphi_3$ designate the value taken by φ in the fuel stream, the oxidizer stream and the liquid water stream, respectively. In Equation (A.1), α, β, γ designate local gaseous mass fraction that originates from the fuel, oxidizer and liquid water streams respectively: $\alpha = 1$ in stream 1 (the fuel stream), and $\alpha = 0$ in streams 2 and 3; similarly $\beta = 1$ in stream 2 (the oxidizer stream), $\beta = 0$ in streams 1 and 3; $\gamma = 1$ in stream 3 (the liquid water stream) and $\gamma = 0$ in streams 1 and 2.

We have by definition

$$\alpha + \beta + \gamma = 1 \qquad \text{(A.2)}$$

and $\alpha = Z$, where Z is the conventionally used mixture fraction variable. One may then rewrite Equation (A.1) as

$$\varphi = Z\varphi_1 + (1 - Z - \gamma)\varphi_2 + \gamma\varphi_3 \qquad \text{(A.3)}$$

It is emphasized that while φ is a conserved variable, it does not necessarily satisfy a transport equation without a source term, owing to mass addition from the third stream

$$L(Z) = 0$$

$$L(1) = L(\gamma) = \dot{m}_w''' \qquad \text{(A.4)}$$

$$L(\varphi) = \dot{m}_w'''\varphi_3$$

where $\dot{m}_w'''$ is the water mass evaporation rate (defined per unit volume per unit time); L is the linear transport operator defined as

$$L(q) = \frac{\partial}{\partial t}(\rho q) + \frac{\partial}{\partial x_j}(\rho u_j q) - \frac{\partial}{\partial x_j}(\rho D \frac{\partial q}{\partial x_j}) \qquad \text{(A.5)}$$

where ρ is the mass density, u_j is the x_j-component of the flow velocity vector, and D the mass diffusivity (in what follows, we assume unity Lewis numbers and equidiffusive properties).

By applying Equation (A.3) to carbon, hydrogen, oxygen and nitrogen element

141

mass fractions, one obtains:

$$Y_C = ZY_{C,1}$$

$$Y_H = ZY_{H,1} + \gamma Y_{H,3}$$

$$Y_O = (1 - Z - \gamma)Y_{O,2} + \gamma Y_{O,3} \qquad \text{(A.6)}$$

$$Y_N = (1 - Z - \gamma)Y_{N,2}$$

where Y_k denotes the element k mass fraction. In Equation (A.6), it is assumed that: the fuel stream 1 has a chemical composition that can be represented by a $C_nH_mO_p$ molecule (no nitrogen); the oxidizer stream 2 is air (composed of oxygen and nitrogen); and the liquid in stream 3 is water. We have

$$Y_{C,1} = \frac{nM_C}{M_{C_nH_mO_p}}$$

$$Y_{H,1} = \frac{mM_H}{M_{C_nH_mO_p}}$$

$$Y_{O,1} = \frac{pM_O}{M_{C_nH_mO_p}}$$

$$Y_{O,2} = Y_{O_2,\text{air}} \qquad \text{(A.7)}$$

$$Y_{N,2} = Y_{N_2,\text{air}}$$

$$Y_{H,3} = \frac{2M_H}{M_{H_2O}}$$

$$Y_{O,3} = \frac{M_O}{M_{H_2O}}$$

where M_k is the molecular weight of species k, and $Y_{O_2,\text{air}}$ and $Y_{N_2,\text{air}}$ the mass fractions of oxygen and nitrogen in air (approximately 0.233 and 0.767, respectively).

The corresponding transport equations for the element mass fractions are

$$L(Y_\mathrm{C}) = 0$$

$$L(Y_\mathrm{H}) = 0$$

$$L(Y_\mathrm{O}) = 0 \tag{A.8}$$

$$L(Y_\mathrm{N}) = 0$$

Equation (A.3) suggests that the description of the flame structure requires at least two variables: the classical mixture fraction variable Z and a new spray vapor variable γ. As shown in the forthcoming section, these two variables provide a complete description of the flame structure in the limit of infinitely fast chemistry.

In the presence of evaporating water spray, γ takes positive values and Equation (A.6) shows that while the mixture fraction is linearly related to the carbon element mass fraction $Z = Y/Y_{\mathrm{C},1}$ such simple relationships do not hold for hydrogen, oxygen or nitrogen element mass fractions. Various coupling relationships may be formulated based on Equation (A.7); for instance, several equivalent expressions are available to calculate γ:

$$\gamma = \frac{Y_\mathrm{H}^+ - Y_\mathrm{C}^+}{Y_{\mathrm{H},1}/Y_{\mathrm{H},3}}$$

$$\gamma = 1 - Y_\mathrm{C}^+ - Y_\mathrm{N}^+ \tag{A.9}$$

$$\gamma = Y_\mathrm{C}^+ \frac{Y_{\mathrm{O},2} - Y_{\mathrm{O},1}}{Y_{\mathrm{O},3} - Y_{\mathrm{O},2}} - (1 - Y_\mathrm{O}^+)\frac{Y_{\mathrm{O},2}}{Y_{\mathrm{O},3} - Y_{\mathrm{O},2}}$$

where

$$Y_\mathrm{C}^+ = \frac{Y_\mathrm{C}}{Y_{\mathrm{C},1}}, \qquad Y_\mathrm{H}^+ = \frac{Y_\mathrm{H}}{Y_{\mathrm{H},1}}, \qquad Y_\mathrm{O}^+ = \frac{Y_\mathrm{O}}{Y_{\mathrm{O},2}}, \qquad Y_\mathrm{N}^+ = \frac{Y_\mathrm{N}}{Y_{\mathrm{N},2}} \tag{A.10}$$

We now turn to the question of the flame location. The flame location may be defined as the iso-surface where fuel and oxidizer meet in stoichiometric proportions.

Reference is made to Bilger [13] for a description. Simply put, the flame location may be determined by invoking the complete combustion assumption as follows.

The elemental mass fractions Y_C, Y_H and Y_O may be described in terms of species $Y_{C_nH_mO_p}$, Y_{O_2}, Y_{CO_2} and Y_{H_2O} as follows (it is assumed for the analysis that global combustion occurs-see Equation (A.15), consisting of only these species-the correctness of which assumption is tested and demonstrated in Section A.4)

$$Y_C = nY_{C_mH_mO_p}\frac{M_C}{M_{C_nH_mO_p}} + Y_{CO_2}\frac{M_C}{M_{CO_2}}$$

$$Y_H = mY_{C_nH_mO_p}\frac{M_H}{M_{C_nH_mO_p}} + 2Y_{H_2O}\frac{M_H}{M_{H_2O}} \tag{A.11}$$

$$Y_O = pY_{C_nH_mO_p}\frac{M_O}{M_{C_nH_mO_p}} + 2Y_{O_2}\frac{M_O}{M_{O_2}} + 2Y_{CO_2}\frac{M_O}{M_{CO_2}} + Y_{H_2O}\frac{M_O}{M_{H_2O}}$$

Upon setting $Y_{C_nH_mO_p} = Y_{O_2} = 0$ at the flame and eliminating Y_{CO_2} and Y_{H_2O} from the foregoing equations, one gets the following condition, which should be satisfied at the flame location.

$$\boxed{2\frac{Y_C}{M_C} + \frac{Y_H}{2M_H} - \frac{Y_O}{M_O} = 0} \tag{A.12}$$

Combining equation (A.6) and (A.12) one gets for the flame location

$$Z\left(\frac{2Y_{C,1}}{M_C} + \frac{Y_{H,1}}{2M_H} + \frac{Y_{O,2} - Y_{O,1}}{M_O}\right) - (1 - \gamma)\frac{Y_{O,2}}{M_O} = 0 \tag{A.13}$$

or

$$Z_{st} = (1 - \gamma_{st})\frac{\frac{Y_{O,2}}{M_O}}{\frac{2Y_{C,1}}{M_C} + \frac{Y_{H,1}}{2M_H} + \frac{Y_{O,2}-Y_{O,1}}{M_O}} \tag{A.14}$$

where Z_{st} and γ_{st} denote the values of the mixture fraction and spray vapor variables on the stoichiometric surface. Thus we find that in contrast to the non-spray case, the flame location in mixture fraction space is not constant and will depend on the

local amount of spray vapor. In addition, Equation (A.14) shows that increased amounts of spray vapor (i.e. larger values of γ_{st}) results in decreasing values of Z_{st}.

A.3 Burke-Schumann Flame Solution

We consider in this Section a simple application of the spray-modified mixture fraction formulation to a diffusion flame problem treated with a low-level chemistry model based on a global combustion equation. We start from the global step:

$$C_nH_mO_p + (n + \frac{m}{4} - \frac{p}{2})O_2 \rightarrow nCO_2 + \frac{m}{2}H_2O \tag{A.15}$$

where the list of chemical species in this model is limited to $C_nH_mO_p$ (also noted F in the following), O_2, CO_2, H_2O and N_2. Equation (A.6) may then be rewritten, after manipulations as follows

$$Y_F + \frac{Y_{CO_2}}{\eta_{CO_2}} = Z$$

$$Y_F + \frac{Y_{H_2O}}{\eta_{H_2O}} = Z + \frac{\gamma}{\eta_{H_2O}} \tag{A.16}$$

$$-r_sY_F + Y_{O_2} = -r_sZ + (1 - Z - \gamma)Y_{O_2,\text{air}}$$

$$Y_{N_2} = (1 - Z - \gamma)Y_{N_2,\text{air}}$$

where r_s, η_{CO_2}, η_{H_2O} are the stoichiometric oxygen-to-fuel, CO_2-to-fuel and H_2O-to-fuel mass ratios:

$$r_s = (n + \frac{m}{4} - \frac{p}{2})\frac{M_{O_2}}{M_{C_nH_mO_p}}$$

$$\eta_{CO_2} = n\frac{M_{CO_2}}{M_{C_nH_mO_p}} \tag{A.17}$$

$$\eta_{H_2O} = \frac{m}{2}\frac{M_{H_2O}}{M_{C_nH_mO_p}}$$

Equation (A.16) suggests that the reactive mixture composition may be obtained as a solution of 4 equations and 7 unknowns (5 species mass fractions, plus Z and γ). The mixture composition has therefore 3 degrees of freedom and may be parametrized in terms of the mixture fraction, the spray vapor variable and one reaction progress variable.

In the limit of inifinitely fast chemistry, an additional constraint is satisfied (fuel and oxidizer do not co-exist) and the mixture composition may then be expressed as follows: If $Z \leq Z_{st}$

$$Y_F = 0$$

$$Y_O = (1 - Z - \gamma)Y_{O_2,\text{air}} - r_s Z$$

$$Y_{CO_2} = \eta_{CO_2} Z \tag{A.18}$$

$$Y_{H_2O} = \eta_{H_2O} Z + \gamma$$

$$Y_{N_2} = (1 - Z - \gamma)Y_{N_2,\text{air}}$$

and if $Z > Z_{st}$

$$Y_F = Z - (1 - Z - \gamma)\frac{Y_{O_2,\text{air}}}{r_s}$$

$$Y_{O_2} = 0$$

$$Y_{CO_2} = \eta_{CO_2}(1 - Z - \gamma)\frac{Y_{O_2,\text{air}}}{r_s} \tag{A.19}$$

$$Y_{H_2O} = \eta_{H_2O}(1 - Z - \gamma)\frac{Y_{O_2,\text{air}}}{r_s}$$

$$Y_{N_2} = (1 - Z - \gamma)Y_{N_2,\text{air}}$$

Equations (A.18) and (A.19) are modified Burke-Schumann state relationships that account for the presence of a water spray. These state relationships now have

2 degrees of freedom and provide insight into the impact of the spray vapor variable γ on the flame structure.

A.4   Direct Numerical Simulation of Spray Modified Diffusion Flames With Finite Rate Chemistry

We now turn to an application of the spray-modified mixture fraction formulation to a diffusion flame problem treated with a finite rate, detailed chemistry model. We consider direct numerical simulations of steady, plane, laminar, counterflow flames, with ethylene as the fuel ($n = 2$, $m = 4$, $p = 0$) interacting with a water spray. To facilitate detailed comparisons with the previous analysis, the simulations were performed with unity Lewis numbers; the DNS solutions provide high-quality data that can then be used to test the predictions of Equations (A.6) and (A.14).

The DNS simulations are performed with the combustion solver S3D that has been used for some of the other studies in this work (Chapters 7). Combustion is described in the present study using a reduced chemical kinetic mechanism developed for ethylene-air mixtures [60, 55], the same mechanism used in Chapter 7-consisting of 19 species and 15 semi-global reactions, developed in [60].

The water spray is described using a classical Lagrangian-based method: the method tracks individual spherical-shaped droplets and includes two-way coupling between the gas and liquid phases, with a limitation to dilute conditions [109, 108], also used in Chapter 7, which uses the diagnostic improvements (for the mixture fraction) proposed herein.

The numerical configuration corresponds to a two-dimensional steady plane counter-flow flame at a strain rate of 440 s^{-1} (approximately 40% of the extinction strain-rate); the computational domain size is (1×2) cm^2 (Figure A.1). In Figure A.1 ethylene is injected at $x = -0.5$ cm (x is the flame-normal direction); air is injected at $x = 0.5$ cm; and the ethylene-air flame is stabilized in the vicinity of the stagnation plane, near $x = 0$. The grid spacing is uniform both in the x and y directions with $\Delta x \approx 16$ μm and $\Delta y \approx 25$ μm. Calculations are typically performed starting with an OPPDIFF solution [43] and using a time-marching approach until steady state is achieved.

Water droplets are injected on the air-side of the flame at a fixed x-location, $x_{ini} = 0.145$ cm. The injection scheme introduces droplets at randomly chosen discrete y-locations and at the local gas flow velocity. The spray is monodispersed with a droplet diameter of 10 μm, a value that is representative of conditions found in water mist systems). The injection scheme is stationary and corresponds to different values of the water loading aprameter WLP (defined as the ratio of the spray evaporative cooling power to the non-spray flame power): low values of WLP result in flame weakening, whereas high values result in flame quenching. While different cases were stimulated (see Chapter 7 for details), in the following, we limit our discussion to a case with WLP $\approx 20\%$.

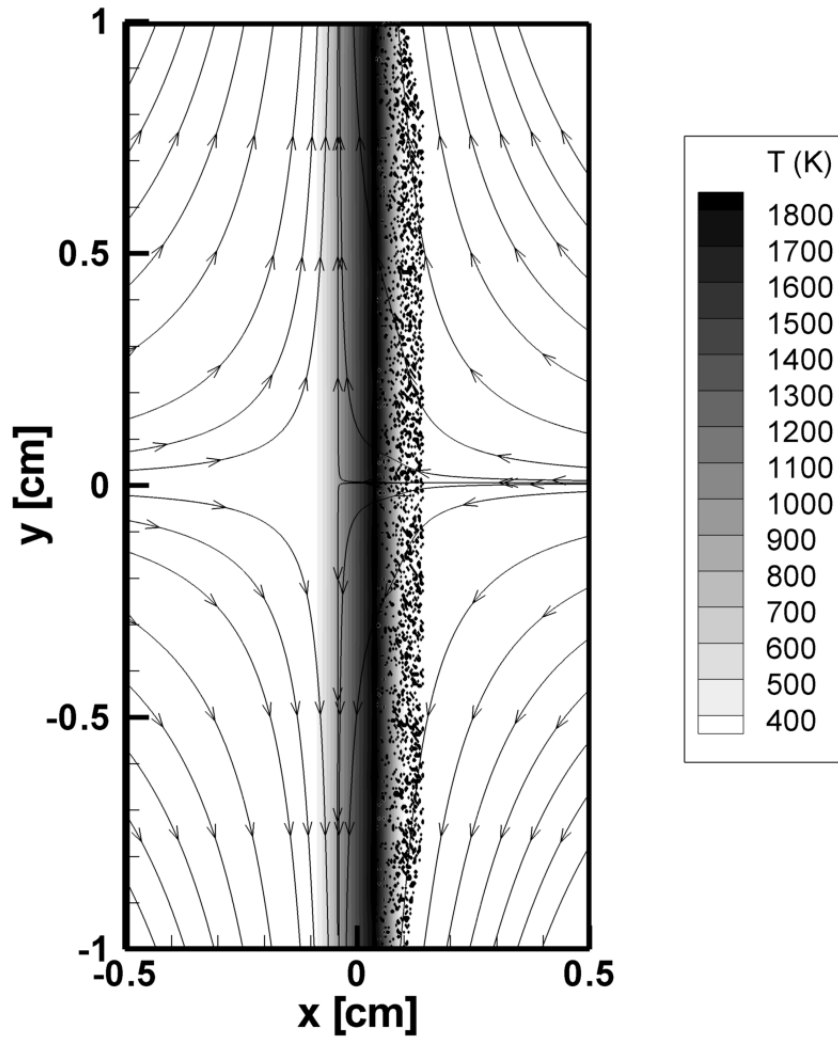Consistent with the previous discussion of Equation (A.6), we now define Z

Figure A.1: Laminar counterflow diffusion flame (ethylene is injected at $x = -0.5$ cm; air is injected at $x = 0.5$ cm). The plot shows selected flow streamlines and temperature iso-contours. The black dots at $0 \leq x \leq 0.145$ cm mark the location of the liquid water droplets.

and γ from the carbon and nitrogen element mass fractions:

$$Z = Y_{\mathrm{C}}^+$$

$$\gamma = 1 - Y_{\mathrm{C}}^+ - Y_{\mathrm{N}}^+$$

(A.20)

Using these relations, Equation (A.6) provides coupling relationships for hydrogen and oxygen mass fractions:

$$Y_{\mathrm{H}}^+ = Z + \gamma \frac{Y_{\mathrm{H},3}}{Y_{\mathrm{H},1}}$$

$$Y_{\mathrm{O}}^+ = 1 + Z \frac{Y_{\mathrm{O},1} - Y_{\mathrm{O},2}}{Y_{\mathrm{O},2}} + \gamma \frac{Y_{\mathrm{O},3} - Y_{\mathrm{O},2}}{Y_{\mathrm{O},2}}$$

(A.21)

Figure A.2 presents the spatial variations of mixture fraction Z and spray vapor variable γ along the flame normal. Consistent with the temperature variations presented in Figure A.1, the Z-variations suggest that the flame is approximately 0.2 cm thick. Also the γ-variations suggest that the spray vapor region corresponds to x-locations between -0.1 and 0.1 cm (note that the spray vapor mass remains small at the injection location because the gas temperature at x_{ini} is low - and close to ambient conditions - and the evaporative process, while already active, is comparitively slow).

Figure A.3 presents a numerical test of these coupling relations where and are evaluated either as H and O element mass fractions or from the Z and γ expressions found on the RHS of Equation (A.21). The scatter plot in Figure A.3 uses data from the entire field associated with one particular instantaneous snapshot of the DNS solution. The excellent agreement observed in Figure A.3 supports the validity of the analysis that led to Equation (A.6).

We now turn to the problem of finding the flame location. Consistent with
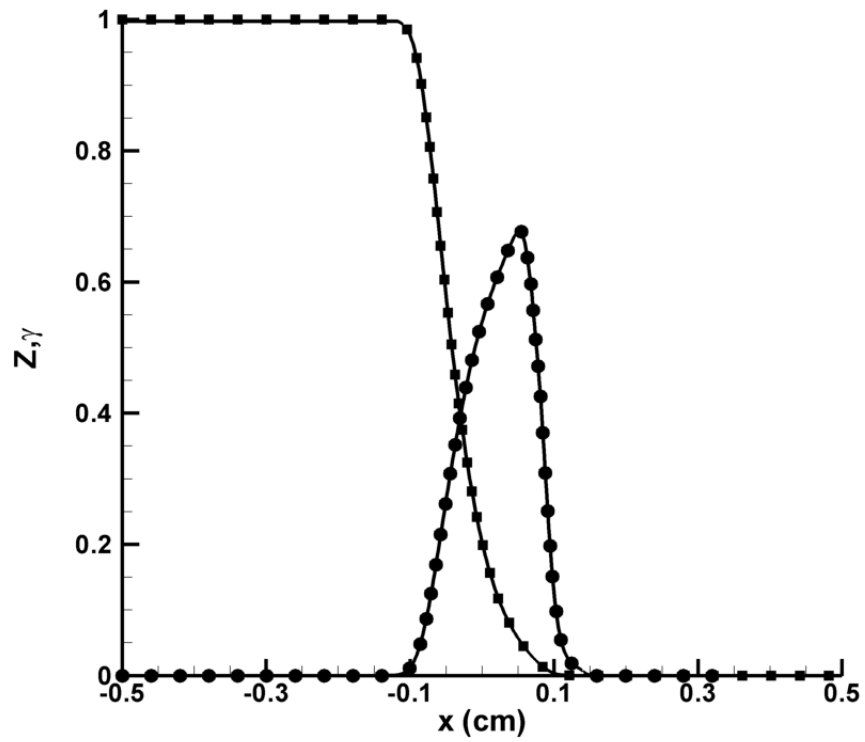
Figure A.2: Spatial variations of mixture fraction Z (squares) and spray vapor mass fraction γ (circles) along the flame normal direction. Values of γ are multiplied by a factor 10 to facilitate the graphical display.
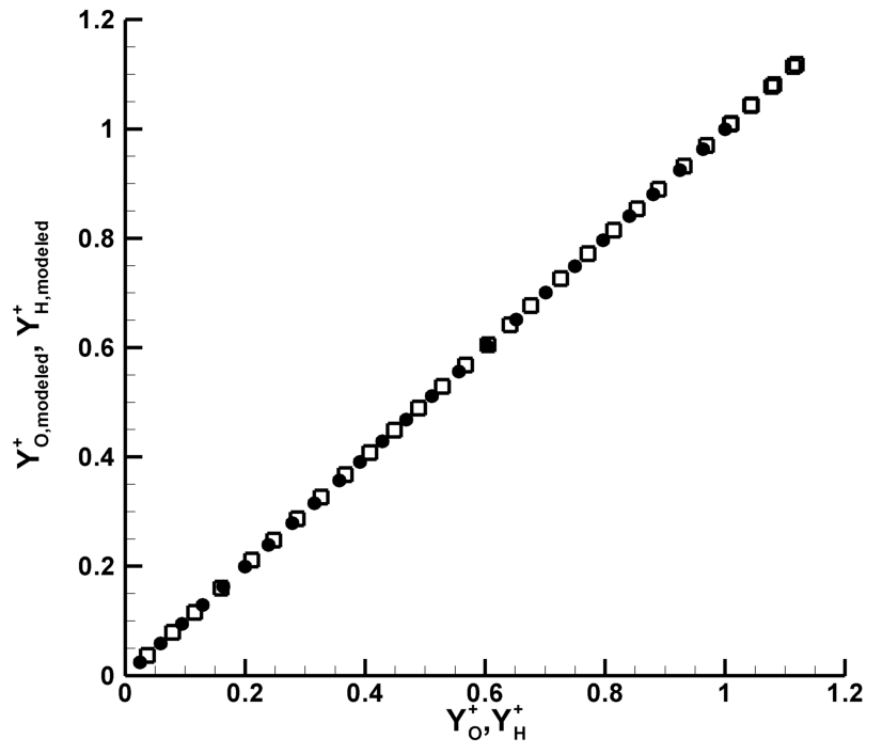
Figure A.3: DNS test of the spray-modified coupling relations presented in Equation (A.6): scatter plot showing (squares) and (solid circles) calculated from the RHS of Equation (A.21) versus the same quantities calculated as normalized hydrogen and oxygen element mass fractions.

the previous discussion of Equation (A.14), and following Bilger [13], we first post-process the DNS data and calculate the flame location as the loci of points where Equation (A.12) is satisfied. Once these points have been located, we interpolate and calculate different local quantities of interest, for instance the values of the mixture fraction and spray vapor variables Z_{st} and γ_{st}, as well as the flame temperature T_{st}. In the following, we compare these quantities to those produced by two different and incorrect methodologies: a first methodology, called M1, that calculates the flame location using a classical nitrogen-based mixture fraction expression that is not valid in the presence of a spray, $Z_{M1} = 1 - Y_{\mathrm{N}}^{+}$, and that assumes a constant value of mixture fraction at the flame location, $Z_{st,M1} = 0.064$; and a second methodology, called M2, that calculates the flame location using a valid carbon-based mixture fraction expression, $Z_{st,M2} = Y_{\mathrm{C}}^{+}$, but that incorrectly assumes a constant value of mixture fraction at the flame location, $Z_{st,M2} = 0.064$. Methodology M1 corresponds to a direct application of a non-spray formulation to a flame interacting with a water spray; methodology M2 corresponds to a hybrid formulation that uses a correct expression for mixture fraction but fails to recognize that the flame is no longer an iso-Z surface.

Figure A.4 presents the spatial variations of flame temperature T_{st} as a function of arc length along the flame contour. In Figure A.4, fluctuations in temperature are the result of the random variations in the droplet injection scheme and the subsequent variations in the spatio-temporal distribution of spray vapor mass. Furthermore, it is found that compared to a non-spray flame, the presence of the evaporating spray reduces the peak flame temperature by approximately 200 K:
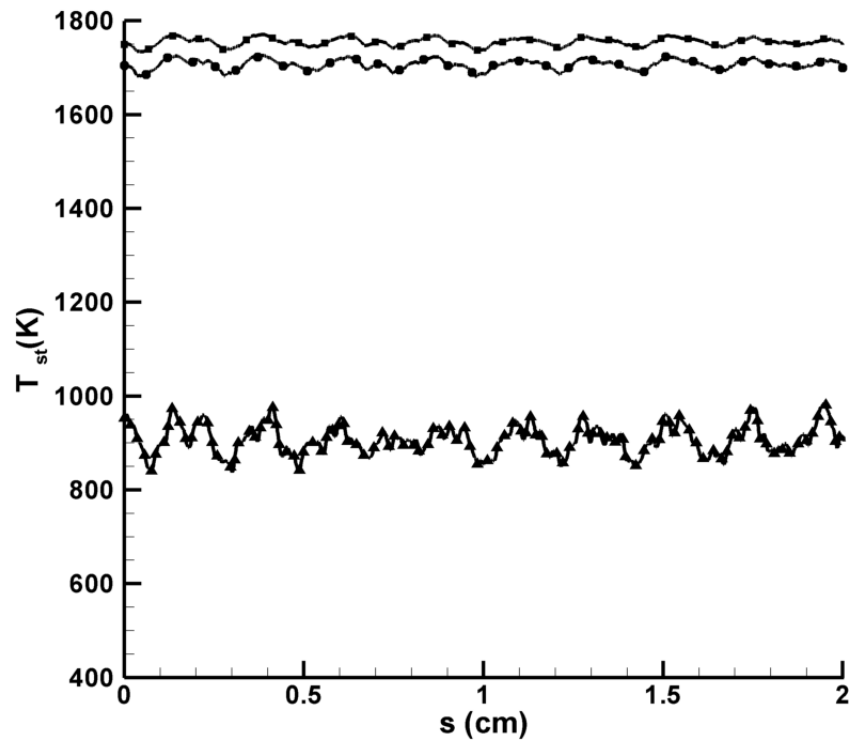
Figure A.4: Temperature variations as a function of arc length s measured along the stoichiometric contour. The lower (upper) curve corresponds to methodology M1 (M2); the middle curve corresponds to the methodology due to Bilger, see Equation (A.12).

the expected value of T_{st} is therefore in the range 1700-1800 K. It is clear from Figure A.4 that the M1 methodology leads to larger errors in the estimation of the flame temperature. These errors illustrate the importance of the modified formulation proposed above.

Figure A.5 presents similar flame-based variations for the mixture fraction Z_{st}. In the present configuration (WLP $\approx 20\%$), the values of γ_{st} are in the range of 6-7% and the shift in flame location in mixture fraction space corresponds to a decrease of the non-spray flame value by the same amount of 6-7%. Note that while in the present case, this shift remains small, Equation (A.14) predicts that configurations with higher water loading will result in larger amounts of spray vapor mass and more pronounced effects.

A.5   Summary

A three-stream mixing analysis is proposed in this study to describe mixture fraction, coupling functions and state relationships in the case of diffusion flames interacting with an evaporating water spray. The resulting description shows that: the flame structure depends on a spray vapor mass fraction variable; classical expressions for mixture fraction may no longer hold; the flame location is shifted in mixture fraction space.

DNS is then used to test the proposed modified mixture fraction formulation. The DNS configuration corresponds to steady, two-dimensional, plane, laminar, counter-flow, ethylene-air diffusion flames interacting with a mist-like water
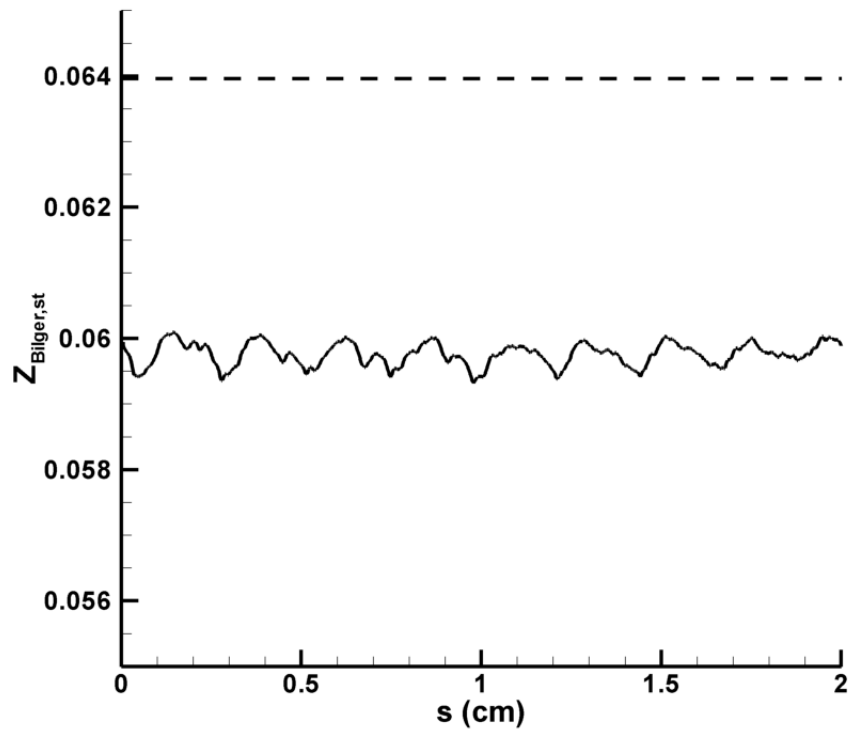
Figure A.5: Mixture fraction variations as a function of arc length s measured along the stoichio-metric contour. The lower curve corresponds to the methodology of Bilger, see Equation (A.14); the upper curve corresponds to methodology M2.

spray (Configuration C3). The DNS treatment includes a detailed chemical kinetic mechanism and unity Lewis numbers. The DNS data support the validity of the modified mixture fraction formulation and also emphasize the large errors that may result from ignoring the change in flame structure due to the presence of the spray.

Appendix B

Validation of Flame Structure Calculations in AEA and DNS

B.1 Flame Structure With Soot

In this appendix, a cross-validation study between AEA and DNS is carried out. A Laminar counterflow flame particular stretch-rate is considered (Configuration C1), and partinent quantities (temperature, species mass fractions, velocities and quantities pertaining to soot) are compared, and the reasons for the discrepancies are explained.

The simulations use $C_{soot} = 700$ m^{-1}K^{-1} to modulate the soot aborption coefficient in Equation (3.48). The comparisons are made for a stretch rate of $\chi_{st} = 6$ s^{-1}. In addition, the calculations test different matching conditions for outer and inner solutions, $Z_{st,+} = (0.08, 0.15)$ (Section 3.98) which has significance in soot production owing to the stiffness of the source terms, as shall be explained.

Figure B.1 shows the flame temperature comparison between AEA and DNS, showing that the flame temperatures compare excellently in both cases. Figure B.2 presents the structure of the scalar dissipation rate. Here, whilst the differences are negligible at the flame ($Z = 0.064$), there is a difference of about 20 % at the locations of peak scalar dissipation rate. These may be attributed to the use of $\rho^2 D = constant$ in the AEA formulation. Figure B.3 presents a comparison of the x-velocity between AEA and DNS.

Figure B.1: Comparison between AEA and DNS flame temperatures, with $\chi_{st} = 6$ s^{-1}, and the matching condition for the mixture fraction $Z_{st,+} = 0.15$. Solid lines denote DNS data, while dashed lines denote AEA data.

Figure B.2: Comparison between AEA and DNS scalar dissipation rates, with $\chi_{st} = 6 \text{ s}^{-1}$, and the matching condition for the mixture fraction $Z_{st,+} = 0.15$. Solid lines denote DNS data, while dashed lines denote AEA data.
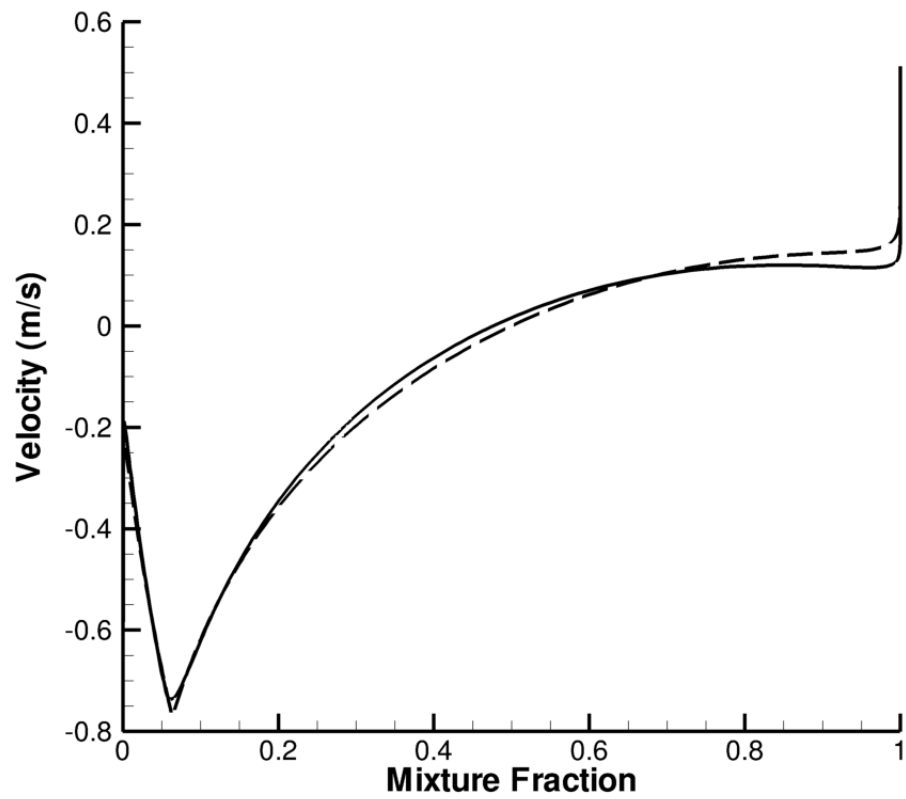
Figure B.3: Comparison between AEA and DNS x-direction velocities, with $\chi_{st} = 6$ s^{-1}, and the matching condition for the mixture fraction $Z_{st,+} = 0.15$. Solid lines denote DNS data, while dashed lines denote AEA data.
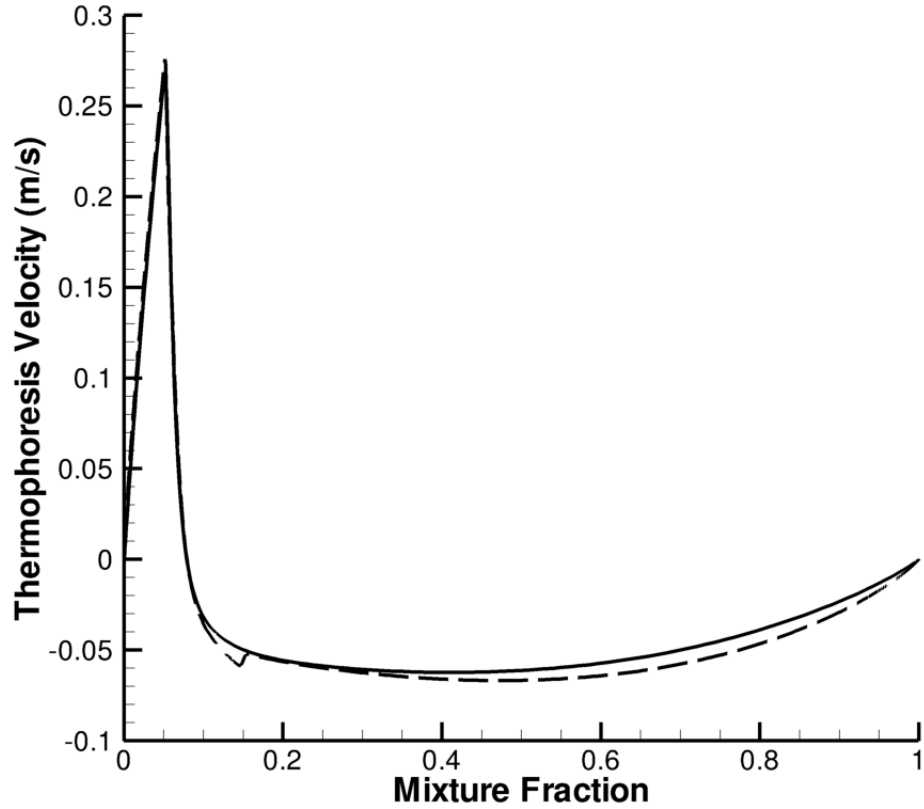
Figure B.4: Comparison between AEA and DNS x-direction thermophoretic velocities, with $\chi_{st} = 6$ s^{-1}, and the matching condition for the mixture fraction $Z_{st,+} = 0.15$. Solid lines denote DNS data, while dashed lines denote AEA data.

B.1.1   Comparison of Quantities Pertaining to Soot

Figure B.4 presents a favorable comparison between thermophoretic velocities between DNS and AEA. The soot number density N_s and soot mass fraction Y_s are compared in Figures B.5 and B.6 respectively. The interpretation from these figures is that while the overall picture compares reasonably well there are some discrepancies in the peak soot mass fractions, which differ by about 20 %, for which explanations are warranted.   An analysis of the source terms reveals that some of
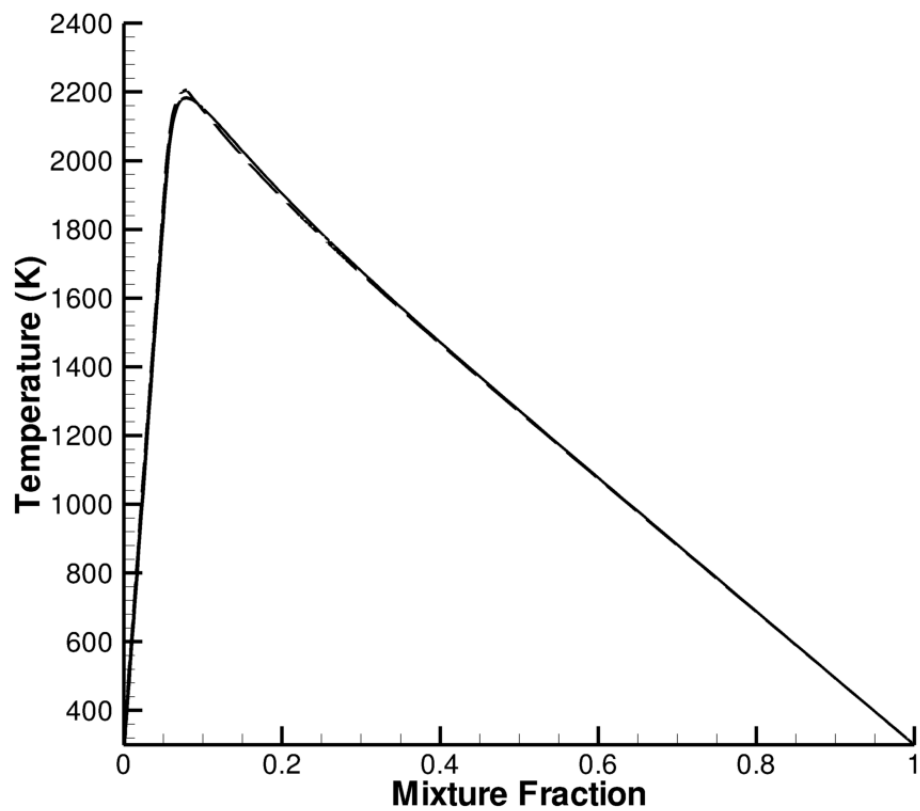
Figure B.5: Comparison between AEA and DNS soot number density, with $\chi_{st} = 6$ s^{-1}, and the matching condition for the mixture fraction $Z_{st,+} = 0.15$. Solid lines denote DNS data, while dashed lines denote AEA data.
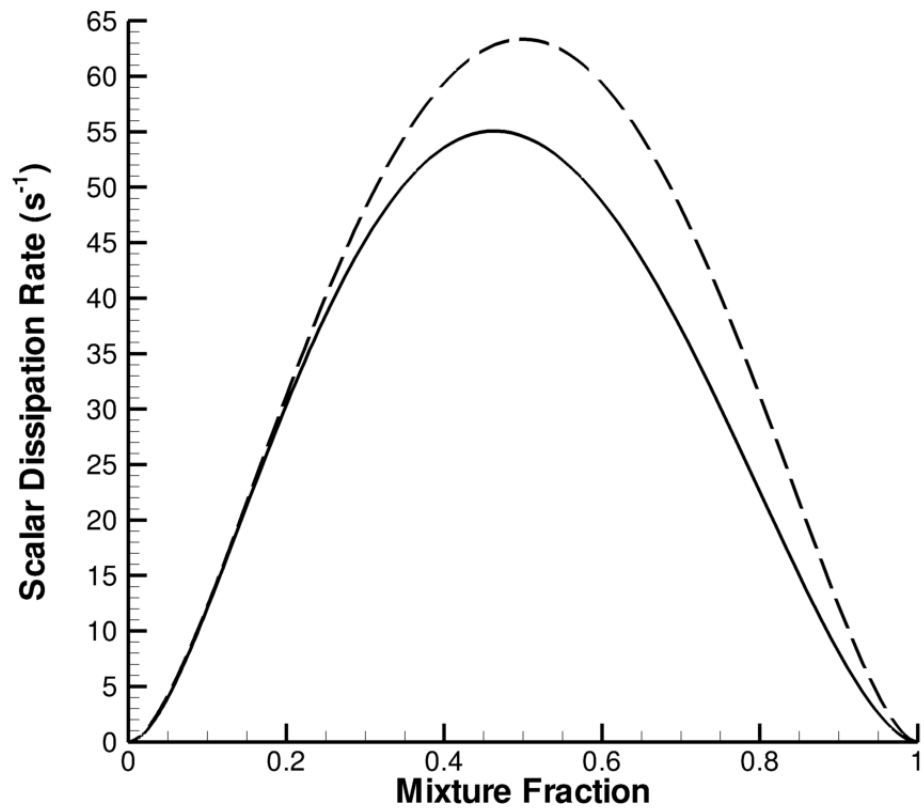
Figure B.6: Comparison between AEA and DNS soot mass fractions, with $\chi_{st} = 6$ s^{-1}, and the matching condition for the mixture fraction $Z_{st,+} = 0.15$. Solid lines denote DNS data, while dashed lines denote AEA data.
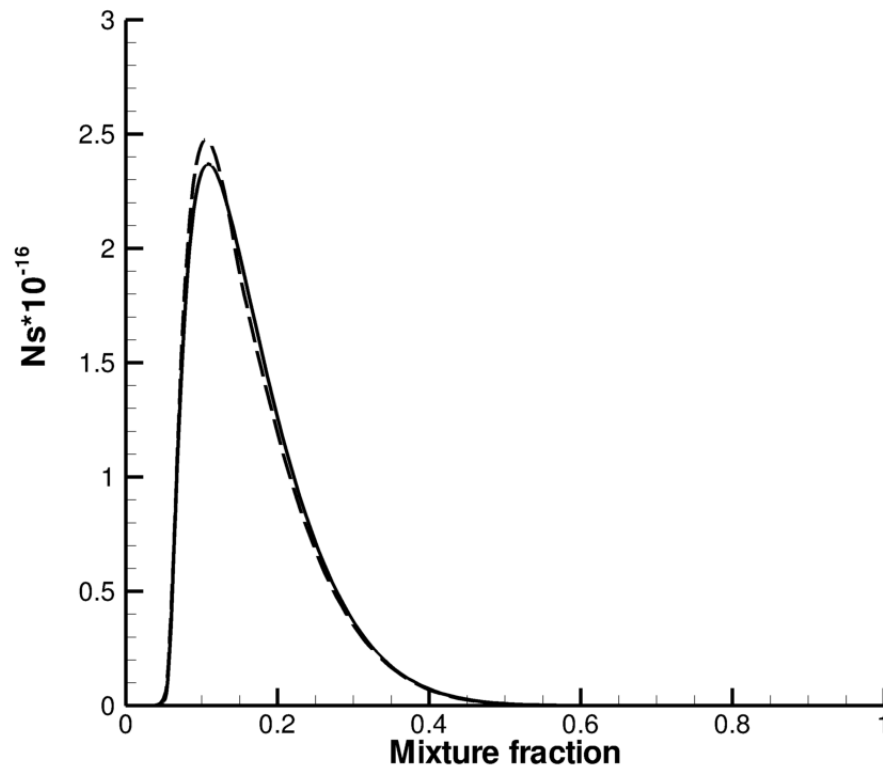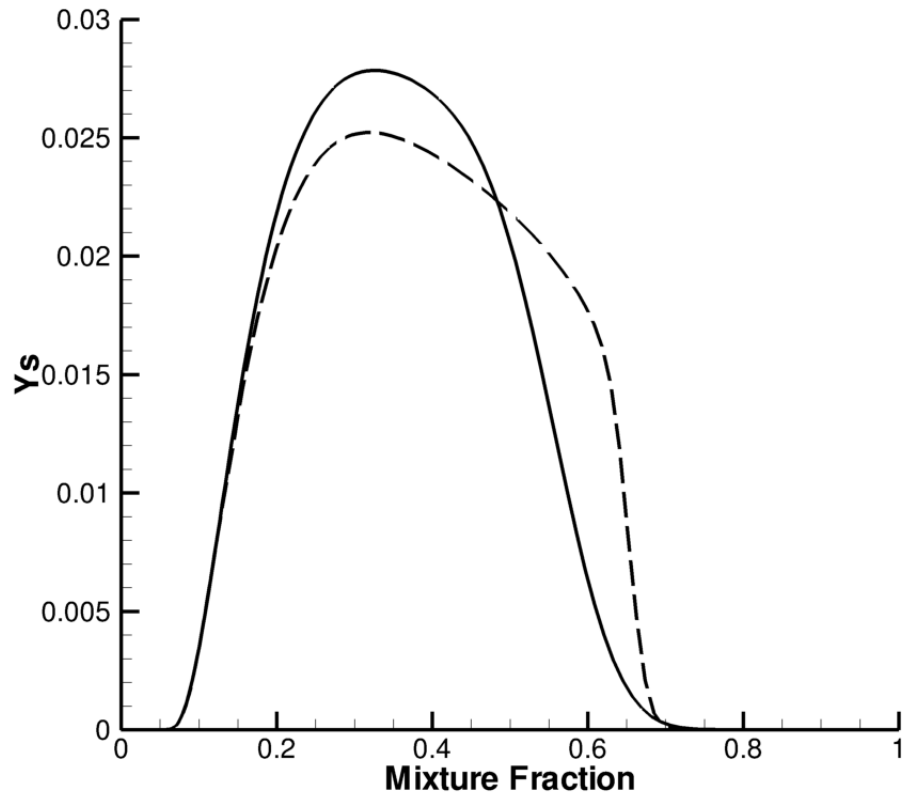
the discrepancies may be attributed to the specification of the mixture fraction used in matching the outer and inner solutions, which has a bearing in the solution of the soot equations by affecting the source terms (it is apparent that since the velocities compare extremely well, the discrepancies have to arise in the source terms). The source terms are stiff, and depend on the fuel and oxidizer mole fractions, as seen in Equations (2.18) and (2.19). Notably, these quantities are fairly negligible in the vicinity of the flame zone, but the stiffness of the source terms implies that they still affect the solution significantly, and thus need to be calculated accurately.

To bring this into perspective, the mole-fraction profiles are presented in Figure B.7 (in connection with Equations (2.18) and (2.19)) in which AEA comparison is made with DNS data for the two different matching conditions of the mixture fraction $Z_{st,+} = (0.08, 0.15)$. The plot has been presented in log-scale in order to more closely observe the values at the stoichiometric location $Z_{st} = 0.064$. While the comparison is good overall, the oxygen concentrations are more accurately reproduced for $Z_{st,+} = 0.15$ than with $Z_{st,+} = 0.08$. Pertinently, $Z_{st,+} = 0.08$ results in a *larger* oxygen concentration, which therefore leads to an increased soot oxidation rate. The soot oxidation rate presented in Figure B.8 highlights this point. Specifying $Z_{st,+} = 0.08$ results in a large overestimate of the soot oxidation term, leading to an underestimate of the soot mass fraction, in Figure B.9. It is seen that the other source terms are less significantly affected, in Figures B.10 and B.11. However, even with these differences, we deem that the comparison is reasonably favorable.
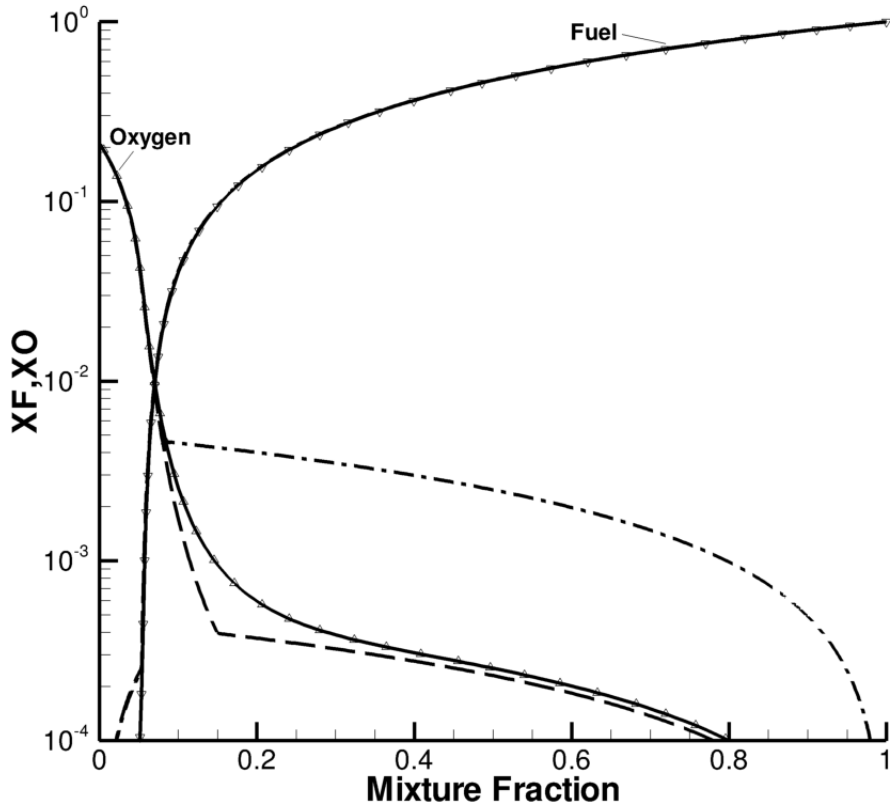
Figure B.7: Comparison between AEA and DNS fuel and oxidizer mole fractions, with $\chi_{st} = 6 \, \text{s}^{-1}$. Solid lines denote DNS data, dash-dotted lines denote AEA data with the matching condition for the mixture condition specified as $Z_{st,+} = 0.08$, and dashed lines denote AEA data with $Z_{st,+} = 0.15$.
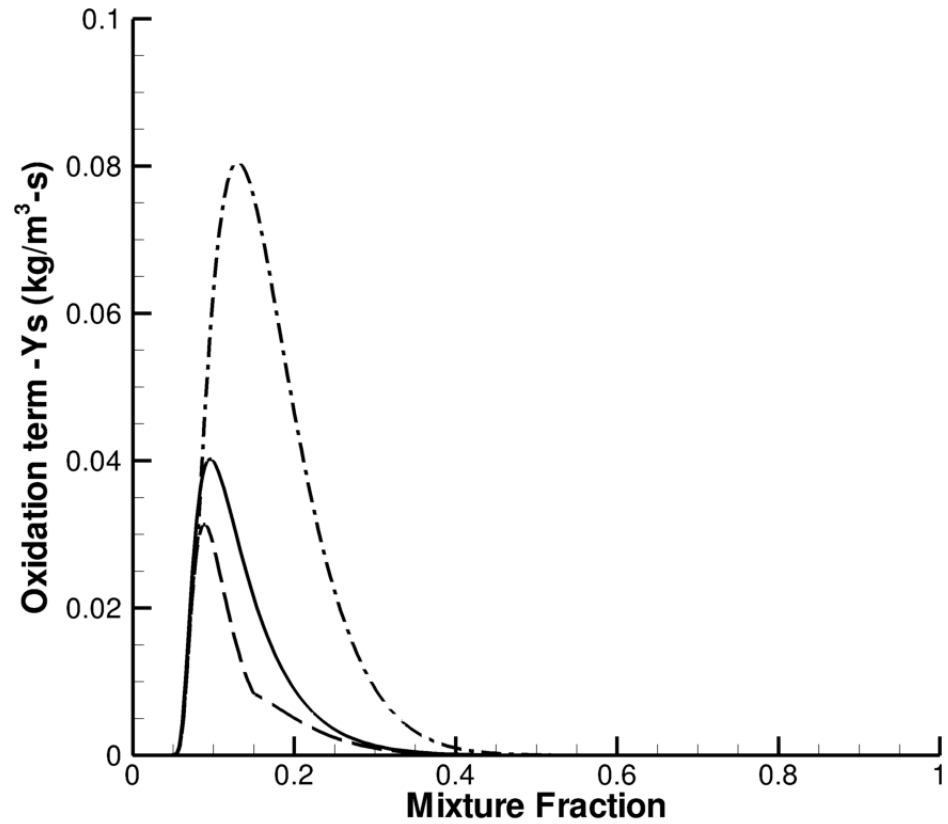
Figure B.8: Comparison between AEA and DNS soot oxidation terms, with $\chi_{st} = 6 \text{ s}^{-1}$. Solid lines denote DNS data, dash-dotted lines denote AEA data with the matching condition for the mixture fraction specified as $Z_{st,+} = 0.08$, and dashed lines denote AEA data with $Z_{st,+} = 0.15$.
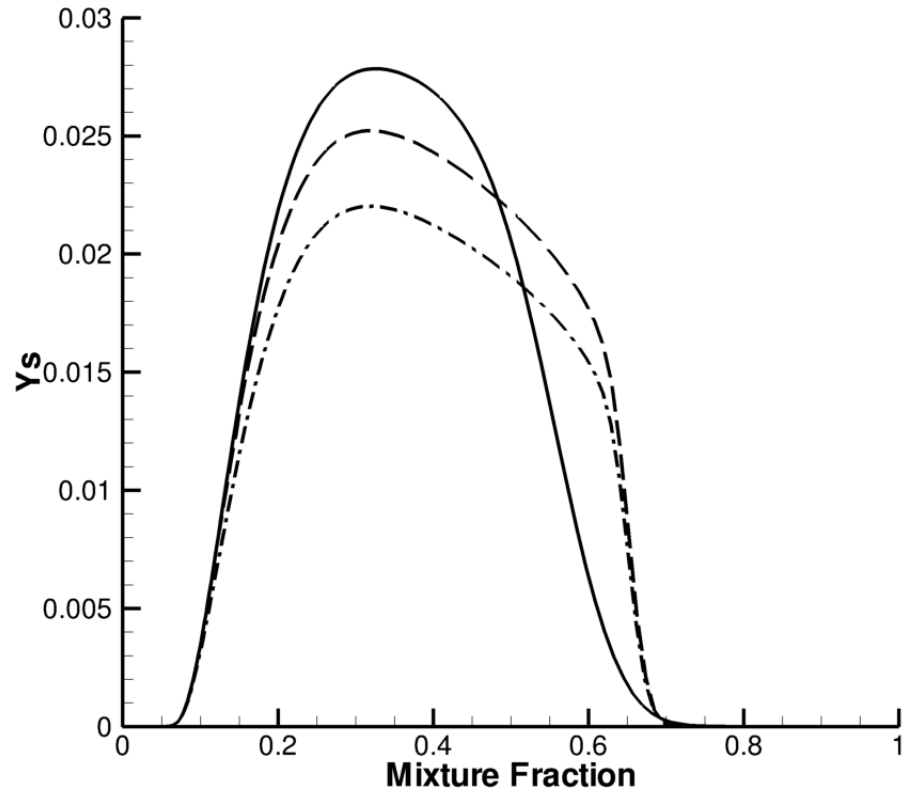
Figure B.9: Comparison between AEA and DNS soot mass fractions, with $\chi_{st} = 6 \text{ s}^{-1}$. Solid lines denote DNS data, dash-dotted lines denote AEA data with the matching condition for the mixture fraction specified as $Z_{st,+} = 0.08$, and dashed lines denote AEA data with $Z_{st,+} = 0.15$

.
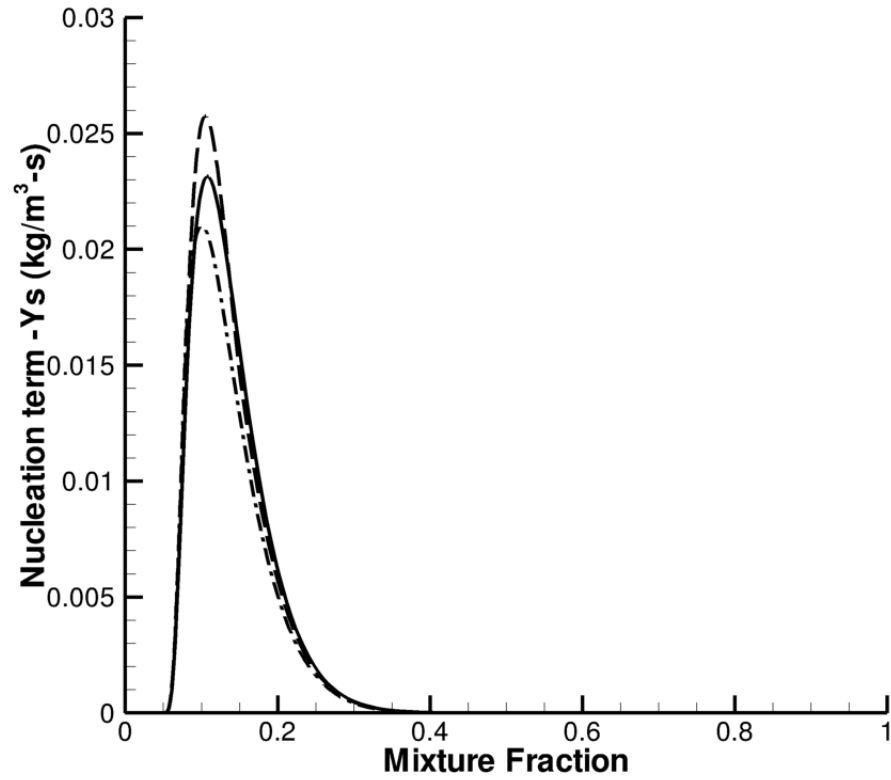
Figure B.10: Comparison between AEA and DNS soot nucleation terms appearing in Equation (2.16), with $\chi_{st} = 6$ s^{-1}. Solid lines denote DNS data, dash-dotted lines denote AEA data with the matching condition for the mixture condition specified as $Z_{st,+} = 0.08$, and dashed lines denote AEA data with $Z_{st,+} = 0.15$.
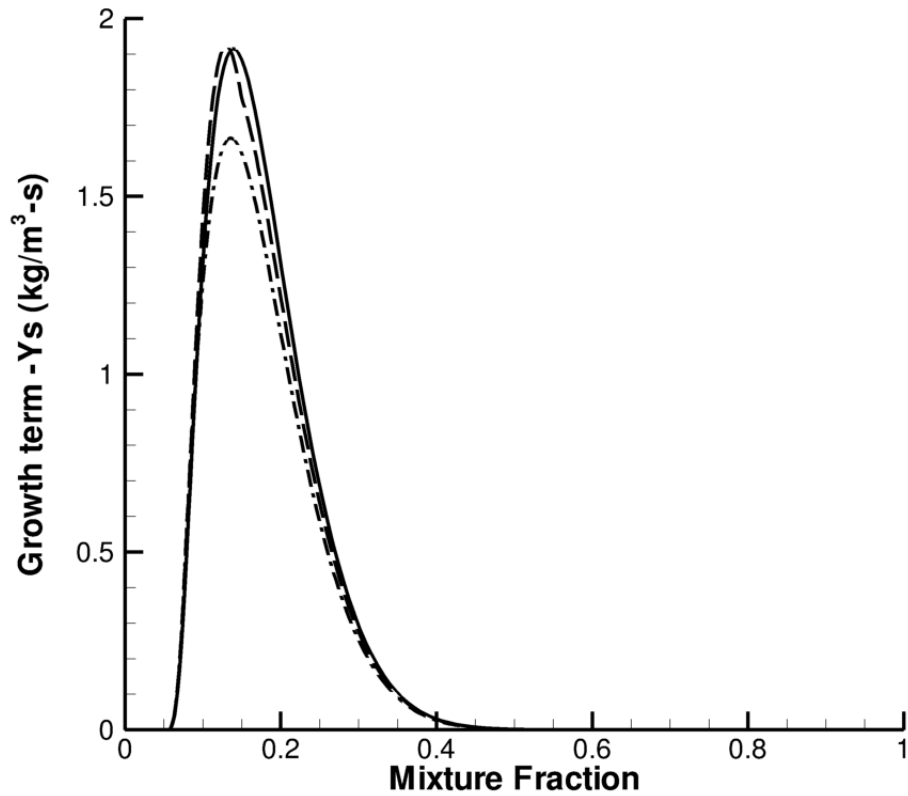
Figure B.11: Comparison between AEA and DNS soot growth terms appearing in Equation (2.16), with $\chi_{st} = 6 \text{ s}^{-1}$. Solid lines denote DNS data, dash-dotted lines denote AEA data with the matching condition for the mixture fraction specified as $Z_{st,+} = 0.08$, and dashed lines denote AEA data with $Z_{st,+} = 0.15$.

B.2 Summary

Successful cross validation tests have been carried out between AEA and DNS for a laminar counterflow flame at a stretch rate of $\chi_{st} = 6$ s^{-1} (Configuration C1). The flame structure was compared to examine pertinent quantities -flame temperature, scalar dissipation rate, species profiles and soot. Of these, some discrepancies are observed in the scalar dissipation rate and soot profiles. For the scalar dissipation rate, the differences may be attributed to the assumption of $\rho^2 D = constant$. As for soot, a further examination of the source terms appearing in the soot transport equations reveal that owing to the stiff nature of these terms, a highly accurate description of the species concentrations is needed (which, to leading order vanish at the flame), and are affected by the matching conditions specified. However, aside from these differences, the comparison is to be considered favorable insofar as the reproduction of the peak soot yield and the qualitative picture are concerned.

Appendix C

Validation Tests for DNS Spray Solver

This chapter presents validation tests for the DNS spray solver in order to test satisfaction of global conservation laws. Tests on the conservation of mass and energy, and the d^2 law for droplet evaporation are conducted. Using the conservation of total mass and energy for the combined gas-droplet system, the mass and energies for the both phases are monitored, as is their sum. The square of the droplet radius is also examined to show that the droplet model obeys the d^2 law.

Two parametric case studies are considered, corresponding to droplet diameters of $(10, 20)$ μm, with a grid spacing chosen as 12 μm so as to have one case where the droplet is smaller than the grid cell size (for the 10 μm droplet) and another where it is larger (for the 20 μm droplet). The flow conditions are quiescent, with zero gas velocity and a *single* stationary droplet at 340 K is injected at the center of a two dimensional domain containing air at 1000 K. The heat from the ambient gas is allowed to evaporate the droplet to completion. The mass and energy of this droplet-gas system are monitored for consistency to satisfy global conservation laws.

C.1   Mass Balance

From mass conservation, it may be recognized that

1. The total mass of the system is conserved.

2. The total water-mass of the system is conserved

Both conservation statements must be satisfied, and may be stated as follows. For total mass balance

$$m_g + m_{liq} = constant \qquad (C.1)$$

where m_g is the mass of the gas phase and m_{liq} is the mass of the liquid phase. The mass of the gas phase m_g is calculated as

$$m_g = \Delta z \int_{x,y} \rho \mathrm{d}x\mathrm{d}y \qquad (C.2)$$

where ρ is the density of the gas phase, and the integration is carried out over the two dimensional domain (x, y). Formally, the spanwise direction z also figures in the above equation, though the simulation itself is carried out in two dimensions.

The liquid-phase mass m_{liq} is calculated by summing up the individual droplet masses, which in this case is for only one droplet, and may be obtained from the radius of the droplet r_d and the density of the droplet ρ_d. For a system with n_d droplets one has

$$m_{liq} = \sum_{n_d} m_d = \sum_{n_d} \frac{4}{3}\pi r_d^3 \rho_d \qquad (C.3)$$

Alternatively, for water mass one may write

$$m_w^l + m_w^g = constant \qquad (C.4)$$

where m_w^l is the water mass in the liquid phase, and m_w^g is the water-mass in the gas phase. It may be noted that in this case, $m_w^l = m_{liq}$. Furthermore, the water mass in the gas phase is obtained by integrating the gaseous water mass-density over the

domain

$$m_w^g = \Delta z \int_{x,y} \rho Y_w \mathrm{d}x\mathrm{d}y \tag{C.5}$$

where Y_w is the mass fraction of water in the gas-phase.

Although both mass conservation equations stated in the foregoing are equivalent, in the current disgnostics only the water mass conservation in Equation (C.4) is presented because of observational convenience (as there is no water mass present initially in the gas phase, it is easier to demonstrate int he water-mass diagnostic that all the water present initially in the liquid phase is transferred to the gas phase subsequent to evaporation).

C.2   Energy Balance

The total energy of the droplet+gas system should be conserved. The diagnostic therefore tracks the energy of each individual phase over time during the course of the droplet's lifetime.

$$H_g + H_{liq} = constant \tag{C.6}$$

where H_g is the total gas phase energy given by

$$H_g = \Delta z \int_{x,y} \rho h \mathrm{d}x\mathrm{d}y \tag{C.7}$$

where he is the gas-phase enthalpy per unit volume, expressed as a combination of the gaseous sensible heat $\int c_p \mathrm{d}T$ and the gaseous enthalpy of formation h_k^0, summed over for each individual species, weighted by the species mass fraction Y_k.

$$h = \sum_k (h_k^0 + \int_{T_0}^{T} c_{p,k}\mathrm{d}T)Y_k \tag{C.8}$$

174

For the liquid phase, one only monitors the enthalpy of the individual droplet, obtained as

$$H_d = \sum_{n_d} m_d (h_w^0 + \int_{T_0}^{T_d} c_{p,w}(T)\mathrm{d}T) \tag{C.9}$$

where T_d is the temperature of an individual droplet, h_w^0, and $c_{p,w}$ are the enthalpy of formation of liquid water and the specific heat of liquid water respectively.

C.3 The d^2 Law

The square of the droplet radius is monitored over the droplet's lifetime to test weather the d^2 law holds, in which case, the square of the droplet will decrease linearly with time during evaporation [47], giving an estimate of the droplet's lifetime.

$$r_d^2 = r_{0,d}^2 - Kt \tag{C.10}$$

where $r_{0,d}$ is the initial droplet radius and K is a constant of proportionality determining the droplet's lifetime.

C.4 Simulation Parameters

1. Domain size: $(L_x, L_y = (480, 480)$ μm $= (0.048, 0.048)$ cm.

2. Grid resolution: 40×40 grid points in (x, y) or a resolution of $(12, 12)$ μm in the x and y directions. While a 12 μm resolution is higher then the simulated turbulent flame resolution of 16 μm (Chapter 7), it was chosen for two reasons

   (a) To reduce the energy contained in the gas phase vis-à-vis the energy of

the droplet phase so that they may be compared more easily.

(b) A 12 μm resolution may be *perceived* as more stringent than a 16 μm resolution with regard to the performance of the droplet solver, because the droplet solver is expected to perform better when the ratio of the droplet to grid size is small [109]. However, as will be seen from the current tests, in the range of droplet sizes considered, the issue does not play a significant role.

3. Gas-phase composition and pressure: Pure air at 1 atm pressure

4. Droplet size:

   (a) Test 1: $d_d = 10$ μm (droplet diameter, smaller than the grid cell of 12 μm)

   (b) Test 2: $d_d = 20$ μm (droplet diameter, larger than grid cell of 12 μm)

5. Temperatures:

   (a) Gas-phase temperature: 100 K

   (b) Droplet temperature: 340 K

6. Velocities:

   (a) Flow velocity is zero (quiescent)

   (b) Droplet velocity is zero (stationary droplet)

7. Number of droplets injected: 1

8. Droplet injection position: at the center of the box of dimensions $(0.048, 0.048)$ cm

9. Boundary conditions: periodic, to ensure that there is no loss of gaseous mass, momentum or energy through the boundaries

10. Number of processors: 4, the simulations being carried out in Franklin, NERSC

11. The droplet is destroyed when the size falls to 1 μm. This condition is set in the code

C.5 Results

C.5.1 Test Case 1: $r_d = 5$ μm (or $d_d = 10$ μm)

In Figures C.1 and C.2 are plotted the system's mass and energy respectively to demonstrate the conservation of these quantities, while in Figure C.3, the d^2 law is demonstrated. Figure C.4 shows a picture of the two dimensional temperature field for the gas-phase. In Figure C.1, the masses of the droplet and gas phases and their sum are monitored over the course of the droplet's lifetime (1 ms). The total mass of the system remains constant, demonstrating that mass conservation is satisfied for the 10 μm droplet.

In Figure C.2, the energies of the droplet and gas phases, and the total energy of the system obtained by summing them are plotted over the course of the droplet's lifetime (1 ms). The total energy remains nearly constant, to a tenth of a percentage, thus demonstrating that energy conservation is satisfied for the 10 μm droplet.

In Figure C.3, the d^2 law is tested by plotting the square of the droplet's radius, versus time. The behavior of this curve is linear, demonstrating that the droplet
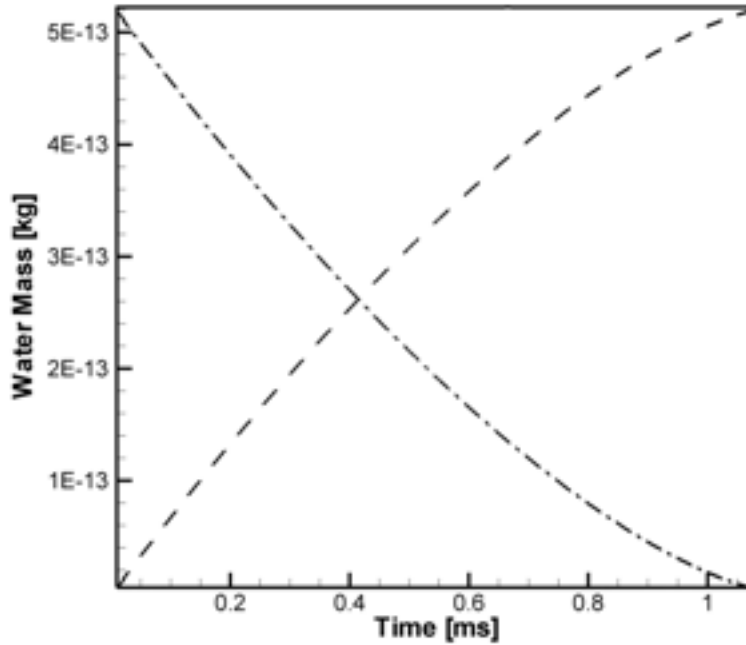
Figure C.1: Conservation of water mass in the system (droplet diameter 10μm). The solid black curve is the total water mass in the system, expressed as the sum of the liquid water mass (dashed-dotted lines) and the gas phase water mass (dashed). The total water mass in the system remains nearly constant over the course of the droplet's lifetime (1 ms) .

model obeys the d^2 law. An additional comment is to be made regarding the size at which the droplet is destroyed, which is set in the solver to be at a radius 1μm. It is therefore seen that the droplet radius ranges from 5 μm to 1 μm in the d^2 curve (Figure C.3).

C.5.2   Test case 2: $r_d = 10$ μm (or $d_d = 20$ μm)

For this larger diameter droplet, the same quantities monitored before are considered. It may be seen from the figures that the larger droplet size does not
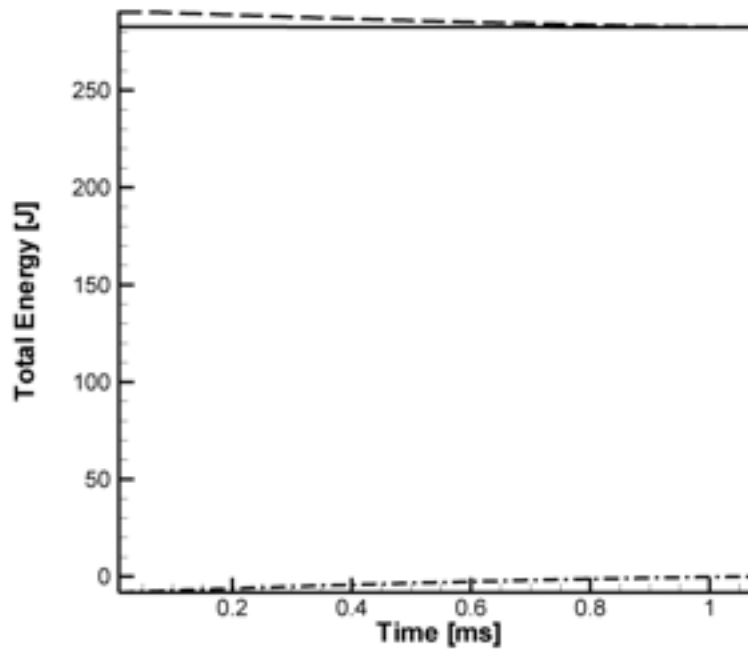
Figure C.2: Conservation of energy (droplet diameter 10μm). The solid black curve is the total energy of the system, expressed as the sum of gas phase (dashed lines) and liquid phase (dash-dotted lines) energies. The total energy of the system remains nearly constant, showing a variation of only 0.1% over the course of the droplet's lifetime (1 ms).
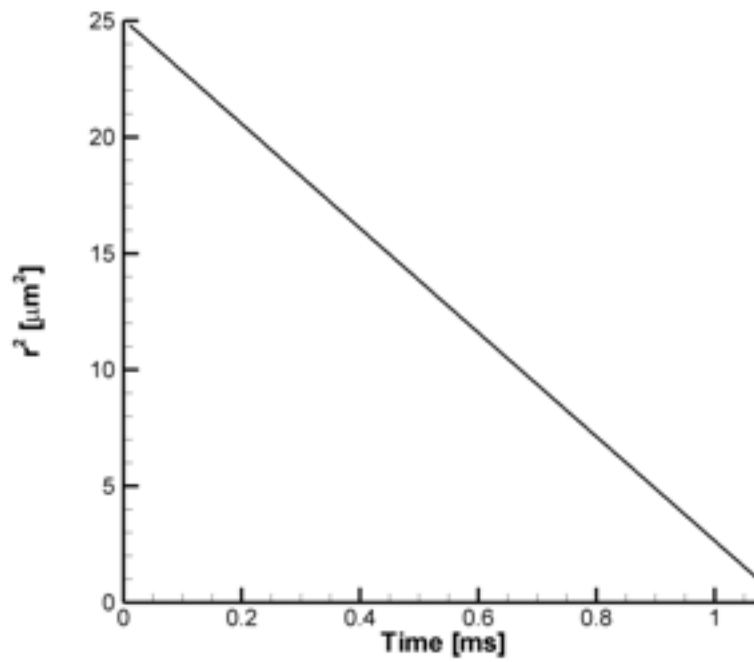
Figure C.3: The d^2 law (droplet diameter 10 μm). The square of the droplet's radius is plotted over time. The variation is linear, thus showing that the d^2 law is satisfied for the evaporating droplet.
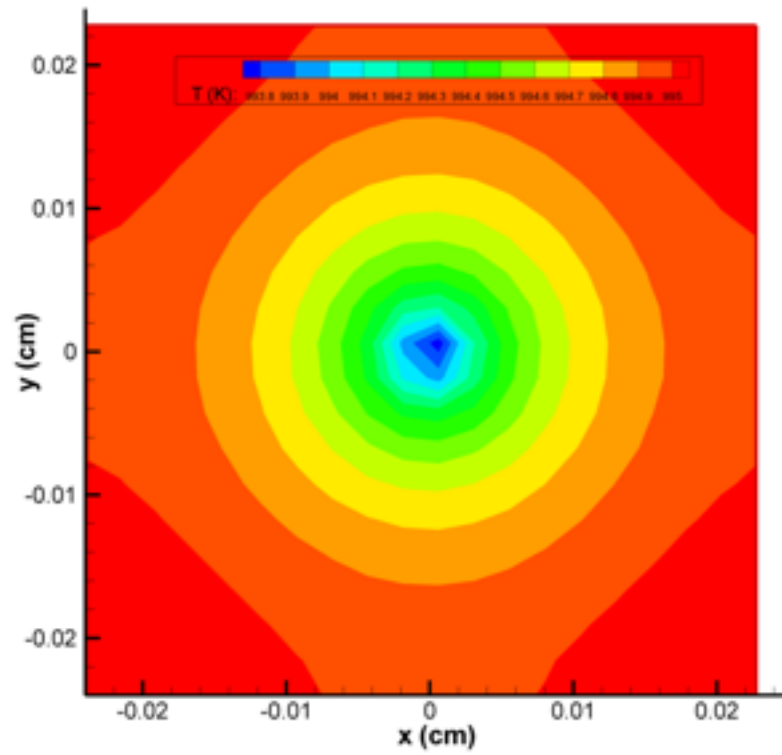
Figure C.4: Temperature isocontours for case with droplet diameter 10 μm. The influence of the droplet spreads radially from the droplet location at the center of the domain.

affect the quality of the simulation, as measured from the mass and energy balance diagnostics.

In Figures C.5 and C.6 are presented the system's mass and energy respectively for the 20 μm droplet case to demonstrate conservation, while in Figure C.7, the d^2 law is demonstrated. Figure C.8 shows a picture of the two dimensional temperature field for the gas-phase.

In Figure C.5, the masses of the droplet and gas phases and their sum are plotted over the course of the droplet's lifetime (4.5 ms). The total mass of the system remains constant, demonstrating that mass conservation is satisfied for the 20 μm droplet.

In Figure C.6, the energies of the droplet and gas phases, and the total energy of the system obtained by summing them are plotted over the course of the droplet's lifetime. The total energy remains nearly constant, with a 1% variation, thus demonstrating that energy conservation is satisfied for the 20 μm diameter droplet. Distinction may be made with the corresponding error in the energy balance computation in the 10 μm diameter case, which is reported at 0.1%. This degradation in comparative solution quality may therefore be attributed to an increase in droplet size relative to the grid, which is expected to affect the fidelity of the solution.

In Figure C.7, the d^2 law is tested by plotting the square of the droplet's radius, versus time. The behavior of this curve is linear, demonstrating that the droplet model obeys the d^2 law.

Figure C.8 depicts the temperature profile in the two dimensional box for the 20 μm droplet case. The influence of the droplet spreads radially outwards from the loca-
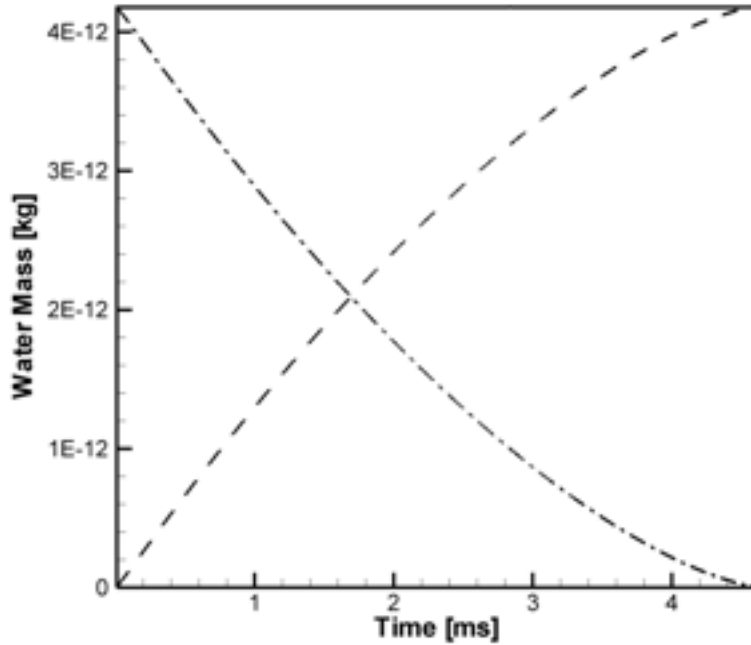
Figure C.5: Conservation of water mass in the system (droplet diameter 20μm). The solid black curve is the total water mass in the system, expressed as the sum of the liquid water mass (dashed-dotted lines) and the gas phase water mass (dashed). The total water mass in the system remains nearly constant over the course of the droplet's lifetime (4.5 ms) .

tion of the droplet at the center of the domain. The plot shows a drop in gas-phase temperature at the region of influence.

C.6   Summary

Mass and energy conservation, and the d^2 law are verified for a quiescent flow, single stationary droplet configuration where the droplet is evaporated to completion by hot ambient gas. Conservation is demonstrated for two droplet diameters, varied parametrically so that they correspond to two cases: one, where the droplet is
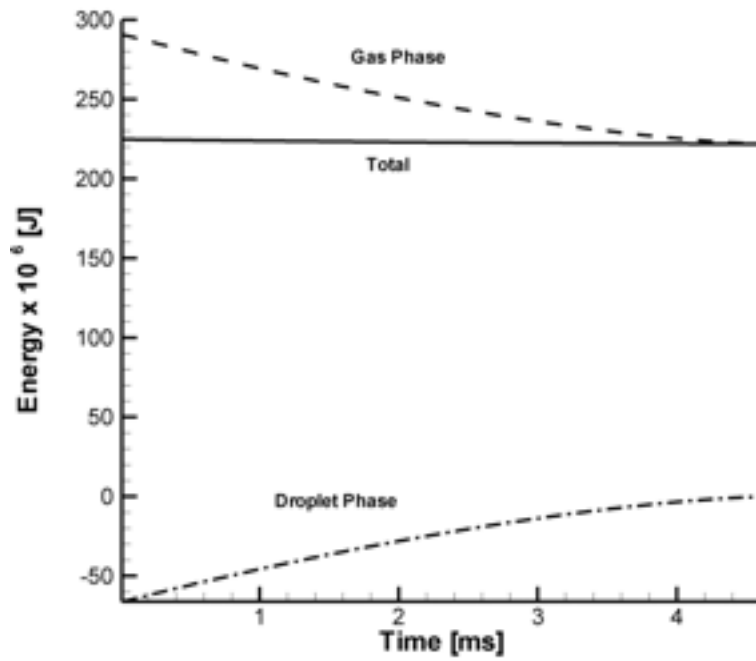
Figure C.6: Conservation of energy (droplet diameter 20 μm). The solid black curve is the total energy of the system, expressed as the sum of gas phase (dashed lines) and liquid phase (dash-dotted lines) energies. The total energy of the system remains nearly constant, showing a variation of only 1% over the course of the droplet's lifetime (4.5 ms).
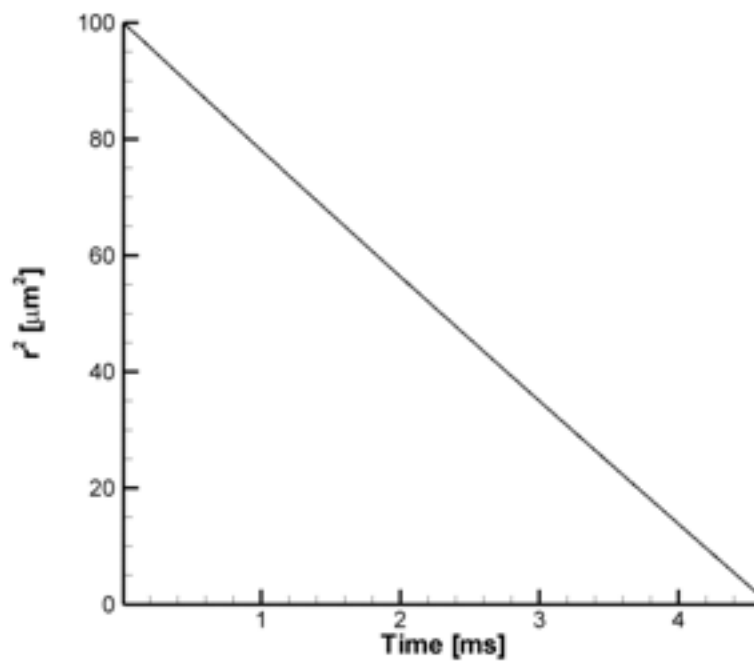
Figure C.7: The d^2 law (droplet diameter 20 μm). The square of the droplet's radius is plotted over time. The variation is linear, thus showing that the d^2 law is satisfied for the evaporating droplet.
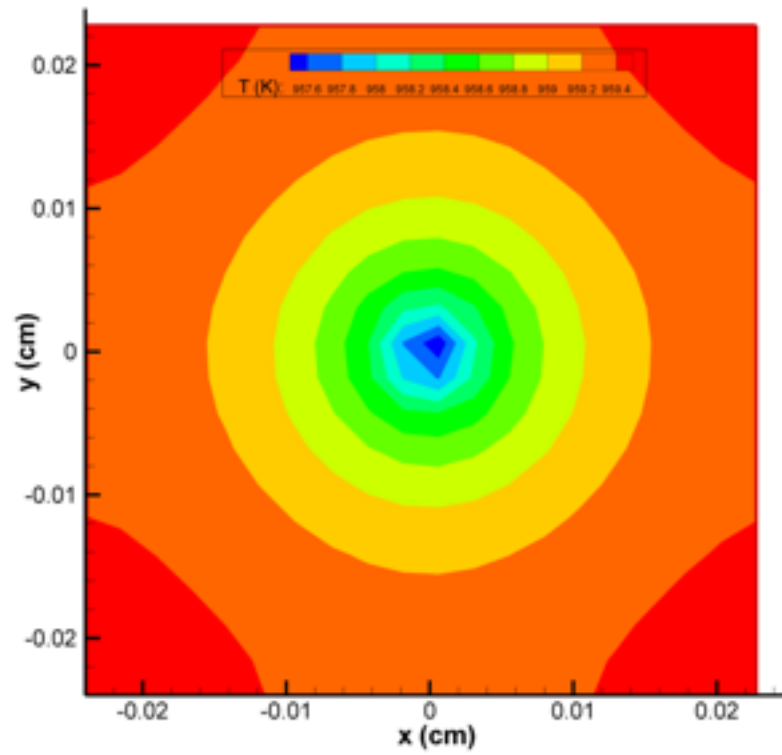
Figure C.8: Temperature isocontours for case with droplet diameter 20 μm. The influence of the droplet spreads radially from the droplet location at the center of the domain.

smaller than the grid cell and the other, where it is larger than the grid cell. It is demonstrated that for the range of parameters chosen, while conservation of mass is satisfied nearly perfectly, energy conservation is also nearly satisfied, albeit with minor discrepancies of up to a tenth of a percentage in the 10 μm diameter case, and a 1% discrepancy in the 20 μm case, as compared with the total energy of the initial system. This increase from 0.1% to 1% in the error in the energy balance computation may be attributed to the increase in droplet size relative to the grid.

The d^2 law is satisfied in both parametric cases, showing a linear decrease of the square of the droplet's radius with time.

It may be concluded, based on the light shed by the present diagnostics, that mass and energy conservation are validated for cases where the droplet size is approximately equal to that of the grid cell, and for less stringent conditions as compared with the test (which uses a grid resolution of 12 μm); in particular, the configuration of the turbulent flame with a grid resolution of 16 μm (Chapter 7), a 10 μm diameter droplet would be simulated adequately by the solver, when viewed from the standpoint of mass and energy balances.

Bibliography

[1] *International Workshop on Measurement and Computation of Turbulent Nonpremixed Flames* (Sandia National Laboratories). `http://public.ca.sandia.gov/TNF/radiation.html`.

[2] Terascale high-fidelity simulations of turbulent combustion with detailed chemistry. WWW page. SciDac Computational Chemistry Program.

[3] ARIAS, P, G., IM, H, G., NARAYANAN, P., AND TROUVÉ, A. Direct numerical simulation of nonpremixed flame extinction by water spray. In *AIAA Aerospace Sciences Meething* (Orlando, FL, January 2010), vol. 48. AIAA-2010-218.

[4] ATREYA, A., AND AGARWAL, S. Effect of radiative heat loss on diffusion flames in quiescent microgravity atmosphere. *Combustion and Flame 115* (1998), 372–382.

[5] ATREYA, A., AGARWAL, S., SACKSTEDER, K, R., AND BAUM, H, R. Observations of methane and ethylene diffusion flames stabilized around a blowing porous sphere under microgravity conditions. In *AIAA Aerospaces Scienecs, Meeting and Exhibit* (Reno, Nevada, 1994), vol. 32.

[6] ATREYA, A., AGARWAL, S., SHAMIM, T., PICKETT, K., SACKSTEDER, K, R., AND BAUM, H, R. Radiant extinction of gaseous diffusion flames. In *Microgravity workshop* (1995), vol. 3.

[7] BAI, X, S., FUCHS, L., AND MAUSS, F. Laminar flamelet structure at low and vanishing scalar dissipation rate. *Combustion and Flame* (2000), 285–300.

[8] BAJPAI. An investigation of the extinction of diffusion flames by halons. *Journal of Fire Flammability 5* (1974), 255–267.

[9] BAUM, H, R. Notes on Howarth transformation. Private communication, 2009.

[10] BAUM, T., POINSOT, T., AND THEVININ, D. Accurate boundary conditions for multi-component reative flows. *Journal of Computational Physics 116*, 2 (1995), 247–261.

[11] BELL, J, B., GREAR, J, F., LIJEWSKI, M, J., DRISCOLL, S, A., AND FILATYEV, S, A. Numerical simulation of a laboratory-scale turbulent slot flame. In *Proceedings of the Combustion Institute* (2007), vol. 31, pp. 1299–1308.

[12] BENDER, C, M., AND ORSZAG, S, A. *Advanced Mathematical Methods for scientists and engineers.* McGraw-Hill Book Company, 1978.

[13] BILGER, R, W. The structure of turbulent nonpremixed flames. In *Proceedings of the Combustion Institute* (1988), vol. 22, pp. 475–488.

[14] BROOKES, S, J., AND MOSS, J, B. Predictions of soot and thermal radiation properties in confined turbulent jet diffusion flames. *Combustion and Flame 116* (1999).

[15] BUNDY, M., HAMINS, A., AND LEE, K, Y. Suppression limits of low strain rate non-premixed methane flames. *Combustion and Flame 133* (2003), 299–310.

[16] BURKE, S, P., AND SCHUMANN, T, W. Bs flame. *Industrial Engineering Chemistry 20*, 10 (1928), 998–1004.

[17] CARRIER, G, F., AND FENDELL, F, E. The effect of strain rate on diffusion flames. ii: Large straining. *SIAM Journal on Applied Mathematics 30*, 3 (May 1976).

[18] CARRIER, G, F., AND PEARSON, C, E. *Ordinary Differential Equations, Theory and Practice*. Classics in Applied Mathematics. SIAM, 1992.

[19] CARRIER, G, K., FENDELL, F, E., AND MARBLE, F, E. The effect of strain rate on diffusion flames. *SIAM Journal on Applied Mathematics 28*, 2 (March 1975).

[20] CHAN, S, H., YIN, J, Q., AND SHI, B, J. Structure and extinction of methane-air flamelet with radiation and detailed chemical kinetic mechanism. *Combustion and Flame 112* (1998), 445–456.

[21] CHAO, B, H., AND LAW, C, K. Asymptotic theory of flame extinction with surface radiation. *Combustion and Flame 92* (1993), 1–24.

[22] CHAO, B, H., LAW, C, K., AND T'IEN, J, S. Structure and extinction of diffusion flames with flame radiation. In *Proceedings of the Combustion Institute* (1990), vol. 23, pp. 523–531.

[23] CHEN, C, L., AND SOHRAB, S, H. Simultaneous effects of fuel/oxidizer concentrations on the extinction of counterflow diffusion flames. *Combustion and Flame 86* (1991), 383–393.

[24] CHEN, R., CHAOS, M., AND KOTHAWALA, A. Lewis number effects in laminar diffusion flames near and away from extinction. In *Proceedings of the Combustion Institute* (2007), vol. 31, pp. 1231–1237.

[25] CHERNOVSKY, M, K. *An experimental study of temperature and radiation characteristics of transient spherical diffusion flames in microgravity*. PhD thesis, The University of Michigan, Ann Arbor, 2006.

[26] Chung, S, H., and Law, C, K. Structure and extinction of convective diffusion flames with general lewis numbers. *Combustion and Flame 52* (1983), 59–79.

[27] Coppola, G., Coriton, B., and Gomez, A. Highly turbulent counterflow flames: a laboratory scale benchark for practical systems. *Combustion and Flame 156* (2009), 1834–1843.

[28] Daguse, T., Croenenbek, T., Rolon, J, C., Darabiha, N., and Soufiani, A. Study of radiative effects on laminar counterflow $H_2/O_2/N_2$ diffusion flames. *Combustion and Flame 106* (1996), 271–287.

[29] Fairweather, M., Jones, W, P., Ledin, H, S., and Lindstedt, R, P. Predictions of soot formation in turbulent, non-premixed propane flames. In *Proceedings of the Combustion Institute* (1992), vol. 24, pp. 1067–1074.

[30] Fendell, F, E. Ignition and extinction in combustion of initially unmixed reactants. *Journal of Fluid Mechanics 21* (1965), 281–303.

[31] Friedman, R. *Theory of fire extinguishment*, 19 ed. Fire Protection Handbook. National Fire Protection Association, 2003, ch. 2, pp. 83–96.

[32] Gottuk, D, T., and Roby, R, J. The role of temperature on carbon monoxide production in compartment fires. *Fire Safety Journal 24* (1995), 315–331.

[33] Gottuk, D, T., and Roby, R, J. *Effect of combustion conditions on species production*, 3 ed. National Fire Protection Association, 2002, ch. 2, pp. 54–82.

[34] Grant, G., Brenton, J., and Drysdale, D. Fire suppression by water spray. *Progress in Energy and Combustion Sciences 26* (2000), 79–130.

[35] Grant, G., Brenton, J., and Drysdale, D. Fire suppression by water sprays. *Progress in Energy and Combustion Science 26* (2000), 79–130.

[36] Hamins, A., Bundy, M., Oh, C, B., and Kim, S, C. Effect of buoyancy on the radiative extinction limit of low-strain-rate nonpremixed methane-air flames. *Combustion and Flame 151* (2007), 225–234.

[37] Hamins, A., Trees, D., Seshadri, K., and Chelliah, H, K. Extinction of nonpremixed flames with halogenated fire suppressants. *Combustion and Flame 99* (1994), 221–230.

[38] Im, H, G., and Chen, J, H. Structure and propagation of triple flames in partially premixed hydrogen-air mixtures. *Combustion and Flame 119* (1999), 436–454.

[39] IM, H, G., TROUVÉ, A., AND RUTLAND, C, J. Direct numerical simulation of turbulent flame quenching by fine water droplets. Tech. rep., Department of Energy, 2007. *Innovative and Novel Computational Impact on Theory and Experiment (INCITE)*.

[40] JOULAIN, P. The behavior of pool fires: State of the art and new insights. In *Proceedings of the Combustion Institute* (1998), vol. 27, pp. 2691–2706.

[41] KARLSSON, B., AND QUINTIERE, J, G. *Enclosure Fire Dynamics*. CRC press, 2000.

[42] KATTA, V, R., TAKAHASHI, F., AND LINTERIS, G, T. Suppression of cup-burner flames using carbon dioxide in microgravity. *Combustion and Flame 137* (2004), 506–522.

[43] KEE, R, J., GRCAR, J., AND RUPLEY, J. OPPDIFF: a Fortran program for computing opposed flow diffusion flames. Tech. Rep. SAND96-8243, Sandia National Laboratories, 1997.

[44] KEE, R, J., RUPLEY, F, M., MEEKS, R., AND MILLER, J, A. Chemkin-III: a fortran chemical kinetics package for the analysis of gas-phase chemical and plasma kinetics. Tech. Rep. SAND96-8216, Sandia National Laboratories Report, 1996.

[45] KENNEDY, C, A., AND CARPENTER, M, H. A comparison of several numerical methods for simulation of compressible shear layers. *Applied Numerical Math. 14*, 4 (1994), 397–433.

[46] KENNEDY, C, A., CARPENTER, M, H., AND LEWIS, R, H. Low-storage, explicit runge-kutta schemes for the compressible navier-stokes equations. *Applied Numerical Math. 35*, 3 (2000), 177–219.

[47] LAW, C, K. *Combustion Physics*. Cambridge university press, 2006.

[48] LECOUSTRE, V, R., SUNDERLAND, P, B., CHAO, B, H., URBAN, D, L., STOCKER, D, P., AND AXELBAUM, R, L. Effects of C/O ratio and temperature on sooting limits in spherical diffusion flames. In *AIAA conference*. Submitted for publication.

[49] LECOUSTRE, V. *Numerical Investigations Of Gaseous Spherical Diffusion Flames*. PhD thesis, The University of Maryland, College Park, 2009.

[50] LENTATI, A, M., AND CHELLIAH, H, K. Dynamics of water droplets in a counterflow field and their effect on flame extinction. *Combustion and Flame 115* (1998), 158–179.

[51] LENTATI, A, M., AND CHELLIAH, H, K. Flame inhibitionsuppression by water mist: Droplet size/surface area, flame structure, and flow residence time effects. In *Proceedings of the Combustion Institute* (2007), vol. 31, pp. 2711–2719.

[52] Leung, K, M., Lindstedt, R, P., and Jones, W, P. A simplified reaction mechanism for soot formation in nonpremixed flames. *Combustion and Flame 87* (1991), 289–305.

[53] Liñan, A. The asymptotic structure of counterflow diffusion flames for large activation energies. *Acta Astronautica 1007*, 1 (1974), 1–29.

[54] Liñan, A., and Crespo, A. An asymptotic analysis of unsteady diffusion flames for large activation energies. *Combustion Science and Technology 14*, 95 (1976).

[55] Lignell, D, O., Chen, J, H., Smith, P, J., Lu, T., and Law, C, K. The effect of flame structure on soot formation and transport in turbulent nonpremixed flames using direct numerical simulation. *Combustion and Flame 151* (2007), 2–28.

[56] Linteris, T., Takahasi, F., and Katta, V, R. Cup-burner flame extinguishment by CF_3Br and Br_2. *Combustion and Flame 149* (2007), 91–103.

[57] Liu, F., Smallwood, G, J., Gülder, Ö, L., and Ju, Y. Asymptotic analysis of radiative extinction in counterflow diffusion flames of nonunity lewis numbers. *Combustion and Flame 121* (2000), 275–287.

[58] Lockwood, F, C., and Shah, N, G. A new radiation solution method for incorporation in general combustion prediction procedures. In *Proceedings of the Combustion Institute* (1980), vol. 18, pp. 1405–1414.

[59] Logue, J, M. *Characteristics of Low Strain Near Extinction Flames in μG and* 1G. PhD thesis, The University of Maryland, College Park, 2003.

[60] Lu, T., and Law, C, K. A directed relation graph method for mechanism reduction. In *Proceedings of the Combustion Institute* (2005), vol. 30, pp. 1333–1341.

[61] Markstein, G, H. Relationship between smoke point and radiant emission from buoyant turbulent and laminar diffusion flames. In *Proceedings of the Combustion Institute* (1985), vol. 20, pp. 1055–1061.

[62] Markstein, G, H., and de Ris, J. Radiant emission and absorption by laminar ethylene and propylene diffusion flames. In *Proceedings of the Combustion Institute* (1985), vol. 20, pp. 1637–1646.

[63] Maruta, K., Yoshida, M., Guo, H., Ju, Y., and Niioka, T. Extinction of low-stretched diffusion flame in microgravity. *Combustion and Flame 112* (1998), 181–187.

[64] Mills, K., and Matalon, M. Extinction of spherical diffusion flames in the presence of radiative heat loss. In *Proceedings of the Combustion Institute* (1998), vol. 27, pp. 2345–2341.

[65] MIZOBUCHI, S., TACHIBANA, S., SHINIO, J., OGAWA, S., AND TAKENO, T. A numerical analysis of the structure of a turbulent hydrogen jet lifted flame. In *Proceedings of the Combustion Institute* (2002), vol. 29, pp. 2009–2015.

[66] MODEST, M, F. *Radiative Heat Transfer*, second ed. Academic Press, San Diego, CA, 2003.

[67] MOIN, P., AND MAHESH, K. Direct numerical simulation: A tool in turbulence research. *Annual Reviews of Fluid Mechanics 30* (1998), 539–578.

[68] MOSS, J, B., STEWART, C, D., AND SYED, K, J. Flowfield modeling of soot formation at elevated pressure. In *Proceedings of the Combustion Institute* (1988), vol. 22.

[69] MOSS, J, B., STEWART, C, D., AND YOUNG, K, J. Modeling soot formation and burnout in a high temperature laminar diffusion flame burning under oxygen-enriched conditions. *Combustion and Flame 101* (1995), 491–500.

[70] NARAYANAN, P., BAUM, H, R., AND TROUVÉ, A. Effect of soot addition on extinction limits of luminous laminar counterflow diffusion flames. In *Proceedings of the Combustion Institute* (2010). Accepted for publication.

[71] NARAYANAN, P., AND TROUVÉ, A. Radiation-driven flame weakening effects in turbulent diffusion flames. In *Proceedings of the Combustion Institute* (2009), vol. 32, pp. 1481–1489.

[72] ORLOFF, L., DE RIS, J., AND DELECHATSIOS, J. Radiation from buoyant diffusion flames. *Combustion Science and Technology 84* (July 1992), 177–186.

[73] PETERS, N. Local quenching due to flame stretch and non-premixed turbulent combustion. *Combustion Science and Technology 30* (1983), 1–17.

[74] PETERS, N. Laminar flamelet concepts in turbulent combustion. In *Proceedings of the Combustion Institute* (1991), vol. 23, pp. 1231–1250.

[75] PETERS, N. *Turbulent combustion.* Cambridge university press, 2000.

[76] PICKETT, K., ATREYA, A., AND AGARWAL, S. Radiation from unsteady spherical diffusion flames in microgravity. In *AIAA Aerospace Sciences, Meeting and Exhibit* (Reno, Nevada, 1995), vol. 33.

[77] PITTS, W, M. Reactivity of product gases generated in idealized enclosure fire environments. In *Proceedings of the Combustion Institute* (1992), vol. 24, pp. 1736–1746.

[78] POINSOT, T., AND LELE, S, K. Boundary conditions for direct simulations of compressible viscous flows. *Journal of Computational Physics 101* (1992), 101–129.

[79] PURI, I, K., AND SESHADRI, K. Extinction of diffusion flames burning diluted methane and diluted propane in diluted air. *Combustion and Flame 65* (1986), 137–150.

[80] QUINTIERE, J, G. Fire behavior in building compartments. In *Proceedings of the Combustion Institute* (2002), vol. 29, pp. 181–193.

[81] QUINTIERE, J, G., AND RANGAWALA, A, S. A theory for flame extinction based on flame temperature. *Fire and Materials 28* (2004), 387–402.

[82] RHATIGAN, J, H., BEDIR, H., AND T'IEN, J, S. Gas-phase radiative effects on the burning and extinction of a solid fuel. *Combustion and Flame 112* (1998), 231–241.

[83] SANKARAN, R., HAWKES, E, R., CHEN, J, H., LU, T., AND LAW, C, K. Structure of spatially developing turbulent lean methane-air bunsen flame. In *Proceedings of the Combustion Institute* (2007), vol. 31, pp. 1291–1298.

[84] SANTA, K, J., CHAO, B, H., SUNDERLAND, P, B., TAYLOR, J, L., URBAN, D, L., STOCKER, D, P., AND AXELBAUM, R, L. Radiative extinction of gaseous spherical diffusion flames in microgravity. In *AIAA Aerospace Sciences, Meeting and Exhibit* (Reno, Nevada, 2006), vol. 44.

[85] SANTA, K, J., CHAO, B, H., SUNDERLAND, P, B., TAYLOR, J, L., URBAN, D, L., STOCKER, D, P., AND AXELBAUM, R, L. Radiative extinction of gaseous spherical diffusion flames in microgravity. *Combustion and Flame 151* (2007), 665–675.

[86] SANTA, K, J., CHAO, C, H., SUNDERLAND, P, B., URBAN, D, L., STOCKER, D, P., AND AXELBAUM, R, L. Radiative extinction of gaseous diffusion flames in microgravity. *Combustion and Flame 151* (2007), 665–675.

[87] SESHADRI, K., AND ILINCIC, N. The asymptotic structure of inhibited non-premixed methane-air flames. *Combustion and Flame 101* (1994), 271–294.

[88] SHADDIX, C, R., AND WILLIAMS, T, C. Soot:giver and taker of light. *American Scientist 95* (May 2007).

[89] SOHRAB, S, H., LIÑAN, A., AND WILLIAMS, F, A. Asymptotic theory of diffusion-flame extinction with radiant loss from the flame zone. *Combustion Science and Technology 27* (1982), 143–154.

[90] SONG, T, H., AND VISKANTA, R. Interaction of radiation with turbulence: Application to a combustion system. *J. Thermophys. Heat Transfer 1*, 1 (1987), 56–62.

[91] SPALDING, D, B., AND JAIN, V, K. A theoretical study of the effects of chemical kinetics on a one-dimensional diffusion flames. *Combustion and Flame 6* (1961), 265–273.

[92] Sun, C, J., Sung, C, J., , He, L., and Law, C, K. Dynamics of weakly stretched flames: quantitative description and extraction of global flame parameters. *Combustion and Flame 118* (1999), 108–128.

[93] Syed, K, J., Stewart, C, D., and Moss, J, B. Modeling soot formation and thermal radiation in buoyant turbulent diffusion flames. In *Proceedings of the Combustion Institute* (1990), vol. 23.

[94] Szoke, A., and Brooks, E, D. The transport equation in optically thick media. *Journal of Quantitative Spectroscopy & Radiative Transfer 91* (2005), 95–110.

[95] Takahashi, F., Linteris, G, T., and Katta, V, R. Extinguishment mechanisms of coflow diffusion flames in a cup-burner apparatus. In *Proceedings of the Combustion Institute* (2007), vol. 31, pp. 2721–2729.

[96] Tang, S. *A Computational Study of Spherical Diffusion Flames in Microgravity with Gas Radiation.* PhD thesis, The University of Michigan, Ann Arbor, 2008.

[97] Tang, S., Chernovsky, M., and Atreya, A. A computational study of spherical diffusion flames in microgravity with gas radiation part i: Model development and validation. *Combustion and Flame 157* (2010), 118–126.

[98] Tang, S., Im, H., and Atreya, A. A computational study of spherical diffusion flames in microgravity with gas radiation. part ii: Parametric studies of the diluent effects on flame extinction. *Combustion and Flame 157* (2010), 127–136.

[99] T'ien, J, S. Diffusion flame extinction at small stretch rates: The mechanism of radiative loss. *Combustion and Flame 65* (1986), 31–34.

[100] T'ien, J, S., and Bedir, H. Radiative extinction of diffusion flames- a review. In *Asia-Pacific Conference on Combustion* (Osaka, Japan, May 12-15 1997).

[101] T'ien, J, S., and Bedir, H. A computational study of flame radiation in pmma diffusion flames including fuel vapor participation. In *Proceedings of the Combustion Institute* (1998), vol. 27, pp. 2821–2828.

[102] Tse, S, D., Zhu, D., Sung, C., Ju, Y., and Law, C, K. Microgravity burner generated diffusion flames: Experiment and computation. *Combustion and Flame 125* (2001), 1265–1278.

[103] Tsuji, J., and Yamaoka, I. The structure of counterflow diffusion flames in the forward stagnation region of a porous cylinder. In *Proceedings of the Combustion Institute* (1969), vol. 12, pp. 997–1005.

[104] Tsuji, J., and Yamaoka, I. Structure analysis of counterflow diffusion flames in the forward stagnation region of a porous cylinder. In *Proceedings of the Combustion Institute* (1971), vol. 13, pp. 723–731.

[105] Utiskul, Y. *Theoretical and Experimental Study on Fully-Developed Compartment Fires.* PhD thesis, The University of Maryland, College Park, 2007.

[106] Vervish, L., and Poinsot, T. Direct numerical simulation of non-premixed turbulent flames. *Annual Reviews of Fluid Mechanics 30* (1998), 655–691.

[107] Wang, Y. *Direct Numerical Simulation of non-premixed combustion with soot and radiation.* PhD thesis, The University of Maryland, College Park, 2005.

[108] Wang, Y., and Rutland, C. Effects of temperature and equivalence ratio on the ignition of n-heptane fuel droplets in turbulent flow. In *Proceedings of the Combustion Institute* (2004), vol. 30, pp. 893–900.

[109] Wang, Y., and Rutland, C. Direct numerical simulation of ignition of turbulent n-heptane fuel spray jets. *Combustion and Flame 149* (2007), 353–365.

[110] Wang, Y., and Trouvé, A. Direct numerical simulation of nonpremixed flame-wall interactions. *Combustion and Flame 144* (2006), 461–475.

[111] Wang, H, Y., Chen, W, H., and Law, C, K. Extinction of counterflow diffusion flames with radiative heat loss and nonunity lewis numbers. *Combustion and Flame 148* (2007), 100–116.

[112] Westbrook, C, K., and Dryer, F, L. Simplified reaction mechanism for the oxidation of hydrocarbon fuels in flames. *Combustion Science and Technology 27* (1981), 31–43.

[113] Williams, F, A. *Combustion Theory.* Benjamin Cummings, Menlo Park, CA, 1985.

[114] Williams, F, A. Progress in knowledge of flamelet structure and extinction. *Progress in Energy and Combustion Science 26* (2000), 657–682.

[115] Williamson, J. *Measurements and analysis of extinction in vitiated flame sheets.* PhD thesis, The University of Maryland, College Park, 2008.

[116] Yoo, C, S. *Direct Numerical Simulations of Strained Laminar and turbulent nonpremixed flames: Computational and Physical Aspects.* PhD thesis, The University of Michigan, Ann Arbor, 2005.

[117] Yoo, C, S., Sankaran, R., and Chen, J, H. Three-dimensional direct numerical simulationof a turbulent lifted hydrogen jet flame in heated coflow: flame stabilization and structure. *Journal of Fluid Mechanics 640* (2009), 453–481.